FEMTOSECOND OPTICAL PARAMETRIC OSCILLATORS IN THE MID-INFRARED

Zoe E. Penman

A Thesis Submitted for the Degree of PhD
at the
University of St Andrews

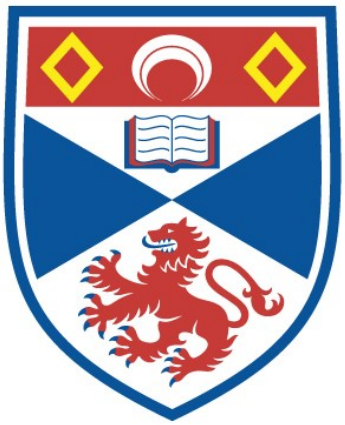

1999

Femtosecond Optical Parametric Oscillators in the Mid-infrared

Thesis submitted for the degree of Doctor of Philosophy
to the University of St Andrews
by

Zoe E. Penman, M.Sci.

October 1998

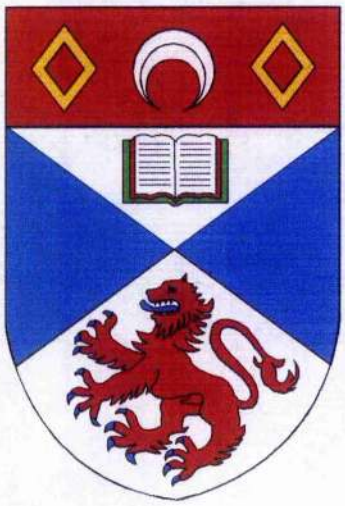

The J.F. Allen Physics Research Laboratories
School of Physics and Astronomy
University of St Andrews
North Haugh
St Andrews
Fife, KY16 9SS

Declarations

I, Zöe Penman, hereby certify that this thesis was written by me, that it is a record of my own work and that it has not been accepted in partial of complete fulfilment of any other degree or professional qualification.

I was admitted to the School of Physics and Astronomy at the University of St. Andrews, as a candidate for the degree of Doctor of Philosophy in October 1995 and remained there as a research student until October 1998.

Date: 2/4/98 Signature of Candidate:

I hereby certify that the candidate has fulfilled the conditions of the Resolution and Regulations appropriate for the degree of Doctor of Philosophy in the University of St. Andrews and that the candidate is qualified to submit this thesis as an application for that degree.

Date: 02/11/98 Signature of Supervisor:

Copyright

In submitting this thesis to the University of St. Andrews I understand that I am giving permission for it to be made available for use in accordance with the regulations of the University Library for the time being in force, subject to any copyright vested in the work not being affected thereby. I also understand that the title and abstract will be published, and that a copy of the work may be made and supplied to any *bona fide* library or research worker.

Date: 2/11/98 Signature of Candidate:

What is research, but a blind date with knowledge.

Abstract

The work described in this thesis is concerned with the development of self-modelocked Ti:sapphire lasers and femtosecond optical parametric oscillators based on periodically-poled rubidium titanyl arsenate and periodically-poled lithium niobate and operating in the near and mid-infrared.

In Chapter 1 the theory of ultrashort pulse generation is explained with regard to the Ti:sapphire laser. The optical properties of Ti:sapphire are discussed along with the principles of laser oscillation and pulse generation. The techniques used to modelock the lasers used in the experimental work, which follows, are also considered. The second part of the chapter deals with typical measurement techniques for characterising femtosecond optical pulses from a laser or an OPO, including a detailed explanation of second harmonic generation autocorrelation. Chapter 1 concludes with a thorough description of frequency-resolved optical gating, the newest of these pulse characterisation techniques.

In Chapter 2 the subject of nonlinear optics and the properties of nonlinear optical materials are discussed. Phasematching in nonlinear optical materials is explained along with the principle techniques for achieving this, including birefringent phasematching and quasi-phasematching. A review of techniques for periodically-poling nonlinear optical crystals is also given. The chapter concludes with a section on the optical effects of group velocity dispersion and self-phase modulation, that influence the output from an ultrashort pulse laser or OPO and describes methods for

second and third-order dispersion compensation. Chapter 2 concludes the theory required to explain the experiments described in Chapters 3, 4, 5 and 6.

Chapter 3 describes the operation and characterisation of two different Ti:sapphire laser systems involving different methods of dispersion compensation. The first laser produces 100 fs duration self-modelocked laser pulses and dispersion compensation is achieved by including a pair of prisms in the cavity. This laser system is discussed further in Chapter 5, where it is operated in conjunction with a Spectra Physics Millennia, as the pump source for an all-solid-state femtosecond OPO based on periodically-poled lithium niobate. A second laser system is described in Chapter 3, which produces self-modelocked pulses of ~15 fs duration and dispersion compensation is achieved by including chirped multilayer dielectric mirrors in the cavity.

The subject matter that Chapter 4 is concerned with includes the operation and characterisation of a femtosecond OPO based on PPRTA. Ti:sapphire pump wavelength tuning and cavity-length tuning of the OPO are shown to produce wavelengths throughout the range 1.060 μm to 1.225 μm in the signal and 2.67 μm to 4.5 μm in the idler, with average output powers as high as 120 mW in the signal and 105 mW in the idler output. The effects of photorefractive damage are minimal and consequently this offers the possibility of room-temperature operation of the PPRTA-based OPO.

Chapter 5 is concerned with the generation of longer idler wavelengths, in the region of 5 μm, from an all-solid-state OPO based on periodically-poled lithium niobate. The

approach used with the PPRTA-based OPO is extended to PPLN and in Chapter 5, results are presented which show that the use of an all-solid-state Ti:sapphire pump source in combination with a PPLN-based OPO represents a robust source of high-repetition-rate femtosecond pulses in the mid-infrared at wavelengths out to ~5 μm. Significantly higher output powers in the signal and idler than previously reported are also measured.

In Chapter 6 a similar PPLN-based OPO is described, with modifications to the cavity elements, to reduce the output pulse duration of the OPO. This system is pumped by a sub- 20 fs Ti:sapphire laser. A pulse duration of 175 fs is recorded for the signal at a wavelength of 1.07 μm. Output powers of 28 mW for the signal at 1.07 μm and 6.8 mW for the idler at 2.7 μm are also measured. The tuning range for the signal extends from 1.045 μm to 1.190 μm, and for the idler, extends from 2.57 μm to 3.67 μm.

Contents

CHAPTER 3

CHAPTER 4

CHAPTER 5

CHAPTER 1

Ultrashort Light Pulse Generation and Characterisation

This chapter is concerned with the generation of ultrashort light pulses from a Ti:sapphire laser and the various methods for characterising ultrashort light pulses. The properties of Ti:sapphire as a laser gain medium are discussed and the principles of ultrashort pulse generation are explained. Details of the different modelocking techniques that are relevant to this work are given. The chapter concludes with a section on ultrashort pulse measurements and includes the second harmonic generation autocorrelation and frequency-resolved optical gating techniques.

Ti:Sapphire as a Laser Gain Medium

Since the first demonstration of Ti:sapphire as a laser gain medium in 1982[1,2], it has become one of the most popular for use in the near-infrared and offers wide tunability, high output powers and straightforward modelocking procedures.

In early solid-state lasers such as ruby and Nd:YAG[3], lasing occurred as a result of photon transitions between electronic levels. This meant that these lasers could only support a narrow band of wavelengths. Ti:sapphire, on the other hand, is a vibronic gain medium, a characteristic of which is that electronic vibrations within the crystal cause laser transitions between broad bands and it is this property which allows the laser output to be both widely and continuously tunable.

The molecular structure of Ti:Al_2O_3 is shown in Figure 1. It consists of either a Ti^{3+} ion or an Al^{3+} ion surrounded by an octahedron of O^{2-} ions.

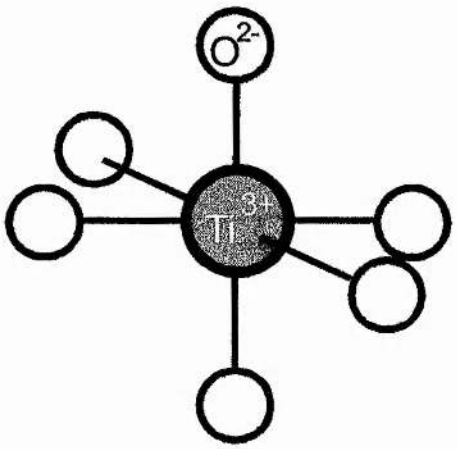

Figure 1: The molecular structure of Ti:sapphire.

The transition metal titanium (Ti) has an electronic configuration described by $1s^2 2s^2 2p^6 3s^2 3p^6 3d^n$[4]. When a Ti ion is substituted for an Al^{3+} in Al_2O_3 it can be either trivalent Ti^{3+} or quadravalent Ti^{4+}. The Ti^{4+} ion has a closed shell, which makes it optically inert. The Ti^{3+} ion has a closed shell plus one outer $3d^1$ valence electron thus the Ti^{3+} ion is the active ion in titanium-doped sapphire. A single 3d electron has a ^2D ground state, but when placed in a host crystal such as sapphire, the cubic and trigonal fields of the O^{2-} ions splits the energy levels into a three-fold degenerate $^2T_2$ ground state and a two-fold degenerate ^2E excited state. The structure of these energy levels is illustrated in Figure 2, and it is between these two levels that lasing occurs. Promotion of the 3d electron to even higher lying energy levels within Ti:sapphire requires energy levels far greater than those required for optical pumping to initiate lasing. Thus the Ti:sapphire laser performance is not compromised by excited state absorption of either the pump or the laser radiation.

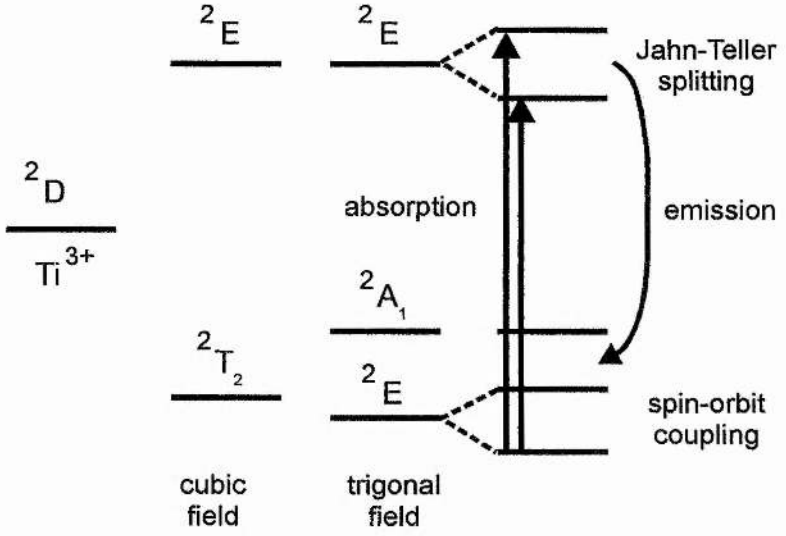

Figure 2: Energy level splitting in Ti:sapphire.

Ti:sapphire is characteristically pink in colour because the peak of the main absorption band is at around 500 nm[5]. This is shown in Figure 3. The presence of Ti^{3+} - Ti^{4+} pairs within the crystal accounts for the second, relatively weak absorption band between 650 nm and 1000 nm. Improvements in crystal growth techniques mean that in high quality crystals this weak residual absorption loss is not sufficient to seriously impair the efficiency and performance of the Ti:sapphire laser. It can also be seen from Figure 3, that the absorption of π-polarised light is 2.3 times stronger than the absorption of σ-polarised light. π-polarised light has its polarisation perpendicular to the c-axis within the crystal and σ-polarised light has its polarisation parallel to the c-axis within the crystal. Maximum absorption of the pump beam and therefore most efficient operation of the laser is met when the pump light is π-polarised, that is, its polarisation is perpendicular to the crystallographic c-axis.

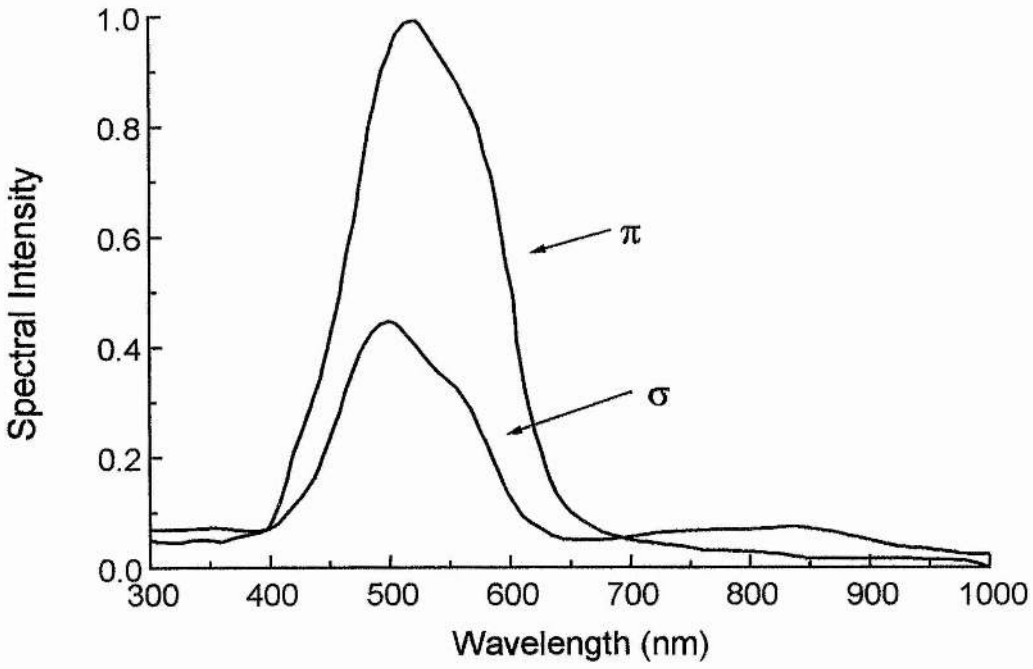

Figure 3: Ti:sapphire absorption spectra for π– and σ-polarised light[5].

Traditionally Ti:sapphire lasers were pumped by mainframe argon-ion lasers producing appropriate blue-green wavelengths from 488 nm to 514 nm. Although these lasers are capable of producing high output powers they are inefficient, bulky and expensive to run, requiring three-phase mains electricity and high-pressure water-cooling. Recent development of all-solid-state diode-pumped frequency-doubled Nd:YLF, Nd:YAG and in particular Nd:YVO_4 lasers has allowed smaller, more efficient systems to take the place of the argon-ion laser. The Spectra-Physics Millennia (frequency-doubled, diode-pumped Nd:YVO_4), for example, is a low cost, compact device powered by single-phase mains electricity with a closed-loop water cooling system. It delivers an output power of either 5 W or 10 W at a wavelength of 532 nm.

The emission spectrum produced by optical pumping of Ti:sapphire at the wavelengths discussed is shown in Figure 4. Extending over 400nm with a peak at around 790 nm, this broad tuning range combined with the output powers typical from Ti:sapphire lasers renders the system ideal for pumping an optical parametric oscillator (OPO).

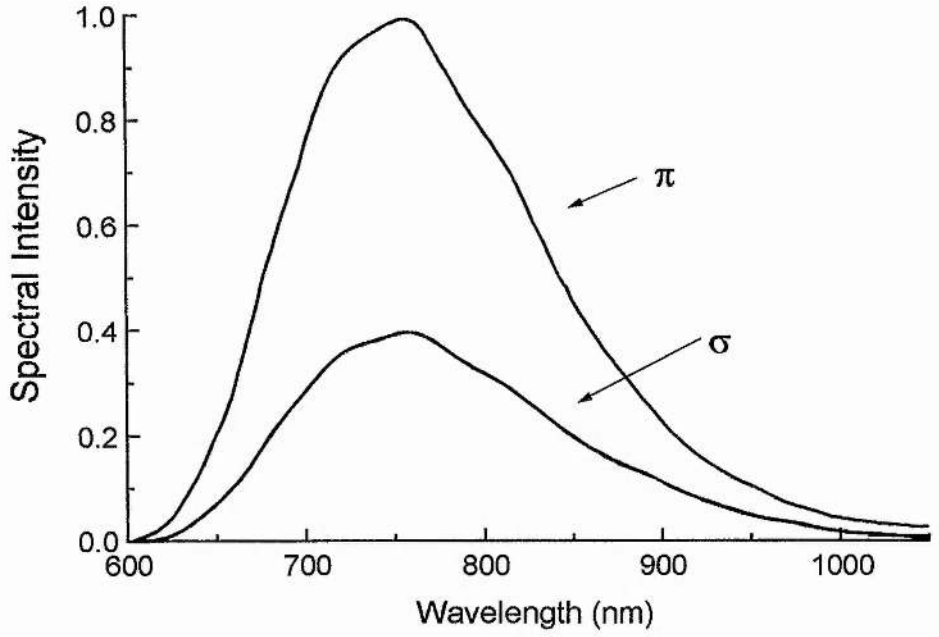

Figure 4: Ti:sapphire emission spectra for π– and σ-polarised light[5].

The upper-state lifetime of Ti:sapphire[6] varies with the temperature of the crystal and this is shown in Figure 5. As the crystal temperature is increased the upper-state lifetime falls, because undesirable non-radiative decay processes occur. At room temperature the non-radiative decay processes are less significant and it is sufficient to cool the Ti:sapphire laser crystal using a simple low-pressure water-cooling system. The upper-state lifetime of Ti:sapphire at room temperature is 3.2 μs. A further advantage of Ti:sapphire as a laser gain medium is that the stimulated emission cross-

section is large, 3×10^{-19} cm^2 and so relatively short crystals can be used.

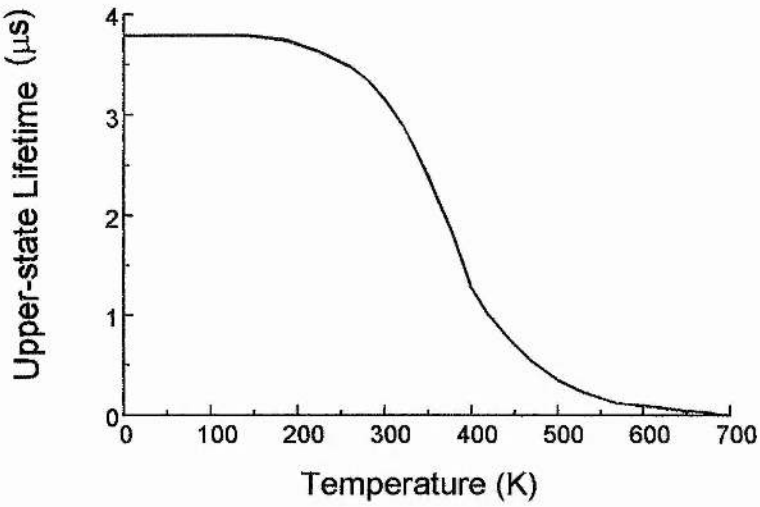

Figure 5: Variation of upper-state lifetime with temperature in Ti:sapphire[6].

Some other optical properties of Ti:sapphire are given in Table 1, for a crystal temperature of 300 K.

Property	**Value at 300 K**
Refractive Index	1.76
Nonlinear Refractive Index	3×10^{-16} cm^2W^{-1}
Thermal Conductivity	0.33 $Wcm^{-1}K^{-1}$
Absorption Cross-section	$5\text{-}8\times10^{-20}$ cm^2
Gain Cross-section	$3\text{-}4\times10^{-19}$ cm^2
Absorption Coefficient	0.7-5.8 cm^{-1}
Upper-state Lifetime	3.2 μs
Ti^{3+} Concentration	$1\text{-}5\times10^{19}$ cm^{-3}

Table 1: Properties of Ti:sapphire.

In Chapter 3 the optical setup and characterisation of two typical Ti:sapphire lasers is described with regard to pumping an OPO. Details of the particular Ti:sapphire laser system used as the pump source for each of the OPOs used in this work are also given at the beginning of the respective OPO chapters. The remainder of this chapter concerns the generation of ultrashort laser pulses and characterisation of ultrashort light pulses as are available from femtosecond lasers and OPOs.

Principles of Laser Oscillation

The light inside a laser cavity circulates for many round trips, and if the intracavity field can reproduce itself exactly after each round trip, then constructive interference will occur. Consequently, a laser can only operate at discrete frequencies for which the intracavity field's round trip phase shift is an integral multiple of 2π, that is a set of evenly spaced frequencies where

$$\Delta\nu = \frac{c}{2nL}$$

$2nL$ is the optical path length of the laser cavity and c is the speed of light. The longitudinal modes corresponding to each of these allowed frequencies see an amount of gain determined by the gain profile of the laser transition. This is illustrated in Figure 6.

For steady-state oscillation to be reached, the intracavity field must experience enough gain to overcome the intracavity loss per round trip. In a narrow bandwidth laser the longitudinal mode nearest to the peak of the gain curve will see more gain during the build-up of laser oscillation than the other modes, and the gain will saturate

when it equals the round trip loss seen by this particular mode. All other modes experience less gain than the peak mode and hence these modes see a net round-trip loss and will not oscillate. When the gain bandwidth is narrow a laser emits a continuous-wave (cw) beam of light at a single longitudinal mode frequency. (This is the case when the laser transition is homogeneously broadened. When the laser transition is inhomogeneously broadened a superposition of many independent homogeneously broadened oscillators are in operation. Each separate oscillator will saturate the gain when the mode nearest to the peak of its gain bandwidth oscillates and so many modes can oscillate across an inhomogeneously broadened linewidth.)

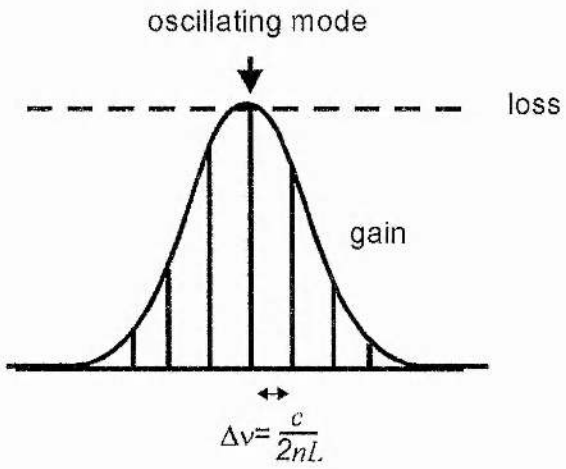

Figure 6: The single oscillating mode is that which experiences sufficient gain to overcome the intracavity loss per round trip.

Ultrashort Light Pulse Generation

In a broad bandwidth laser, such as Ti:sapphire, the peak of the gain bandwidth is quite flat and so more than one longitudinal mode frequency can oscillate. If these frequencies oscillate independently, then the interference between the modes is totally

random and this describes a cw laser. This is shown in Figure 7(a). If, on the other hand, the situation can be modified such that these longitudinal cavity modes oscillate with comparable amplitudes and a definite phase relationship, the laser will modelock to produce an evenly spaced sequence of light pulses and this is shown in Figure 7(b).

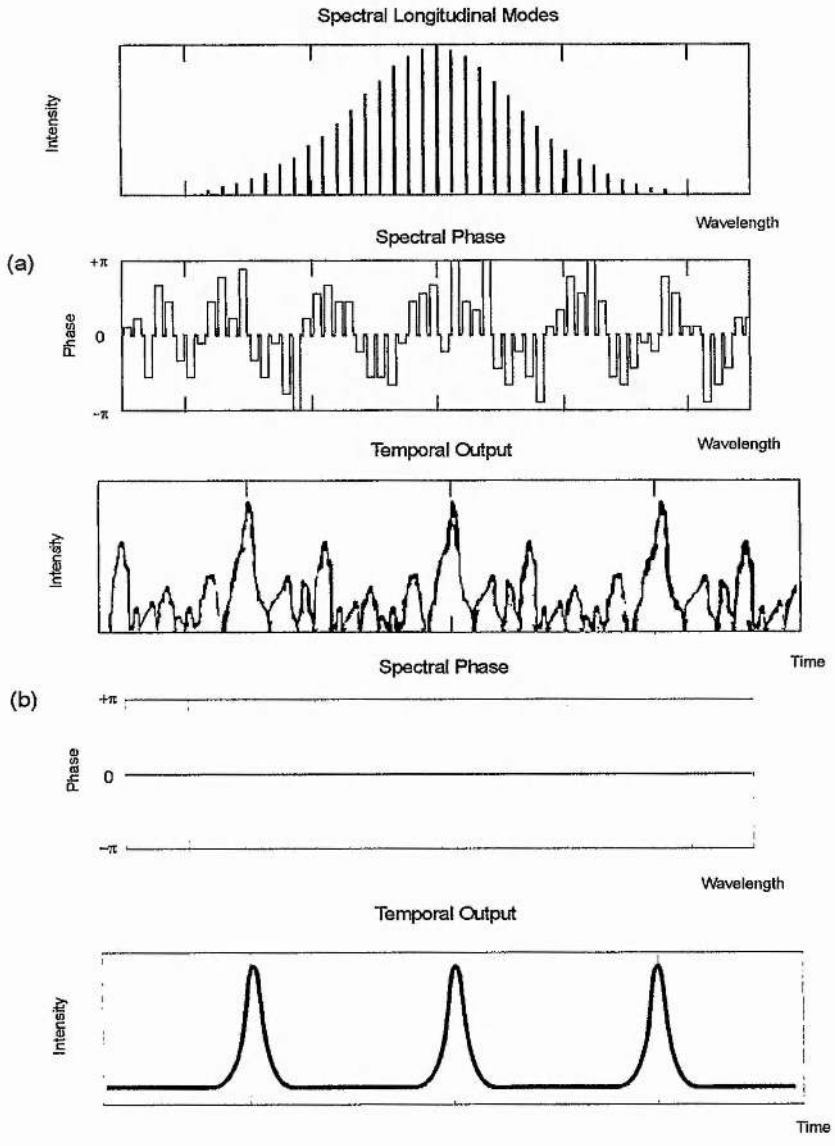

Figure 7: (a) The superposition of many longitudinal modes oscillating with random phases leads to a random continuous-wave output; (b) Many longitudinal modes oscillating with a fixed phase relationship and the resulting pulsed output from the laser.

The conditions required for modelocking can be considered in terms of the behaviour of the intracavity laser field with time. A laser will favour modelocked operation over cw operation if the cavity is aligned so that the gain required by an ultrashort pulse is less than that required during cw operation. A cw field that consists of noise fluctuations will repeat itself at the period of an applied modulation and will continue to be amplified until such time as the gain required by ultrashort pulse operation is less per round-trip. At this point modelocking is achieved. Modelocking can be achieved in a number of ways such as active-modelocking[7], passive-modelocking[8-10] and coupled-cavity modelocking[11,12]. The most recent and most useful method of modelocking is, however, self-modelocking, developed in 1991 by Spence, Kean and Sibbett[13] and it is this technique which is relevant to this work. Self-modelocking of the Ti:sapphire lasers used in this work was achieved using two different self-modelocking methods and these will be explained in the following sections.

Regeneratively-Initiated Self-Modelocking

The technique of regeneratively-initiated self-modelocking[14] involves inserting an acousto-optic modulator into the laser cavity close to one of the end mirrors. The modulator consists of a piezo-electric transducer, which is attached to a quartz block. The modulator is driven by an external signal, which causes changes in the refractive index of the quartz, and thus acts as an optical diffraction grating. This produces a sinusoidal time-varying loss within the cavity, at a specific frequency. If this frequency does not equal the longitudinal mode spacing, the loss it introduces simply

modulates the amplitude of the electric field of each cavity mode. This produces modulation side-bands.

If the modulation frequency *does* equal the longitudinal mode spacing, the oscillating side-bands coincide with the adjacent longitudinal mode frequencies of the resonator. The modes become coupled with locked phases. The modulation period T will equal the cavity round trip time $\frac{2nL}{c}$ and the situation can be described as shown in Figure 8.

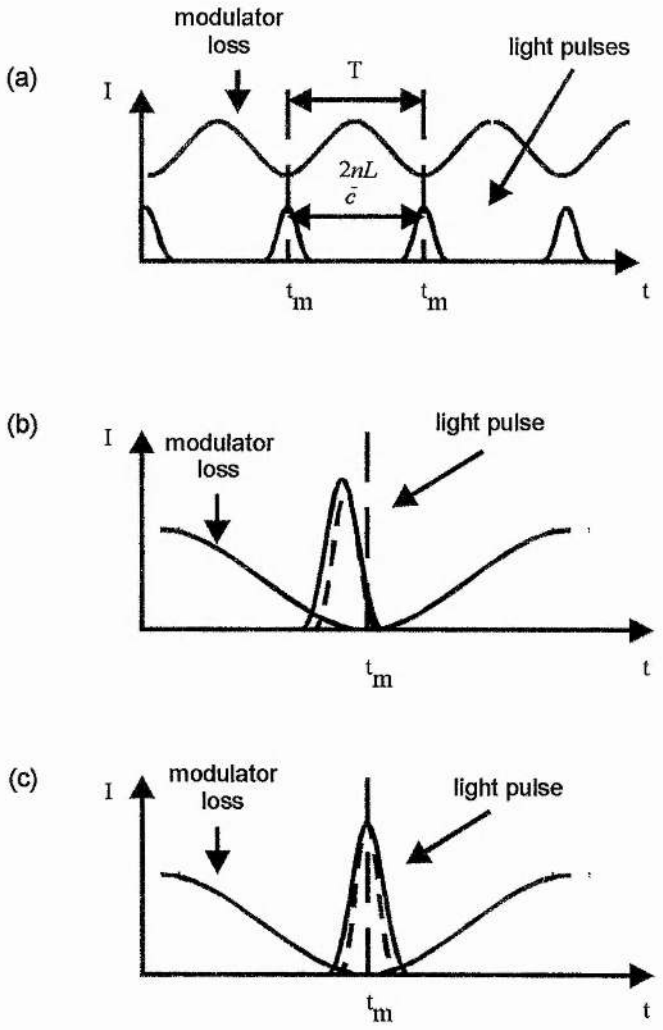

Figure 8: (a), (b) and (c) Pulse evolution in a regeneratively initiated self-modelocked laser cavity.

If the pulse passes through the modulator at a time t_m, of minimum loss, it will return to the modulator at a time $\frac{2nL}{c}$, when the loss is again at a minimum. If the pulse arrives at a time slightly before t_m, the leading edge will suffer more attenuation by the modulators time varying loss than the trailing edge of the pulse. After passing through the modulator, the time at which the pulse peak occurs will have been advanced such that during the next passage the peak will arrive closer to t_m. This corresponds to a stable modelocked condition.

The oscillating bandwidth is concentrated around a central frequency ν_o. A light pulse of finite duration passes through the modulator at a time of minimum loss. The output pulse is narrower than the input pulse since both the leading and trailing edges are attenuated and the peak of the pulse is not. The pulse narrowing is counteracted, by the pulse broadening that occurs on transit through the gain medium.

For the case of acousto-optic (AO) modulation, strain induced by an ultrasonic wave causes local changes in the refractive index of the material. This acts as a phase grating with its period equal to the acoustic wavelength, its amplitude proportional to the sound amplitude and which is travelling at the speed of sound in the medium. The pulse repetition frequency is governed by the applied modulation frequency. AO-modulators have a low optical insertion loss and materials can be driven at a high repetition rate and this can be advantageous.

The modulator can be switched off and the laser will remain modelocked and hence this is the technique of regeneratively-initiated self-modelocking. Self-modelocking

can also be achieved without the use of an AO-modulator as explained below.

Self-Modelocking

In a typical Ti:sapphire laser system, the transverse (spatial) cavity mode is focused to a beam radius of a few tens of microns within the gain medium. This produces high intensities, which for ultrashort pulses means that spatial nonlinear effects such as self-focusing become significant. The self-focusing effect causes an intensity-dependent change in the spatial profile of the oscillating mode. Introduction of an intracavity aperture can be used to favour oscillation of only high intensity part of the beam by providing a power dependent loss in the form of an amplitude modulation. This happens because the nonlinear medium acts as an intensity dependent lens, producing a smaller beam waist for higher light intensities. If an aperture is placed at a location within the laser cavity, see Figure 9(a), where the beam size decreases with increasing intensity, it will have a greater transmission for a high intensity beam than for a low intensity beam. Thus the cavity losses are intensity dependent and the system sees a higher gain with increasing intensity. In a suitably aligned laser cavity, such a passive amplitude modulation mechanism can favour modelocked operation over cw operation[15]. Self-modelocking can take place even in the absence of an intracavity aperture[16]. The combination of self-focusing and gain saturation produces a differential gain that favours the growth of short pulses and eliminates cw oscillations. This is shown in Figure 9(b).

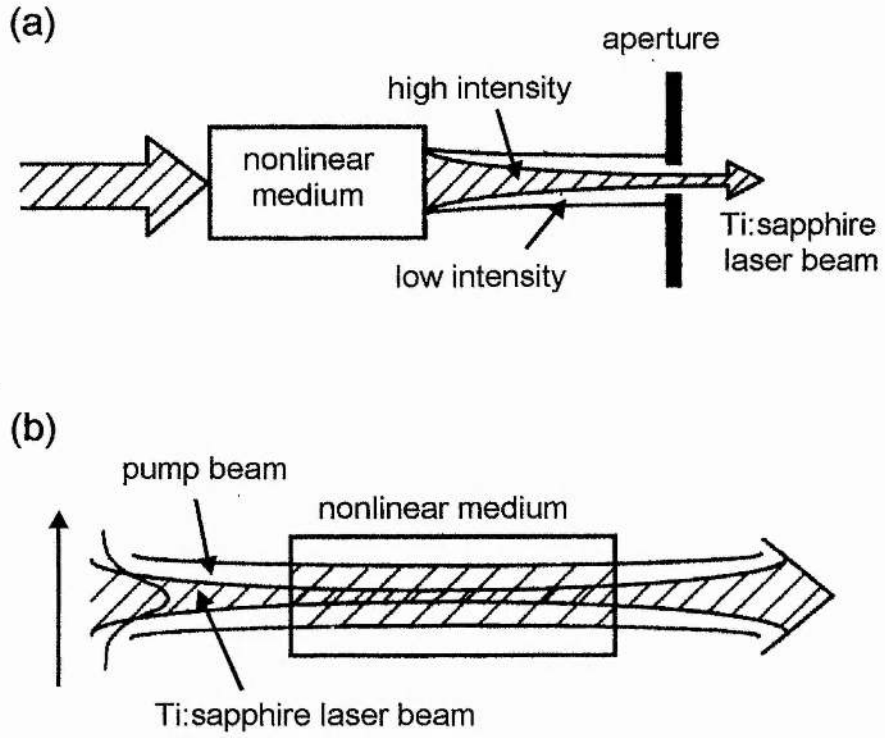

Figure 9: Self-focusing of a laser beam for (a) hard aperture self-modelocking and (b) soft aperture self-modelocking.

This lensing effect is a result of the Kerr nonlinearity present in the medium hence the technique of self-modelocking is also called Kerr lens modelocking. The success of this technique has resulted in the demonstration of self-modelocking in a number of other solid-state media including Cr:LiSAF[17-19], Cr:LiSCaF[20], Cr:LiCaF[21], Cr:LiSGaF[22], Cr:YAG[23], Cr:forsterite[24], Nd:glass[25], Nd:YAG[26], and Nd:YLF[27].

Self-modelocking can start spontaneously from the random fluctuations of cw oscillation. It is often, however, more convenient to induce the self-modelocked

behaviour. There are various techniques for achieving this including mirror tapping, which causes rapid changes in the cavity length. This works well when no intracavity elements are present other than the laser crystal and dispersion compensating prisms. A shaking mirror can also be used either intracavity or extracavity to initiate self-modelocking. The periodic movement of the mirror provides sufficient amplitude modulation for the laser to favour and sustain self-modelocked operation.

Once modelocking has been achieved it is important that the output from a laser or an OPO can be both measured and monitored. There are a number of methods for achieving this and these are described in the remainder of this chapter.

Ultrashort Light Pulse Characterisation

The second harmonic generation autocorrelator is most effective for measuring pulses with durations of the order of femtoseconds. The initial demonstration of this scheme was in 1966[28] and it is this technique which is considered first. This is followed by a discussion of the use of light-emitting diodes and photodiodes in second harmonic generation autocorrelation. The radio-frequency spectrum analyser and the optical spectrum analyser are discussed in terms of the pulse information that they can provide and the final pulse measurement technique discussed is that of frequency-resolved optical gating. The chapter concludes with a detailed account of the optical effects that influence the output from an ultrashort pulse laser or OPO and methods for controlling them with regard to minimising the available pulse duration.

The Second Harmonic Generation Autocorrelator

The SHG autocorrelator achieves femtosecond accuracy in measuring pulse durations, by converting the measurement of times of the order of femtoseconds into the simpler task of measuring a distance, which is easily within the range of laboratory instruments. This succeeds because a pulse of 100 fs duration has an optical path length of the order of 30 μm. A schematic diagram of a typical SHG autocorrelator used for the temporal pulse measurements in this work is shown in Figure 12.

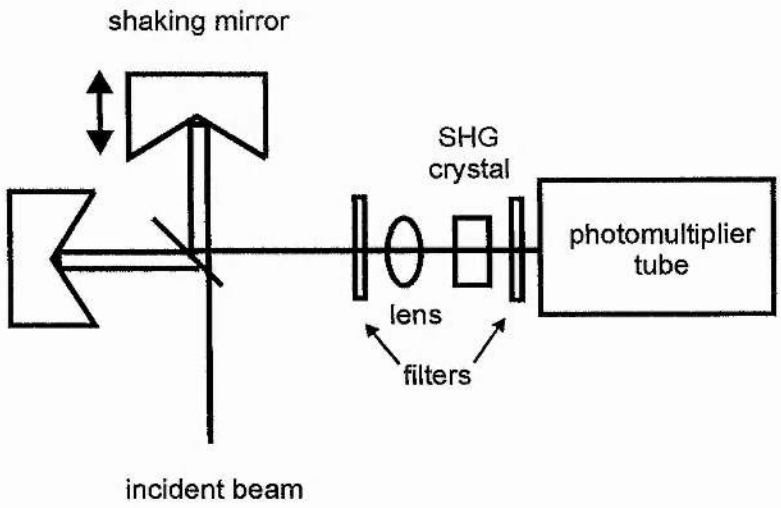

Figure 12: Schematic diagram of an SHG autocorrelator system.

The output pulses from the laser are sent into a Michelson interferometer-type optical delay system. One arm consists of a retroreflector mounted on a loudspeaker, which is scanned at ~20Hz. The length of this arm varies as the loudspeaker vibrates. The length of the other arm is fixed. The light pulses from each arm of the interferometer are recombined at a beamsplitter and then focussed tightly into a nonlinear crystal

such as β–barium borate (BBO). The pulses at this point are spatially collinear and overlapped in time. The second harmonic light passes through filters, which eliminate any fundamental or stray background light, and is detected by a photomultiplier tube.

The degree of overlap of the pulses when the beam is recombined, produces a corresponding amount of second harmonic light and this is recorded as a function of delay. The resultant second harmonic signal consists of a background intensity level, due to the separate signals from each arm, plus an enhanced signal when the pulses overlap. This enhanced signal, as a function of the relative delay between the two arms of the interferometer, represents the intensity autocorrelation of the pulse.

Calibration of the autocorrelator is achieved by translating the static retroreflector a known distance and calculating the corresponding temporal delay of the pulse.

For collinear autocorrelation, the intensity autocorrelation function of the light pulse is given by the equation

$$G(\tau) = 1 + 2\frac{\int_{-\infty}^{+\infty} I(t)I(t-\tau)dt}{\int_{-\infty}^{+\infty} |I(t)|^2 dt},$$

where $I(t)$ is the intensity distribution of the pulse and τ is the time delay. The pulse duration $\Delta\tau_p$ is obtained by measuring the full-width half-maximum (FWHM) duration of the autocorrelation function Δt and dividing it by a constant K,

$$\Delta\tau_p = \frac{\Delta t}{K}.$$

The value of K depends on the assumed pulse shape. The intensity autocorrelation pulse envelope has a peak-to-background ratio of 3:1, and it is the intensity autocorrelation function that is used to determine the duration of the laser pulses.

The accuracy of assuming an appropriate pulse shape can be checked by comparing the time-bandwidth product of the measured pulse spectrum, to the calculated value for the chosen pulse profile, provided that the pulses are not frequency chirped. Values for the Fourier transform-limited time-bandwidth product $\Delta\tau_p\Delta\nu$, and the constant K for two common pulse profiles, are shown in Table 2.

Pulse Profile	**I(t)**	$\Delta\tau_p\Delta\nu$	K
sech^2	$\text{sech}^2\left(\frac{t}{T}\right)$	0.315	1.543
Gaussian	$e^{-\left(\frac{t^2}{T^2}\right)}$	0.441	1.414

Table 2: Time-bandwidth products and the value of K for some common pulse profiles.

The intensity autocorrelation function is symmetric and so is averaged with time, and that relies on assuming a pulse shape. This must be verified by ensuring that the time-bandwidth product for the measured pulse gives a value close to that presented in the table, for the assumed pulse shape. If the calculated value for the time-bandwidth product is larger than expected, then the pulses are likely to be frequency-chirped.

The interferometric autocorrelation function is not averaged with time, so the high

frequency components associated with frequency chirp are not filtered out. The interferometric autocorrelation function is given by the equation

$$g(\tau)=\frac{\int_{-\infty}^{+\infty}\left|\left\{E(t)e^{i\omega t}+E(t-\tau)e^{i\omega(t-\tau)}\right\}^2\right|^2 dt}{2^4\int_{-\infty}^{+\infty}E^4(t)dt}$$

In interferometric autocorrelation the individual optical cycles within the pulse envelope are resolved. Unlike intensity autocorrelations, where all the phase information is averaged out, varying degrees of frequency chirp can produce distinctive patterns in interferometric autocorrelation and examples are given in Figure 13. The leading and trailing edges of a frequency-chirped pulse are not coherent and thus do not interfere constructively. Consequently the interferometric autocorrelation function collapses over these parts of the pulse.

A chirp-free interferometric autocorrelation can also provide direct information about the pulse duration, because the separation of each fringe corresponds to a single optical cycle at the centre frequency of the pulse. The interferometric autocorrelation pulse envelope has a peak-to-background ratio of 8:1.

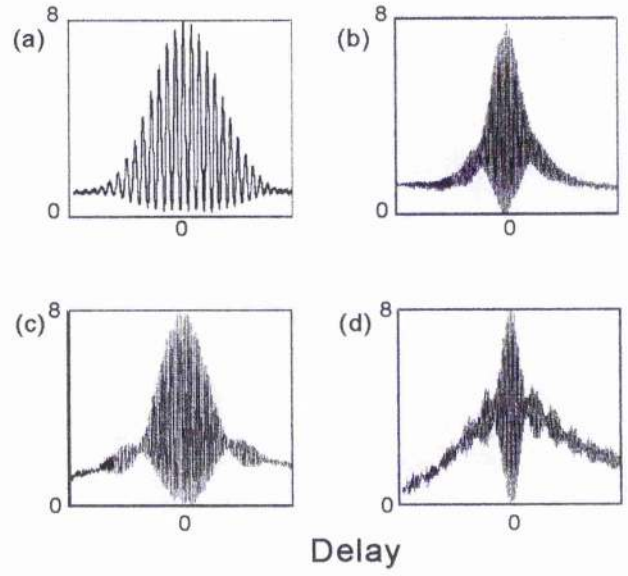

Figure 13: Distinctive interferometric autocorrelation patterns produced for a light pulse that is (a) transform-limited and (b)-(d) increasingly frequency-chirped.

Light-Emitting Diodes and Photodiodes for Autocorrelation

Although in widespread use, the SHG-autocorrelator does have its drawbacks. As a detector it is not well suited to every ultrashort pulse laser or OPO system. The main problem is that appropriate nonlinear crystals for SHG in the UV and MIR are not available. Even at wavelengths where the SHG-autocorrelator works well there can still be disadvantages when measuring particularly short pulses due to the pulse broadening introduced in the SHG crystal.

The SHG crystal must be kept to a minimum thickness to avoid the effects of temporal walk-away and Poynting vector walk-off. This means that conversion efficiencies are low. Further, the crystal must be kept thin to prevent dispersive

broadening of the pulse that is to be measured. Any single nonlinear crystal will only operate well at a specific wavelength due to its phasematching properties and the limits of the spectral bandwidth. Different crystals are thus required for characterising light pulses from different laser or OPO systems. Photomultiplier tubes work well, particularly when output powers are low. However, photomultiplier tubes are bulky, they require a high-voltage power supply to operate, they are sensitive to background light and so have to be carefully enclosed and are expensive in comparison to the available alternatives.

Light emitting diodes (LEDs) and photodiodes[29-31] have recently been proven to be very effective in producing high quality interferometric autocorrelation traces. Autocorrelation systems that incorporate LEDs or photodiodes in place of photomultiplier tubes are both low-cost and compact. A high voltage power supply is not required and problems associated with phasematching and dispersion are eliminated. These systems allow the straightforward measurement of femtosecond pulses over a broad range of wavelengths.

An LED used as an unbiased photodiode, or a photodiode, exhibits a nonlinear power-dependent response that can be used for sensitive detection and characterisation of femtosecond pulses. In this work, an extended InGaAs photodiode[32] was used to obtain autocorrelation measurements of the idler pulses form the various OPOs and a GaAs LED was used for some of the autocorrelation measurements of the signal pulses.

The basic structure of an LED is shown in Figure 14. The LED consists of an active semiconductor structure contained within a small metal cup. The emitted photons can then be reflected in the forward direction. At the other end, the diode is connected to an electrode with a fine bond wire, and all the components are enclosed within a plastic dome. To ensure maximum transmission of the light to the diode, and minimise the effects of group velocity dispersion, the plastic casing has to be polished down very close to the wire. Ultrahigh brightness devices must be used in preference to standard LED structures. They are more suitable because the incoming light does not have to propagate through an extra surface layer of semiconductor material before reaching the active region and thus any losses due to absorption are minimised.

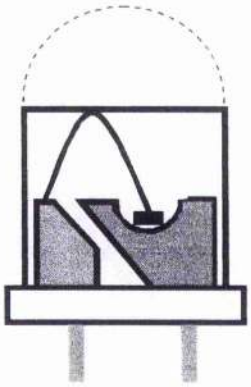

Figure 14: The basic structure of a light-emitting diode (LED) with the casing polished down.

The choice of diode material is vitally important. The bandgap energy must be sufficiently large to prevent absorption of single photons, otherwise the nonlinear response will not be seen. The bandgap energy is roughly equivalent to the photon energy of the peak emission wavelength of the LED, so the wavelength it can measure will be longer than the specified emission wavelength. Once an appropriate LED has been selected, the electrodes can be connected directly to an oscilloscope using a coaxial cable and connectors.

Multiphoton absorption[33,34] involves the transition of an electron from the low valence band to the higher conduction band and is a result of the absorption of two or more photons from an incident light beam. The higher the intensity of the incident light, the more significant this effect becomes although it is the frequency of the light that determines if the effect will occur at all. Figure 15(a) shown the cross-section of a photodiode. The P-layer at the active surface and the N-layer at the substrate form a PN-junction, which acts as a photoelectric converter. The neutral region between the P- and N-layers is called the depletion layer. The spectral response and the frequency response of a photodiode can be controlled by varying the thickness of the P-layer, the N-layer and the bottom N^+-layer, as well as varying the doping concentration of the semiconductor.

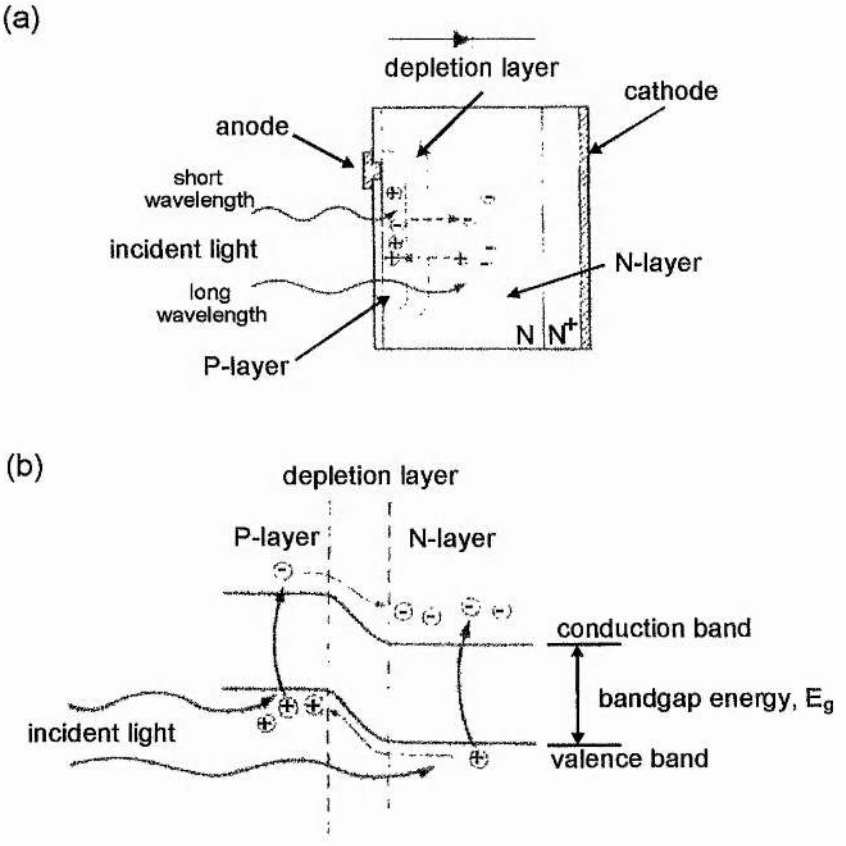

Figure 15: (a) The cross-section of a photodiode. (b) The PN-junction within a photodiode[33,34].

When a photon strikes a photodiode, an electron within the crystal structure becomes excited. If the energy of the photon is larger than the bandgap energy, E_g, the electrons are pulled up into the conduction band, leaving holes in their place in the valence band. This is shown in Figure 15(b). These electron-hole pairs occur throughout the P-layer, the depletion layer and the N-layer materials. In the depletion layer, the electric field accelerates the electrons towards the N-layer and the holes towards the P-layer. The electrons from the electron-hole pairs generated and the electrons from the P-layer are left in the N-layer conduction band. At the same time, the holes are diffused through the N-layer to the depletion layer. There they are accelerated forwards and are collected by the valence band. The number of electron-hole pairs generated is proportional to the intensity of the incident light. The result is that the P-layer becomes positively charged and the N-layer becomes negatively charged. If an external circuit is connected between the N- and P- layers a current will flow.

The mechanism for the photodetection using LEDs and photodiodes depends on two-photon absorption. In two-photon absorption the optical signal at the fundamental wavelength is directly converted to a photocurrent. This only happens if the light intensity is sufficient. The two photons are absorbed in the valence band of the semiconductor and this provides the energy for promotion of an electron to the conduction band. Hence, the photons must have a minimum energy of half the bandgap energy, E_g, for this process to occur. In terms of wavelength the chosen LED should have a peak emission wavelength of at least half the wavelength which is to be measured.

The technique of second-harmonic generation autocorrelation is a useful means of measuring the temporal output from a laser or an optical parametric oscillator. However, only once this information is combined with a measurement of the spectral output from the laser or optical parametric oscillator can true the characterisation of an ultrashort pulse system be achieved. Methods for measuring the RF spectrum and the optical spectrum of the output from a laser are described next.

The RF Spectrum Analyser

Further valuable information about the pulses from a modelocked laser can be obtained from the radio frequency (RF) power spectrum of the laser output It is important to be able to make an accurate measurement of the laser cavity length when regenerative modelocking is employed. Analysis of the mode-beating of the longitudinal modes of the cw laser allows an accurate calculation of the laser cavity length. This information is available from the RF spectrum, which is also a convenient means of checking that regenerative modelocking is maintained during optimisation of the laser cavity elements for self-modelocking. Throughout the work with the regeneratively initiated self-modelocked Ti:sapphire laser, the fast photodiode of the regenerative-initiation circuit was used in conjunction with an HP70000 System RF spectrum analyser to monitor the RF spectrum of the laser output. It is also possible to measure the pulse timing jitter[35] of the output from a modelocked laser using an RF spectrum analyser, although this is not considered in this work.

The Optical Spectrum Analyser

The optical spectrum of an ultrashort light pulse also provides essential information, and combined with the temporal pulse data, allows the calculation of the time-bandwidth product of the pulse. Additional information about the pulse, such as the presence of a cw spike or evidence of multiple pulsing can also be found from its optical spectrum.

The optical pulse spectra of the output from the Ti:sapphire lasers used in this work were measured using a fibre-coupled Anritsu Wiltron MS96A optical spectrum analyser (OSA). The optical pulse spectra of the output from the OPOs used in this work were measured using a Rees E200 Series laser spectrum analyser (LSA)[36]. This instrument is capable of monitoring the output of ultrafast laser systems at wavelengths beyond the cut-off of the OSA. The LSA was operated in conjunction with an oscilloscope to provide a real-time display of the optical pulse spectrum.

Frequency Resolved Optical Gating

Techniques such as intensity and interferometric autocorrelation require assumptions to be made about the expected shape of the laser pulse and this can be limiting. The more recently developed technique of frequency resolved optical gating (FROG)[37] allows the direct determination of the full intensity and phase information, of a single femtosecond pulse, without making assumptions, in a single shot and using an optical system that is not complex. The experimental FROG-trace, produced by such a

system, is related to the pulse spectrogram, from which the complete complex electric field of the pulse can be determined, using an algorithm that generates accurate results in a short time.

The FROG technique involves measuring the spectrum of a light pulse as a function of the delay between two input light pulses. These two input pulses are produced when the pulse to be measured is split into two replicas; the pulse to be measured and a gate pulse. A variable delay is then introduced between them. The pulses are then recombined whilst the subject of an instantaneous nonlinear effect. FROG can use almost any instantaneous optical nonlinearity, with the most common geometries being polarisation gate (PG), self-diffraction (SD) and second harmonic generation (SHG)[38].

Polarisation gating and self-diffraction rely on third-order nonlinear effects, and consequently require high intensities to produce a significant signal electric field. This can be a problem in both low power laser systems and synchronously-pumped femtosecond OPOs. For this reason, SHG-FROG was used in this work and this is the only FROG technique that will be considered further.

The resulting signal is then spectrally resolved and recorded, and a plot of the intensity of the pulse as a function of both delay and frequency is generated. Mathematically this can be described as

$$S_E(\omega,\tau)=\left|\int_{-\infty}^{\infty}E(t)g(t-\tau)\exp(-i\omega t)dt\right|^2. \qquad (1.1)$$

$E(t)$ is the electric field of the pulse, $g(t-\tau)$ describes the gate pulse and τ is the delay. This is the pulse spectrogram. FROG gates the optical pulses to be measured with replicas of themselves. It can be shown that the spectrogram includes all intensity and phase information of the pulse, and that the complex electric field of the pulse can be recovered from it. The experimentally generated FROG-trace is intuitive, visually appealing and can yield quantitative information about the temporal and spectral width and chirp of the pulse.

The optical signal, $E_{sig}(t,\tau)$, has a mathematical form that depends on the particular nonlinear response used to gate the light pulses. As a result, the exact shape of the pulse spectrogram also depends upon the choice of gating technique from which it was generated. The optical geometries required for each of the FROG techniques already mentioned are shown in Figure 15, and the signal electric field produced in each case is also given.

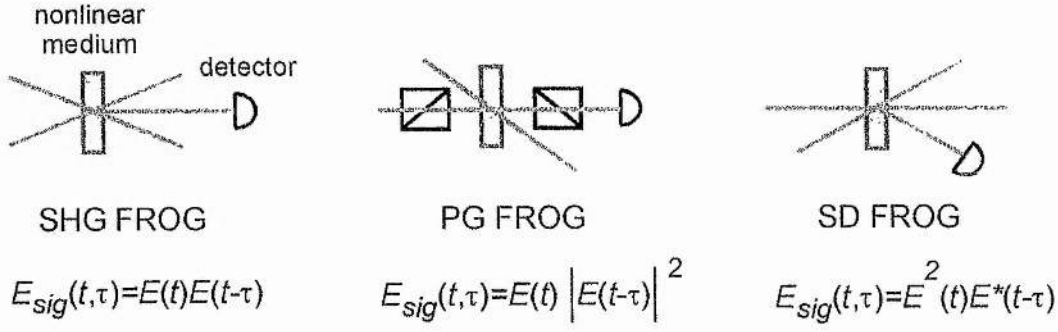

Figure 15: The optical geometries used in second harmonic generation FROG, polarisation gate FROG and self-diffraction FROG, along with the signal electric field, $E(t,\tau)$, produced in each case.

The technique of SHG-FROG was first demonstrated by Paye et al in 1993[39]. At that time it was known as spectrally resolved autocorrelation because the individual spectra recorded for each value of delay was used to construct the SHG-FROG trace. Many experimental FROG systems operate by progressively recording spectra for particular delay values and building up the FROG-trace from them. In a real-time system the FROG-trace display is constantly updated. This dramatically reduces the acquisition time and allows the spectral and temporal pulse characteristics to be constantly monitored.

The FROG system can be described more specifically as having two separate components. The first is the optical setup used to obtain the pulse spectrogram, and the second is the computer algorithm used to retrieve the pulse information from the spectrogram.

The optical setup of an experimental SHG-FROG system is illustrated in Figure 16. The system which will be described was constructed to characterise the output from a self-modelocked Ti:sapphire laser. Details of this experiment are given in Chapter 3. The first component of the SHG-FROG system was a standard Michelson interferometer-type optical delay arrangement, comprising a beamsplitter and two retroreflectors. One of the retroreflectors was mounted on a loudspeaker and the other was mounted on a calibrated translation stage. This was used to provide a continually scanning delay between the two input pulses.

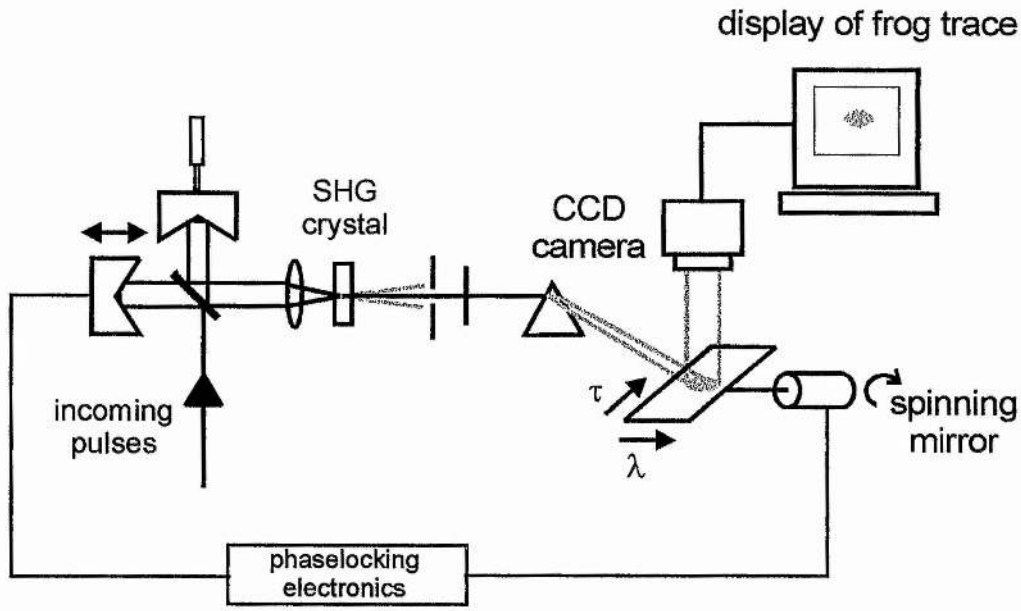

Figure 16: Optical setup for the experimental SHG-FROG system.

A lens was used to focus the output from the Michelson interferometer-type optical delay arrangement, into a frequency-doubling crystal to generate second harmonic light. The SHG-FROG system had to be aligned for noncollinear phasematching to eliminate any background light level and allow the pulse to be successfully retrieved by the algorithm. (The background light level seen in SHG autocorrelation results from the collinear phasematching geometry.)

The two replicas of the input beam were separated laterally prior to passing through the lens, but were made to cross over on focussing, at an angle, through the doubling crystal. The combined intensities of the forward propagating component of each beam was sufficient to generate second harmonic light in the forward direction. The two deviating side beams were blocked using a pinhole, and the forward component, $E_{sig}(t,\tau)$, was then spectrally dispersed using a prism. A spinning mirror was used to

sweep the dispersed spectrum across the surface of a CCD camera to create a frequency scan. The spinning mirror was phaselocked to the loudspeaker so that the frequency scan and the delay scan were always synchronous. This was achieved by using a small motor to spin the mirror freely. An error signal was derived, by comparing the frequency of spin with the frequency of the loudspeaker, and this signal was fed back into a loop that adjusted the loudspeaker frequency to minimise the error value. This meant that the FROG-trace detected by the camera was both complete and continuous.

A video monitor, updated at a rate of approximately 15 Hz, was used to display the FROG-trace and a frame-grabber was used to select and digitise the FROG-trace producing a 512 by 512 array of data. Image processing was carried out to eliminate background noise and to centre the trace in the middle of the array. The trace was then calibrated temporally in the same way as for an autocorrelation trace. Spectral calibration was achieved by measuring the dispersed output with a monochromator and the bandwidth and peak wavelength corresponding to zero delay was determined. The retrieval algorithm was then applied to the data set to obtain the pulse information.

The generated signal electric field was spectrally dispersed and recorded as a function of the delay, τ. For SHG-FROG, the spectrogram of Equation (1.1) becomes the FROG-trace so that

$$I_{FROG}(\omega,\tau)=\left|\int_{-\infty}^{\infty}E(t)E(t-\tau)\exp(-i\omega t)dt\right|^2 .$$

The electric field of the pulse, $E(t)$, was obtained from the electric field of the signal, $E_{sig}(t,\tau)$, or from the FROG-trace, $I_{FROG}(\omega,\tau)$ using two-dimensional phase-retrieval, which involved two-dimensional Fourier transforms. Two-dimensional phase-retrieval problems can be solved to produce a unique result and this is why the FROG system works so well. For a particular trace, there is a single unique pulse that can be retrieved by the algorithm hence this pulse must take the exact form of the original pulse that produced the trace in the first place.

The phase retrieval was achieved using an iterative Fourier transform algorithm, and two constraints were applied to force it to converge and yield the correct solution. The first algorithm of this kind was developed by Trebino and Kane[40]. This algorithm was improved to make it more compatible with the SHG-FROG system and an outline of its format is given in Figure 17. An initial guess, $E(\tau)$, was made as to the expected shape and form of the pulse to be measured and from this the signal electric field, $E_{sig}(t,\tau)$, was calculated. Fourier transformation of $E_{sig}(t,\tau)$ converted the signal electric field to $E_{sig}(\omega,\tau)$ in terms of frequency. The first constraint was applied at this stage: the magnitude of $E_{sig}(\omega,\tau)$ was replaced with the magnitude of the measured FROG trace, $E'_{sig}(\omega,\tau)$. The inverse Fourier transform then converted the signal electric field to $E'_{sig}(t,\tau)$, so that the second constraint could be applied.

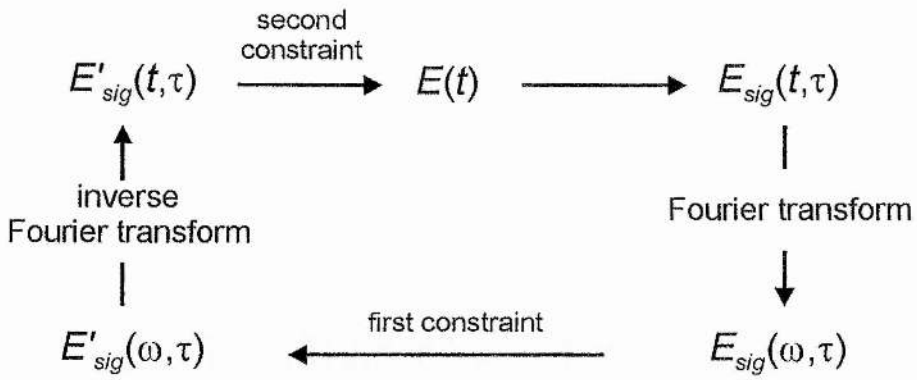

Figure 17: Outline of the algorithm used by the SHG-FROG system.

This resulted in an improved guess pulse and the algorithm continued until it had converged sufficiently and the pulse could be identified. After each iteration of the algorithm, the FROG-trace of the guess pulse was calculated and compared with the FROG-trace that was actually measured. In this way the convergence of the algorithm could be monitored by calculating an error G, described mathematically by

$$G = \sqrt{\frac{1}{N^2}\sum_{\omega,\tau=1}^{N}\left(I_{FROG}(\omega,\tau) - \left|E_{sig}(\omega,\tau)\right|^2\right)^2} .$$

There were N frequency values to describe the spectrum at each of the N delay times. If the generated array of data is not square (i.e. $N \times N$), it is necessary to scale the experimental FROG-trace prior to application of the algorithm. The reason is that fast Fourier transformation requires that the increment in delay values, $\delta\tau$, must be related to the increment in frequencies, $\delta\upsilon$, by

$$\delta\nu = \frac{1}{N\delta\tau} .$$

The value of G was used to monitor the progress of the algorithm. If G became small after a certain number of iterations then the algorithm did converge. In practice, it was

found that not all pulses could be retrieved using a single algorithm and the system was more successful when a combination of two different types of algorithm was used. In this case, if the value of G had not reduced significantly after a certain number of iterations, the algorithm would swap to a different type to increase the chances of convergence. The combined system worked well and pulses were retrieved quickly in this way. Details of the mathematics involved can be found in references 41-43.

The SHG-FROG technique is limited in the same way as SHG autocorrelation and has one further significant drawback. The SHG-FROG trace is symmetric in terms of delay, about $\tau=0$. This means that a delay of $-\tau$ produces the same signal electric field as a delay of $+\tau$. Hence, the FROG-trace of $E(t)$ is the same as the FROG-trace of $E(-t)$.It is therefore not possible to determine the leading and trailing edges of the pulse, in terms of time, from the SHG FROG-trace. The only exception to this, is that if the source of chirp is known, for example group velocity dispersion introduces positive chirp, then this information can be used to determine the leading and trailing edges of the pulse. This limitation is unique to the SHG-FROG system and the techniques of PG-FROG and SD-FROG do not suffer from this problem.

Theoretical examples of FROG-traces, measured using the three techniques mentioned are shown in Figure 18. They include a transform-limited pulse, a pulse that is linearly chirped, a pulse that has undergone self-phase modulation and a pulse that has suffered both GVD and SPM. It is clear from these examples that the SHG-FROG trace is always symmetric in delay, unlike the PG- and SD-FROG traces. A

graph of the variation of the pulse temporal intensity (circles) and phase (squares) determined by SHG-FROG, for a transform-limited pulse is also shown. The technique of frequency-resolved optical gating is thus a powerful method for measuring the full amplitude and phase of the electric field of an ultrashort optical pulse.

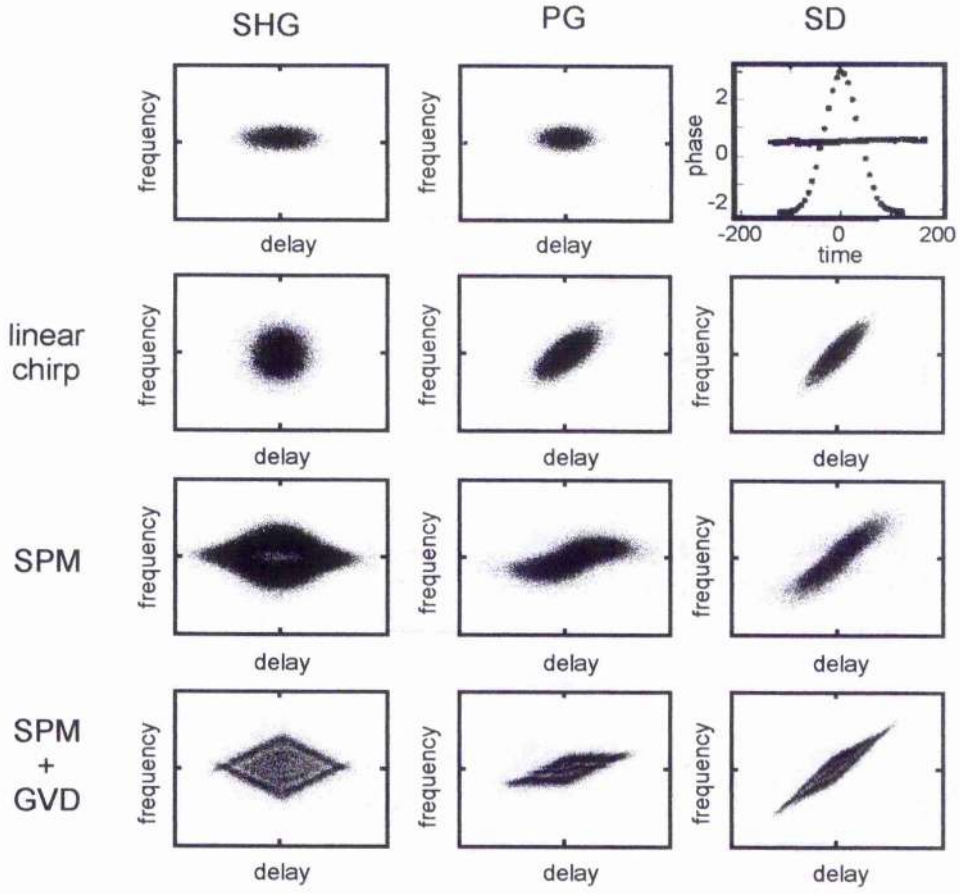

Figure 18: Theoretical examples of FROG traces for several common ultrashort pulses. The variation of the pulse temporal intensity (circles) and phase (squares) are also shown for a transform-limited pulse.

Conclusions

The purpose of this chapter was to explain the theory of ultrashort pulse generation

with regard to the Ti:sapphire laser. The optical properties of Ti:sapphire were discussed along with the principles of laser oscillation and pulse generation. The techniques used to modelock the lasers used in the experimental work, to follow, were also considered. The second part of the chapter dealt with typical measurement techniques for characterising femtosecond optical pulses from a laser or an OPO, and concluded with a detailed explanation of frequency-resolved optical gating, the newest of these techniques.

Two typical femtosecond Ti:sapphire laser systems are characterised in Chapter 3, and consideration is given to their suitability as pump sources for an optical parametric oscillator. Further to this, the Ti:sapphire lasers used as pump sources for the OPOs described in experimental Chapters 4, 5, and 6 are also discussed at the beginning of each chapter. The pulse characterisation techniques are also relevant to the femtosecond OPO work, as the output from each OPO was characterised using second harmonic generation autocorrelation.

Chapter 1

References

1. P.F Moulton, *Optics News* **8**, 9 (1982)
2. P.F Moulton, *J. Opt. Soc. Am. B* **33**, 125 (1986)
3. R.R Joyce and P.L Richards, *Phys. Rev.* **179** 375 (1969)
4. W.R Rappaport, C.P Khattak, *Appl. Optics* **27** 2677 (1988)
5. P Albers, E Stark and G Huber, *J. Opt. Soc. Am. B* **3** 134 (1986)
6. T.R Steele, D.C Gerstenberger, A Drobshoff and R.W Wallace, *Opt. Lett.* **16** 399 (1991)
7. J Harrison, A Finch, D.M Rines and P.F Moulton, *Opt. Lett.* **16** 581 (1991)
8. A Sanchez, A.J Strauss, R.L Aggarwal, R.E Fahey, *IEEE J. Quantum Electron.* QE-**24** 995 (1988)
9. G.T Maker and A.I Ferguson, *Opt. Lett.* **15** 375 (1990)
10. D.E Spence, J.M Evans, W.E Sleat and W Sibbett, *Opt. Lett.* **16** 1762 (1991)
11. G.R Huggett, *Appl. Phys. Lett* **13** 186 (1968)
12. D.E Spence, P.N Kean and W Sibbett, *Opt. Lett.* **16** 42 (1991)
13. B.E Lemoff and C.P.J Barty, *Opt. Lett.* **17** 1367 (1992)
14. T Babec, P.F Curley, C Spielmann, E Wintner and A.J Schmidt, *J. Opt. Soc. Am. B* **10** 1029 (1993)
15. M Piché and F Salin, *Opt. Lett.* **18** 1041 (1993)
16. G Cerullo, S De Silvestri and V Magni, *Opt. Lett.* **19** 1040 (1994)
17. M.J.P Dymott and A.I Ferguson, *Opt. Lett.* **19** 1988 (1994)
18. M.J.P Dymott and A.I Ferguson, *Opt. Lett.* **20** 1157 (1995)

19. J.M Evans, D.E Spence, W Sibbett, B.H.T Chai and A Miller, *Opt. Lett.* **17** 1447 (1992)

20. H.S Wang, P LiKamWa, J.L Lefaucheur, B.H.T Chai and A Miller, *Opt. Commun.* **110** 679 (1994)

21. P LiKamWa, B.H.T Chai and A Miller, *Opt. Lett.* **17** 1438 (1992)

22. V.P Yanovsky, F.W Wise, A Cassanho and H.P Jenssen, *Opt. Lett.* **20** 1304 (1995)

23. A Sennaroglu, C.R Pollack and H Nathel, *Opt. Lett.* **19** 390 (1994)

24. A Seas, V Petricevic and R.R Alfano, *Opt Lett.* **18** 891 (1993)

25. U Keller, T.H Chiu and J.F Ferguson, *Opt. Lett.* **18** 1077 (1993)

26. K.X Liu, C.J Flood, D.R Walker and H.M van Driel, *Opt. Lett.* **17** 1361 (1992)

27. M Ramaswamy, A.S Gouveianeto, D.K Negus, J.A Izatt and J.G Fujimoto, *Opt. Lett.* **18** 1825 (1993)

28. M Maier, W Kaiser and J.A Giordmaine, *Phys. Rev. Lett.* **17** 1275 (1966)

29. A.E Siegman, Lasers (University science books, California, 1986) Ch 9

30. G.P Agrawal, Nonlinear Fibre Optics (Academic Press, London 1989) Ch 3

31. D. T. Reid, C. McGowan, M. Ebrahimzadeh and W. Sibbett, *IEEE J. Quantum. Electron.* **33**, 1, (1997)

32. D.T Reid, M Padgett, C McGowan, W.E Sleat and W Sibbett, *Opt. Lett.* **22** 233 (1997)

33. E.W Van Stryland, H Vanheerzeele, M.A Woodall, M.J Soileau, A.L Smirl, S Guha and T.F Bogess, *Optical Engineering* **24** 613 (1985)

34. A Miller, Nonlinear Optics in Signal Processing, A Miller (Engineering Aspects of Laser Series, Series editor, Dr T.A Hall, Chapman-Hall) Ch 3

35. L.P Barry, P.G Bollond, J.M Dudley, J.D Harvey and R Leohardt, *Electron. Lett.* **32** 1922 (1996)

36. Rees Instruments Ltd, Thornbrook, Weyside Park, Cattleshall Lane, Godalming, Surrey, GU7 1XE

37. D.J Kane and R Trebino, IEEE J. *Quantum Electron.* **29** 571 (1993)

38. K.W Delong, R Trebino and D.J Kane, *J. Opt. Soc. Am. B* **11** 1595 (1994)

39. J Paye, M Ramaswamy, J.G Fujimoto and E.P Ippen, *Opt. Lett.* **18** 1946 (1993)

40. R Trebino and D.J Kane, *J. Opt. Soc. Am. A* **10** 1107 (1993)

41. K.W Delong, R Trebino, J Hunter and W.E White, *J. Opt. Soc. Am. B* **11** 2206 (1994)

42. K.W Delong, D.N Fittinghoff, R Trebino, B Kohler and K Wilson, *Opt. Lett.* **119** 2152 (1994)

43. K.W Delong and R Trebino, *J. Opt. Soc. Am. A* **11** 2429 (1994)

CHAPTER 2

Nonlinear Optics and Optical Parametric Oscillation

In chapter 1 the subject matter related to the generation of ultrashort light pulses from a laser and various techniques for characterising ultrashort light pulses were described. This chapter concerns the operation of an ultrashort pulse optical parametric oscillator (OPO) and the various methods for achieving this. In order that the process of optical parametric oscillation is fully understood, some discussion of linear and nonlinear optics is required, and this is mentioned at the outset. The properties of nonlinear crystals are also discussed and phasematching techniques are explained together with the technique of periodic-poling of nonlinear optical crystals. The chapter concludes with an account of the effects of second and third-order dispersion and methods for second and third-order dispersion compensation.

Nonlinear Polarisation and the Coupled Wave Equations

Nonlinear optical effects become apparent in certain materials when they are subjected to an intense electric field, such as the output from a pulsed laser. This interaction of light with matter is described by Maxwell's equations and the precise nature of any interaction is determined by the specific properties of the light and the medium involved.

If an intense light beam is applied to a dielectric material, the electric field associated with the light causes the electrons within the dielectric to become polarised with respect to the nuclei. This causes an overall polarisation to be induced within the dielectric. When the electric field strength of the applied beam is small, the degree of induced polarisation is proportional to the incident field and the relationship between the electric field strength, E, and the polarisation, P, is

$$P = \varepsilon_o \chi^{(1)} E .$$

ε_o is the permitivity of free space. $\chi^{(1)}$ is the linear susceptibility of the material, which relates P to E, and is responsible for linear optical effects such as the refractive index, dispersion and birefringence of the material. This is the basis of linear optics. For higher electric field strengths, comparable to the interatomic field strength within the dielectric, the relationship between P and E is no longer linear and can be described by the equation

$$P = \varepsilon_o \chi^{(1)} E + \chi^{(2)} E^2 + \chi^{(3)} E^3 + \ldots\ldots,$$

where $\chi^{(i)}$ is a tensor which describes the higher-order nonlinear susceptibilities of the medium. Vectors P and E are not in general parallel, and hence tensors can be used to describe their properties more appropriately. The values of $\chi^{(i)}$ decrease significantly as the value of i increases, and this is why a high electric field strength such as that generated by a pulsed laser, is necessary for nonlinear optical effects to become significant in a material. $\chi^{(2)}$ is the second order nonlinear susceptibility which governs the three-wave mixing processes of second harmonic generation, sum- and difference-frequency mixing and optical parametric generation. The third-order nonlinear susceptibility, $\chi^{(3)}$, is responsible for cubic nonlinear effects such as third harmonic generation and the optical Kerr effect. Higher order effects are not discussed here.

If the nonlinear polarisation of a dielectric is approximately given by the equation

$$P_{NL} = \chi^{(2)} E^2 , \tag{2.1}$$

then the effect on the nonlinear medium, when an electromagnetic wave propagates through it, can be considered. For a dielectric material, Maxwell's equation relates the variation of the polarisation with time and the variation of the electric field with time in such a way that:

$$\nabla^2 E = \mu\varepsilon_o \frac{\partial^2 E}{\partial t^2} + \mu \frac{\partial^2 P}{\partial t^2} .$$

By including the polarisation described by Equation (2.1) and assuming that all waves propagate in the z-direction, then the resulting second-order Maxwell equation is:

$$\frac{\partial^2 E}{\partial z^2} = \mu\varepsilon \frac{\partial^2 E}{\partial t^2} + \mu \frac{\partial^2 (\chi^{(2)} E^2)}{\partial t^2} ,$$

where $\varepsilon=\varepsilon_o(1+\chi^{(2)})$. It is the solution of this equation that determines the behaviour of the light as it propagates through the dielectric medium.

The three waves of a second-order nonlinear optical process are referred to as ω_1, ω_2, and ω_3, and conservation of energy requires that the frequencies of these three waves are related by:

$$\omega_1 + \omega_2 = \omega_3 . \tag{2.2}$$

ω_3 is the highest frequency (shortest wavelength) and ω_1 is the lowest frequency (longest wavelength). Hence there are a number of interactions that are possible. Equation (2.2) describes sum-frequency mixing, where two longer wavelengths are used to generate a shorter one. Second harmonic generation is a special case of sum-frequency mixing in

which $\omega_1=\omega_2$. Difference-frequency mixing, on the other hand, is described by Equation (2.3) and has

$$\omega_3 - \omega_2 = \omega_1 . \tag{2.3}$$

In optical parametric generation a single wave at a short wavelength is used to produce two waves each with longer wavelengths than the original, and

$$\omega_3 = \omega_1 + \omega_2 . \tag{2.4}$$

By convention the waves are given names according to wavelength. The shortest wavelength is the pump, ω_p (ω_3), which generates two new wavelengths, the shorter of which is the signal, ω_s (ω_1), and the longer of which is the idler, ω_i (ω_2). If $\omega_1=\omega_2$ the process is said to be degenerate.

For the case of a three-wave interaction, the total instantaneous electric field is given by the sum of the individual electric fields of ω_1, ω_2, and ω_3, so that

$$E(z,t) = E_1(z,t) + E_2(z,t) + E_3(z,t) . \tag{2.5}$$

If the waves E_i(z,t) are plane waves, their spatial and temporal dependence can be written as

$$E_i(z,t) = \frac{1}{2}(E_i(z)e^{i(k_i z-\omega t)} + c.c.), \tag{2.6}$$

where wave i has a wave vector k_i.

When Equation (2.6) is substituted into Equation (2.5), the resulting equation can be split into three parts, each of which describes the behaviour of one of the waves. Details of the

mathematics involved and the approximations made can be found in references 1-5. These three equations are:

$$\frac{dE_1(z)}{dz} = \frac{-i\omega_1}{2}\sqrt{\frac{\mu}{\varepsilon_1}}\chi^{(2)}E_3(z)E_2^*(z)e^{i\Delta kz} \qquad (2.7)(a)$$

$$\frac{dE_2(z)}{dz} = \frac{-i\omega_2}{2}\sqrt{\frac{\mu}{\varepsilon_{21}}}\chi^{(2)}E_3(z)E_1^*(z)e^{i\Delta kz} \qquad (b)$$

$$\frac{dE_3(z)}{dz} = \frac{-i\omega_3}{2}\sqrt{\frac{\mu}{\varepsilon_{31}}}\chi^{(2)}E_2(z)E_1^*(z)e^{i\Delta kz}. \qquad (c)$$

In each case $\chi^{(2)}$ describes the interaction of the other waves in generating the resulting wave.

These are the coupled wave equations, and are so named because the amplitudes of the fields are coupled via the second-order tensor $\chi^{(2)}$. In a three-wave interaction, they describe both the propagation of the waves through the nonlinear medium and the interaction of the waves with one another.

The wave vector mismatch, denoted by Δk in Equations (2.7)(a), (b) and (c) is found from

$$\Delta k = k_3 - k_2 - k_1$$

where the individual wave vectors can be found from

$$k_i = \frac{n_i\omega_i}{c} = \frac{2\pi n_i}{\lambda_i}.$$

n_i is the refractive index, and λ_i is the wavelength of wave i and c is the speed of light.

It was previously mentioned that any combination of ω_1, ω_2, and ω_3 can interact during propagation through the nonlinear material, however, only the processes that experience gain and thus generate light in significant quantities will actually occur. Light is generated when the waves have the correct phase relationship to interfere constructively. This condition is called phasematching and is met when Δk=0.

The coupled wave equations can be solved to produce an equation that describes the gain, $G(\omega_s,\omega_i)$ of the signal and idler waves in an optical parametric oscillator:

$$G(\omega_s,\omega_i) \cong \frac{\omega_s \omega_i \mu_o (\chi^{(2)}_{eff})^2 L^2}{2 n_p n_s n_i c} I_o(\omega_p) \frac{\sin^2\left(\frac{\Delta kL}{2}\right)}{\left(\frac{\Delta kL}{2}\right)^2}. \qquad (2.8)$$

$\chi^{(2)}_{eff}$ is the effective second-order nonlinear susceptibility for the particular circumstances of the interaction and L is the interaction length. The gain of the optical parametric oscillator has a sinc^2 dependence on ΔkL. Thus it is clear that maximum gain is available from the optical parametric oscillator when Δk=0 and phasematching is achieved.

This second-order interaction can occur in a single-pass arrangement, where the incoming wave from a laser beam, passes once through the nonlinear medium in order to generate the resulting waves. This describes an optical parametric generator. The optical parametric generator can be modified by enclosing the nonlinear medium within suitably reflecting mirrors, so that one or more of the generated waves is allowed to oscillate, and significantly more light is produced. This describes an optical parametric oscillator.

Crystals that are suitable for use in optical parametric oscillation are described in the next section.

Nonlinear Crystals

For a crystal to be suitable for optical parametric oscillation, or for another second-order process, then the material must be structured so that it has a non-zero second-order nonlinear susceptibility, $\chi^{(2)}$. All crystalline materials fall into one of 32 possible structural categories, known as point groups. The different structures possess different degrees of symmetry, responsible for a number of different physical properties of the material. These properties render the material either piezoelectric, pyroelectric or ferroelectric. The lowest level of symmetry divides the crystals into two groups, those that are centrosymmetric and those that are not. The condition necessary for the material to have a non-zero second-order nonlinear susceptibility is that the crystal is non-centrosymmetric. Of the 32 crystal structures, 21 are non-centrosymmetric and are suitable for optical parametric oscillation[6].

As mentioned previously, $\chi^{(2)}$, is a third-rank tensor with 27 components, χ_{ijk}. However, the nonlinearity of a material is more usually discussed in terms of a piezoelectric tensor with its elements defined by

$$d_{ijk} = \frac{\chi_{ijk}}{2}.$$

In some cases j and k are not distinct and $d_{ijk}=d_{ikj}$. The tensor is equivalent to a 3×6 matrix, d_{ij}, with elements d_{11} to d_{36}. In most experimental work in nonlinear optics it is

assumed that there are no losses in the system, and that Kleinmann's symmetry conditions hold so that distinct coefficients of the matrix related by rearrangement of the subscripts are in fact equal. In this way the 3×6 matrix is further limited to only ten independent elements. In many cases only a few of these values are non-zero and these are called the nonlinear coefficients of the material. The resulting matrix has the same form for all members of a particular crystal class, and relates the polarisation and electric fields such that

$$\begin{bmatrix} P_x \\ P_y \\ P_z \end{bmatrix} = \begin{bmatrix} d_{11} & d_{12} & d_{13} & d_{14} & d_{15} & d_{16} \\ d_{16} & d_{22} & d_{23} & d_{24} & d_{14} & d_{12} \\ d_{15} & d_{24} & d_{33} & d_{23} & d_{13} & d_{14} \end{bmatrix} \begin{bmatrix} E_x^2 \\ E_y^2 \\ E_z^2 \\ 2E_zE_y \\ 2E_zE_x \\ 2E_xE_y \end{bmatrix}.$$

The d_{ij} coefficients can be used to calculate an effective nonlinearity for the material, d_{eff}, using equations that depend on crystal class. Equation (2.8) indicates that a large value for the effective nonlinear susceptibility, $\chi^{(2)}_{eff}$, will maximise the gain of an interaction, therefore it is desirable to use a material with a large value of d_{eff}. The particular matrices for the different crystal classes can be found in a number of texts[7-10].

Phasematching

As mentioned previously, the gain of a second-order nonlinear interaction is maximised when phasematching of the interacting waves is achieved and Δk=0. For an optical parametric oscillator,

$$\Delta k = k_p - k_s - k_i,$$

which can be expanded so that the phasematching condition becomes:

$$\frac{n_p}{\lambda_p} - \frac{n_s}{\lambda_s} - \frac{n_i}{\lambda_i} = 0 . \tag{2.9}$$

This equation effectively expresses the phasematching condition in terms of the conservation of photon momentum. Conservation of energy also states, that including $\omega=2\pi\nu$ and $c=\nu\lambda$ in Equation (2.9), that for an optical parametric oscillator:

$$\frac{1}{\lambda_p} - \frac{1}{\lambda_s} - \frac{1}{\lambda_i} = 0 . \tag{2.10}$$

Equations (2.9) and (2.10) must be simultaneously satisfied for light amplification to occur in a three-wave mixing process. Phasematching can be achieved either collinearly or noncollinearly, where the wavevectors are arranged as shown in Figure 1.

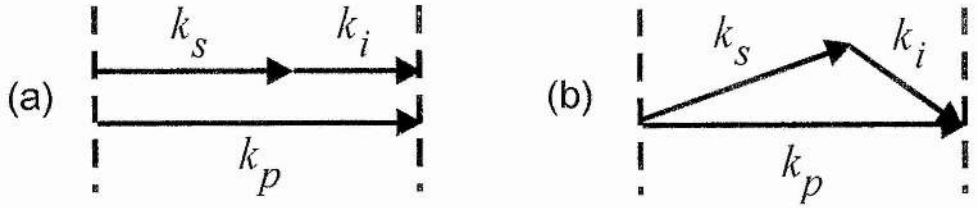

Figure 1: Arrangement of wavevectors for (a) collinear phasematching and (b) noncollinear phasematching.

The different techniques used to achieve phasematching in optical parametric oscillation are discussed in the following sections.

Birefringent Phasematching

A popular method for achieving phasematching involves using a nonlinear material that is birefringent[11]. When light consisting of orthogonal polarisations propagates in an arbitrary direction through a birefringent material, each polarisation experiences a different value of refractive index. Refractive index also varies with wavelength so Equation (2.9) does have solutions. Generally a birefringent crystal has three optical axes, defined relative to the crystallographic axis, and designated x, y and z. The refractive index associated with each axis has a value of n_x, n_y or n_z. A light wave propagating with its polarisation parallel to one of those axes will experience the refractive index of that axis, and is referred to as an ordinary wave, or o-wave. The light wave propagating with the orthogonal polarisation, at an angle to an axis, will experience a value of refractive index dependent on that angle, and is called an extraordinary wave, or e-wave. This situation is illustrated in Figure 2.

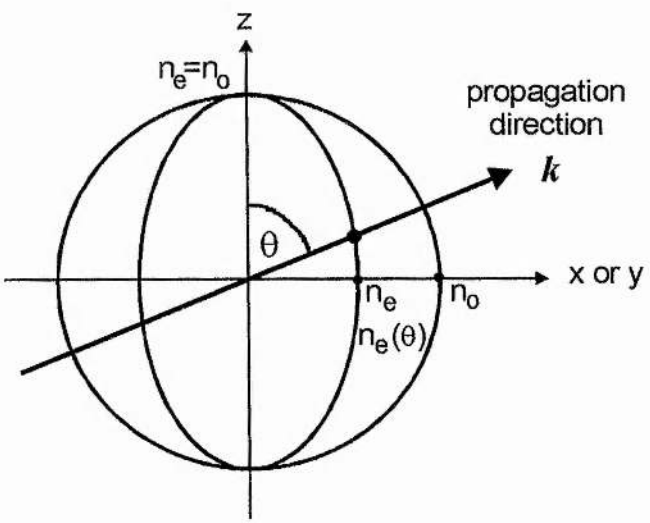

Figure 2: The values of refractive index seen by an o-wave and an e-wave on propagation through a birefringent crystal at an angle θ. In this case the crystal is negative uniaxial.

In this way the phasematching condition can be satisfied for a suitable choice of polarisations and propagation angles for the incident light.

There are two categories of birefringent crystal, those that are uniaxial and those that are biaxial. In a uniaxial crystal, two of the values of refractive index are equal, so that the propagating wave polarisations see either n_o or n_e. A uniaxial crystal may be positive, with $n_e > n_o$, or negative, with $n_e < n_o$. In a biaxial crystal n_x, n_y, and n_z have distinct values and either $n_x > n_y > n_z$, or $n_x < n_y < n_z$. Different combinations of ordinary and extraordinary waves can be used to achieve phasematching depending on whether the phasematching is Type I or Type II. For optical parametric oscillation in both positive and negative uniaxial crystals the type of phasematching involves the combinations of wave polarisations shown in Table 1.

	Positive	**Negative**
Type I	o→e+e	e→o+o
Type II	o→e+o	e→o+e
or	o→o+e	e→e+o

Table 1: Combination of wave polarisations used depending on the type of birefringent phasematching employed.

The variation of refractive index with wavelength is described by the experimentally derived Sellmeier equation for the particular crystal. Sellmeier equations for the crystals used in this work can be found in Chapters 4 and 5. The Sellmeier equation for a chosen

crystal can be included in the phasematching condition of Equation (2.9). Further, the angular variation of the refractive index can also be included, so that the propagation angle of the incident light required to generate specific signal and idler wavelengths from a given pump wavelength, can be determined.

For the configuration shown in Figure 2, the angular variation of n_e is given by

$$n_e(\theta) = n_o \sqrt{\left(\frac{1+\tan^2(\theta)}{1+\left(\frac{n_o}{n_e}\right)^2 \tan^2(\theta)} \right)}.$$

This angular variation of the refractive index means that it is possible to angle tune the output of the optical parametric oscillator by slowly rotating the crystal so that the pump beam experiences a slowly varying refractive index. The signal and idler wavelengths are tuned accordingly so that the phasematching condition still holds. The output from the optical parametric oscillator can be tuned using other methods such as pump tuning, where only the pump wavelength varies; all other parameters remain constant. Temperature tuning is also possible because in some birefringent crystals the refractive index varies significantly with temperature.

Birefringent phasematching can be achieved for two geometries of optical parametric oscillator cavity where the phasematching is either noncritical or critical. For noncritical phasematching, the pump, signal and idler waves all propagate along the crystal axis, and consequently see the refractive index of one of the other axes. In this case all waves remain collinear over the length of the crystal and therefore interact over the entire length

of the crystal. In this type of interaction the gain is high (because of the dependence of the gain on the square of the interaction length) and the output can be tuned by tuning the pump wavelength or varying the temperature of the crystal. Angle tuning is not possible for this geometry and thus the tuning range of the optical parametric oscillator can be limited. To obtain a particular wavelength from the OPO it is sometimes necessary to propagate the incident light at an angle to a crystal axis. This geometry is called critical phasematching. In critical phasematching the ordinary wave that propagates through the crystal can be described by a momentum vector, k and a Poynting vector, S. k and S are parallel and are normal to the wavefronts. This is illustrated in Figure 3. The extraordinary wave, on the other hand, has a Poynting vector that moves in a different direction to the momentum vector, at an angle $\rho(\theta)$, and this is called the walk-off angle. The wavefronts in this case remain normal to the momentum vector, k. The ordinary and extraordinary waves interact with each other over a short distance only, and the interaction is far less than in the case of noncritical phasematching. Hence, these systems are both low gain and of poor efficiency.

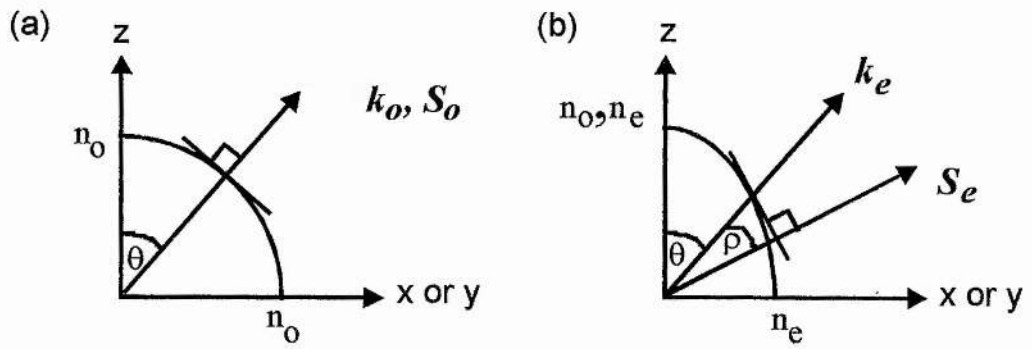

Figure 3: Direction of propagation of momentum vetor k and Poynting vector S for (a) an o-wave and (b) an e-wave.

Poynting vector walk-off is only a problem in a critically phasematched optical parametric oscillator. In a noncritically phasematched optical parametric oscillator all the waves propagate along an optical axis and thus there is no Poynting vector walk-off.

The problem of walk-off can be overcome by using a system called noncollinear phasematching. This time the ordinary and extraordinary waves are propagated with their momentum vectors at an angle to each other such that the extraordinary Poynting vector walks *onto* the ordinary Poynting vector, thus increasing the depth of the interaction. The walk-off angle for an extraordinary wave can be calculated from the dot product of the electric field unit vector, E, which is normal to the Poynting vector, S, and the displacement vector, D, which is normal to the momentum vector, k

$$\rho(\theta) = \pm \tan^{-1}\left[\left(\frac{n_o}{n_e}\right)^2 \tan\theta\right] \pm \theta .$$

Temporal Walk-away

The effects of Poynting vector walk-off can also be considered in terms of time. As can be seen from Equation (2.13), the group velocity of the pulse depends on frequency. As a result, the pump, signal and idler pulses propagate through the OPO crystal with different group velocities. After some distance through the material the pulses are no longer overlapped in time and there is no further interaction between them. This is the effect of walk-away. The amount that the pulses separate by, or the walk-away, w, can be

calculated as the difference in the inverse group velocities, of the pulses of different wavelengths

$$w = \frac{1}{v_{g1}} - \frac{1}{v_{g2}}. \tag{2.11}$$

This is an important factor when choosing a suitable OPO crystal. Typical values of walk-away, for frequently used OPO crystals are of around 100 fs/mm. In femtosecond OPOs, crystals need only be a few millimeters in length. In longer crystals, pulses suffer walk-away, and the extra gain available for the remaining crystal length is not exploited. Also the extra crystal length contributes to the intracavity group velocity dispersion and subsequently pulse broadening occurs. This is detrimental to the OPO process.

The optical parametric oscillators used in this work were phasematched using an alternative technique, which has been around longer than birefringent phasematching, but which has only recently become popular. This technique is called quasi-phasematching, and is discussed in the following section.

Quasi-Phasematching

Quasi-phasematching was originally developed by Armstrong et al [12], in 1962, and at that time it was not called quasi-phasematching. Quasi-phasematching is not like birefringent phasematching, in that it does not exploit the refractive indices of the material. In quasi-phasematching, the phasematching equation for Δk=0 includes an extra term, which depends upon a different physical property of the material. This property is the grating period of the crystal and crystals can be manufactured to have a specific

grating period for a specific operating wavelength. Nonlinear materials can be tailored in this way, so that a wider range of wavelengths can be generated, leaving the materials of use in a greater range of applications. At mid-infrared wavelengths, particularly beyond 4 μm, birefringent phasematching is limited because there are very few materials that are both transparent and which can be phasematched in this wavelength region.

When the pump, signal and idler waves propagate collinearly and the interaction is not phasematched, there is still an interaction between them as they propagate thorough the crystal. The waves convert to longer wavelengths and are then converted back, until such time that the phase relation favours forward conversion once again, and the process repeats itself. The overall conversion to new wavelengths, over the length of the crystal is negligible, and no useful output light is generated. This is shown in Figure 4. The propagation distance after which the gain is reduced by half, is the coherence length, l_c, and is given by

$$l_c = \frac{\pi}{k_p - k_s - k_i} = \frac{\pi}{\Delta k}.$$

In the process of quasi-phasematching, the sign of the nonlinear coefficient is reversed after each coherence length (so is modulated at twice the coherence length), and the interaction is brought back into phase, and continues to build up over the entire crystal length. When this occurs significant amounts of light can be generated. The gain is maximised when Δk=0, but the optical parametric oscillator will still oscillate for values of Δk close to zero.

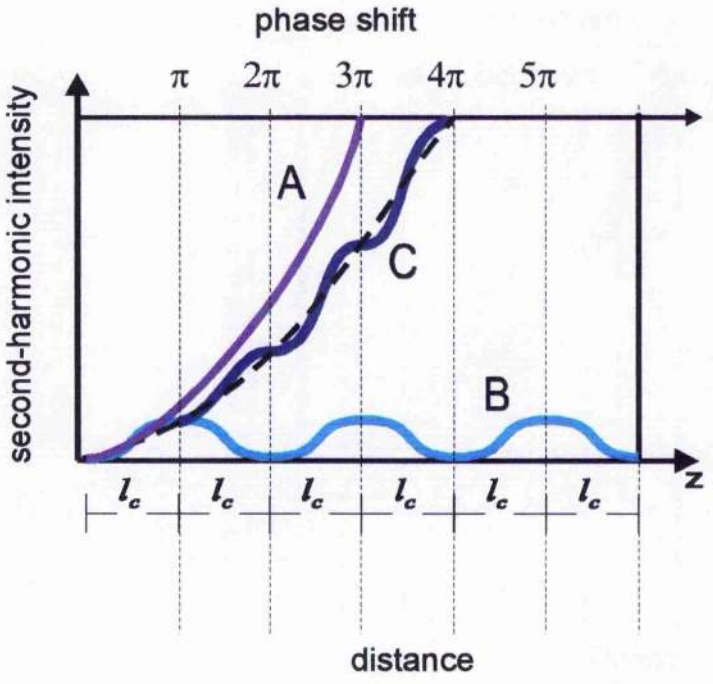

Figure 4: Growth of the second-harmonic light intensity with distance through a nonlinear crystal: A is for exact phasematching, B is for an interaction that is not phasematched, C is for first-order quasi-phasematching in a periodically-poled crystal.

Reversing the sign of the nonlinearity is achieved via a technique called periodic-poling. This involves applying an electric field to a ferroelectric crystal to periodically reverse the polarity and therefore the nonlinearity. The technique of periodic-poling is discussed further at the end of this chapter. It is only now that reliable fabrication methods for poling crystals are available, and so the use of quasi-phasematching has only recently become so popular.

The period of modulation of the nonlinearity is called the grating period, Λ, and is such that:

$$\Lambda = 2nl_c,$$

where l_c is the coherence length of the material. It is this value of the grating period that is the extra term included in the phasematching equation. For quasi-phasematching:

$$\Delta k_q = k_p - k_s - k_i - k_g,$$

where k_g is the grating vector, found from:

$$k_g = \frac{2\pi m}{\Lambda}$$

and m is the order of the quasi-phasematched process. m=1,3,5...; m=1 is a first order process. Thus an appropriate grating period can be chosen to allow phasematching to be possible. Quasi-phasematching calculations can be carried out in the same way as for birefringent phasematching, provided that the grating vector is included in the equations. The conservation of momentum condition for first order quasi-phasematching in an optical parametric oscillator is:

$$\frac{n_p}{\lambda_p} - \frac{n_s}{\lambda_s} - \frac{n_i}{\lambda_i} - \frac{1}{\Lambda} = 0 \qquad (2.12)$$

and the conservation of energy condition of Equation (2.10) remains unchanged. There are a number of advantages of quasi-phasematching over birefringent phasematching. The use of a grating means that a nonlinear crystal can be manufactured to phasematch any desired combination of wavelengths within the transparency range of the material, thus overcoming the limitations of birefringent phasematching. Also, the lack of dependence on the birefringent properties of the crystal means that any combination of propagation direction and light polarisations can be used. The light waves can always be propagated along a crystal axis and the problems caused by Poynting vector walk-off can be eliminated. In birefringent phasematching the restriction on light polarisation

combinations means that frequently the highest nonlinearities of the material cannot be accessed. In quasi-phasematching, polarisations are chosen to access the largest nonlinearities and this in turn increases the gain of the system. The effective nonlinearity of a quasi-phasematched process is given by:

$$d_{eff(q)} = \frac{2\pi}{m} d_{eff},$$

where d_{eff} is the effective nonlinear coefficient for the equivalent process in the absence of a grating. A first order process is most efficient.

This section has described the three principal methods of phasematching: noncritical and critical birefringent phasematching and quasi-phasematching. Each of the optical parametric oscillators used in this work was quasi-phasematched and this will be discussed further in the experimental chapters. The current popularity of quasi-phasematching has increased dramatically because of the advantages it has over birefringent phasematching and also because it is now possible to manufacture high quality periodically-poled crystals. There are a number of techniques for periodically-poling nonlinear optical crystals and these will be described in the next section.

Periodic-Poling

There are a variety of fabrication methods for periodically-poling crystals, all of which are aimed at producing high quality, uniform grating structures, to micrometre precision, and without disturbing the linear and nonlinear optical properties of the material. These techniques have succeeded to varying degrees. Shallow gratings suitable for waveguides

can be produced using chemical indiffusion[13,14], but these gratings are not deep enough to be used in bulk materials. Techniques based on modulating the crystal growth process[15,16] have produced crystals which suffer from poor conversion efficiency resulting from axial variations that are introduced in the domain periodicity. Bulk PPLN with good periodicity can be produced using electron beam writing[17], but the reproducibility is not sufficiently good to justify commercial manufacturing. Houé and Townsend[18] review a number of other interesting techniques for fabricating gratings, including electric field poling, which is relevant to this work and has proved to be more reliable than the aforementioned methods.

In electric field poling, the crystal is prepared by depositing a mask, which defines the structure of the grating, onto its surface. An electric field is then applied along the material to reverse the polarity, and this acts only on the sections of the crystal which are not protected by the mask. The mask consists of a layer of insulator in the form of a photoresist, and a layer of conductor, which is often aluminium. These layers can be applied in either order to form the mask and the configuration in each case is shown in Figure 5.

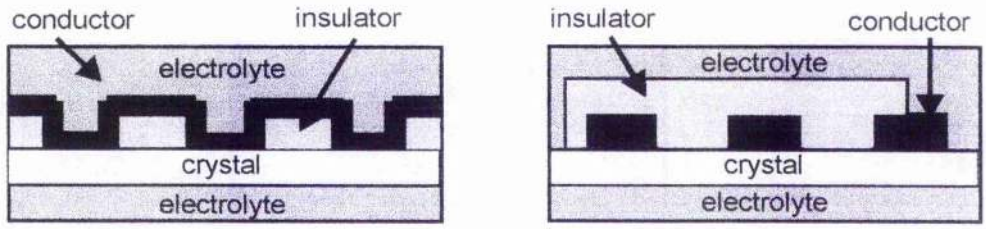

Figure 5: Arrangement of electrodes for electric field poling. In both cases the electrolyte layer connects the crystal to a circuit that applies the electric field.

In the first arrangement, the photoresist is applied first, to protect the areas of the crystal that are not to have their polarity reversed. The conducting layer is applied on top. The electric field is applied to the metal via a contact with a layer of liquid electrolyte. In the second arrangement the aluminium layer is applied first, to the regions which have to have their polarity reversed. The photoresist layer is applied on top, except for a small area of metal, which is left as a contact for applying the electric field.

The electric field can be applied continuously or as a series of short pulses. Permanent application of a high electric field can cause the permanent breakdown of the crystal lattice, and in cases where this is likely a pulsed electric field is used. The electric field has to be greater than the coercive field of the material for polarity reversal to occur and the amount of charge required to pole the crystal is given by

$$Q = 2P_s A$$

where P_s is the spontaneous polarisation and A is the area of the crystal.

The poling process lasts for sufficient time that the domain reversal can leak sideways into neighboring domains in the crystal. For this reason a 50:50 duty cycle mask does not produce a precise 50:50 grating, and the duty cycle of the mask has to be adjusted to compensate for this. After poling the crystals are annealed at a low temperature to reduce the strain imposed during the poling process.

The resulting periodically-poled crystal consists of a series of nonlinear segments with opposing optical domains and this is shown in Figure 5. Changing the sense of the

polarisation causes a change of phase of π to a light wave passing through the crystal. For every odd multiple of the crystal coherence length l_c, such a reversal occurs and a phase shift of π is added to an existing one. The result is that only constructive interference can occur.

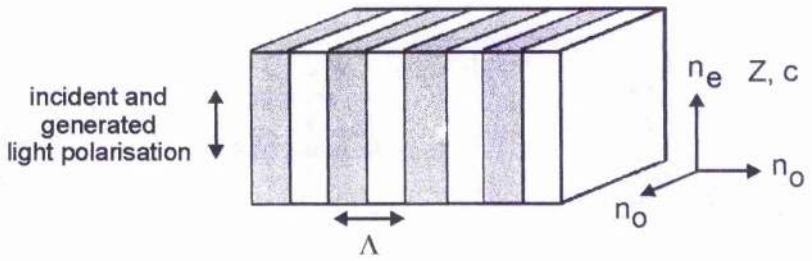

Figure 5: Diagram of a periodically-poled crystal showing the optical domains, the orientation of the crystal axes and the orientation of the incident light polarisation required to exploit the nonlinear optical properties of the material.

Periodic domain inversion eliminates the need for index matching and can allow the largest nonlinear coefficients of the material to be accessed.

Within the laser cavity the physical length of the gain medium causes a large amount of group velocity dispersion (GVD). Combined with the high intracavity powers present in a modelocked Ti:sapphire laser system or an ultrashort pulse OPO the physical length of the gain medium will also produce considerable self-phase modulation (SPM). It is the combined effect of GVD and SPM that determines the duration and shape of ultrashort light pulses. To generate transform-limited ultrashort light pulses these effects have to be carefully controlled and this subject is considered next.

Group Velocity Dispersion

In a linear optical material the refractive index varies with the wavelength of the light which passes through it. This wavelength dependence, or dispersion, can be calculated for any optical material using the Sellmeier equation

$$n^2(\lambda) = 1 + \frac{B_1\lambda^2}{\lambda^2 - C_1} + \frac{B_2\lambda^2}{\lambda^2 - C_2} + \frac{B_3\lambda^2}{\lambda^2 - C_3}$$

where $B_{1,2,3}$ and $C_{1,2,3}$ are experimentally derived Sellmeier constants and have different values for different materials. The velocity of light travelling through a material is different for different light wavelengths, and this causes dispersion. When $n(\lambda)$ and $\frac{dn(\lambda)}{d\lambda}$ decrease with wavelength, the material is normally dispersive. In such a material blue light travels slower and therefore refracts more strongly than red light. For a short intense light pulse passing through a normally dispersive material, the leading edge of the pulse is 'red shifted'. That is, the longer wavelength components speed up in the material and extend the leading edge of the pulse. The trailing edge of the pulse is 'blue shifted' i.e. the shorter wavelength components are slowed down thus retarding the trailing edge of the pulse. Pulse broadening occurs and the pulse is said to be frequency chirped.

If the linear optical material has a frequency propagation constant β, and the propagating wave has a centre frequency ω_o, a Taylor series expansion of $\beta(\omega_o)$ gives:

$$\beta(\omega) = n(\omega)\frac{\omega}{c} = \beta_o(\omega_o) + \beta_1(\omega - \omega_o) + \frac{1}{2}\beta_2(\omega - \omega_o)^2 + \frac{1}{3!}\beta_3(\omega - \omega_o)^3 + \ldots \quad .$$

For a light pulse, the pulse envelope travels at a group velocity v_g, where:

$$\beta_1 = \frac{d\beta}{d\omega} = \frac{1}{c}\left[n + \omega\frac{dn}{d\omega}\right] = \frac{1}{v_g}. \tag{2.13}$$

The GVD[19,20], which describes the frequency chirp introduced by the dispersive material, is given by:

$$\beta_2 = \frac{d^2\beta}{d\omega^2} = \frac{1}{c}\left[2\frac{dn}{d\omega} + \omega\frac{d^2n}{d\omega^2}\right] = \frac{\lambda^3}{2\pi c^2}\frac{d^2n}{d\lambda^2}.$$

If β_2 equals zero then the temporal pulse envelope is unchanged as the pulse propagates indefinitely. (There is a 'zero dispersion wavelength' of 1.3μm and this is the wavelength at which $\beta_2 = 0$ for many optical materials.) In ultrashort light pulse generation third-order dispersion can also be significant and:

$$\beta_3 = \frac{d^3\beta}{d\omega^3} = \frac{1}{c}\left[3\frac{d^2n}{d\omega^2} + \omega\frac{d^3n}{d\omega^3}\right].$$

Introducing a series of prisms into the cavity can produce a negative GVD, which will compensate for the positive GVD produced in the cavity elements. For a single pass of four Brewster-angled prisms, arranged as shown in Figure 6.

$$\frac{d^2P}{d\lambda^2} = 4l\left\{\left[\frac{d^2n}{d\lambda^2} + \left(2n - \frac{1}{n^3}\right)\left(\frac{dn}{d\lambda}\right)^2\right]\sin\theta - 2\left(\frac{dn}{d\lambda}\right)^2\cos\theta\right\}$$

where P is the optical path length. Generally θ is the order of the angular deviation of the light wave, therefore $\cos\theta$ is approximately equal to one. $l\sin\theta$ is close to the beam spot size of about 2 mm. For a sufficiently large prism separation l the prism sequence will introduce a net negative GVD if $\frac{d^2n}{d\lambda^2}$ is not large compared to $\left(\frac{dn}{d\lambda}\right)^2$.

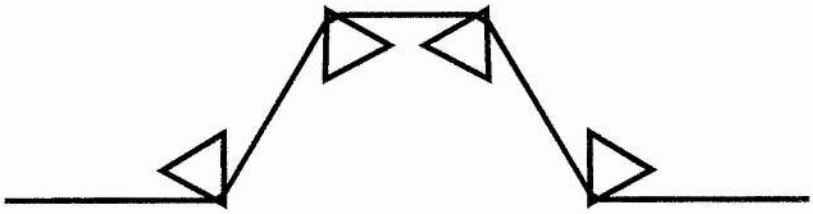

Figure 6: Prism sequence used to control group velocity dispersion.

A plane mirror can be placed in the symmetry plane of the four-mirror sequence to produce an equivalent system. This is the standard arrangement in a linear self-modelocked Ti:sapphire laser cavity for GVD compensation[21].

The use of a prism sequence to introduce negative GVD into the laser cavity will reduce the overall GVD seen by the laser pulse and therefore reduce the pulse duration. However, if both second and third-order intracavity dispersion compensation can be introduced into a laser or OPO cavity, then the pulse durations can be further reduced. It is possible to compensate perfectly for both second and third-order dispersion for pulses at a centre wavelength within a range defined by the laser crystal and prism materials and the apex angle of the prisms.

The effect of third-order dispersion, or cubic phase, has been considered by Brabec et al.[22]. Various techniques have been used to reduce the amount of third-order dispersion experienced by the laser pulse. These include the use of shorter laser crystals[23,24], non-standard prism materials[25-27] and the use of an intracavity Gires-Tournois interferometer[28]. Each of these techniques has succeeded to some degree. More recently, Lemoff and Barty[29] have shown that it is possible to simultaneously eliminate

intracavity cubic phase and still compensate for the intracavity GVD experienced by an ultrashort laser pulse.

This is accomplished using a correct choice of prism material, prism separation and of the amount of prism glass inserted into the laser cavity. For a single pass of four Brewster-angled prisms, arranged as shown in Figure 6,

$$\frac{d^3P}{d\lambda^3} = l\cos\beta\left[\left(\frac{24}{n^3}-48n\right)\left(\frac{dn}{d\lambda}\right)^3 - 24\frac{dn}{d\lambda}\frac{d^2n}{d\lambda^2}\right]$$
$$+ l\sin\beta\left[\left(\frac{dn}{d\lambda}\right)^3\left(\frac{12}{n^6}+\frac{12}{n^4}+\frac{8}{n^3}-\frac{16}{n^2}+32n\right)+\left(24n-\frac{12}{n^3}\right)\frac{dn}{d\lambda}\frac{d^2n}{d\lambda^2}+4\frac{d^3n}{d\lambda^3}\right]$$

This opens up the possibility of producing shorter pulses from laser and OPO systems than have previously been reported, and with durations that are ultimately limited by fourth-order dispersion and the gain bandwidth of the laser or OPO crystal material.

An alternative method for third-order dispersion compensation is to use cavity mirrors which have chirped dielectric coatings, otherwise known as chirped mirrors[30]. These mirrors have been used in Ti:sapphire laser systems to generate pulse of less than 5 fs duration[31]. The mirror-dispersion-compensated Ti:sapphire laser described in the next chapter, relies on this technique for generating pulses of less than 20 fs duration. Chirped mirrors have also been used in OPO systems based on potassium titanyl arsenate ($KTiOAsO_4$) and this has resulted in the successful generation of pulses of 50 fs duration at 1.25 μm[32,33].

Self-Phase Modulation

In nonlinear optical materials the presence of a nonlinear refractive index causes the material refractive index to be dependent on intensity, and this is described by

$$n = n_o + n_2 I(t)$$

where $I(t)$ is the temporal intensity of the pulse and n_2 is the nonlinear refractive index of the material. The $n_2 I(t)$ term is a result of the optical Kerr effect and causes the pulse to suffer a time-dependent phase delay $\Delta\phi(t)$, which also depends on the intensity of the pulse.

$$\Delta\phi(t) = kL\Delta n(t) = \frac{2\pi L}{\lambda} n_2 I(t)$$

where L is the length of the material. Thus the nonlinear refractive index is responsible for SPM of the pulse[34,35].

For a short intense light pulse, this phase delay causes a nonlinear instantaneous frequency chirp described by

$$\Delta\omega = \frac{d}{dt}(\Delta\phi(t)) = \frac{2\pi L n_2}{\lambda}\frac{dI(t)}{dt}.$$

The dependence of $\Delta\omega$ on the temporal gradient of the pulse intensity combined with $n_2 > 0$ (which is usually the case), causes the leading edge of the pulse to experience a 'red shift' and the trailing edge of the pulse to experience a 'blue shift'. For a smooth pulse profile, the central region of the pulse will experience an approximately linear frequency chirp. The frequency shift produces additional spectral components, which in turn cause the spectral bandwidth to be broadened. The phase and frequency shift across

a pulse which has undergone SPM, and the corresponding pulse spectrum are shown in Figure 7. Additional peaks present in a typical self-phase modulated spectrum are a result of interference between equal spectral components, which exist at different times.

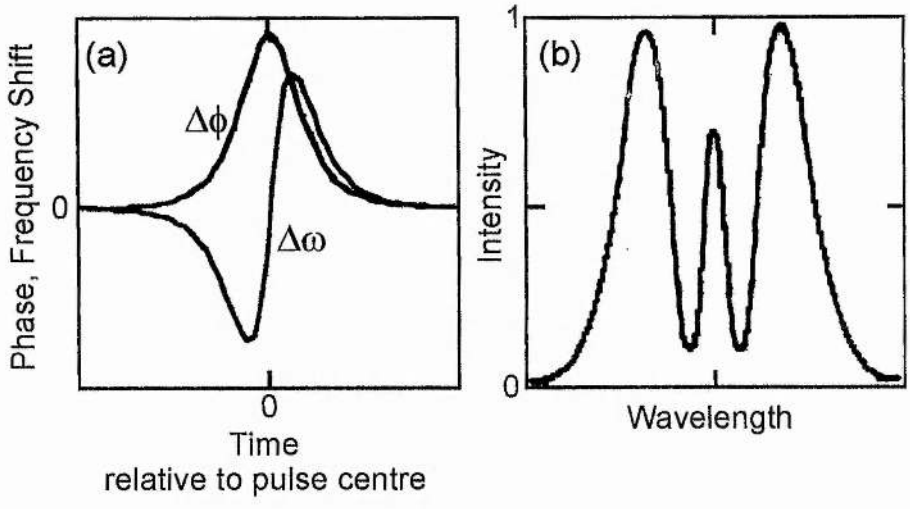

Figure 7: (a) The phase and frequency shift across a pulse that has undergone SPM (b) the corresponding pulse spectrum.

The linear frequency chirp is positive and is thus equivalent to the chirp produced when a light beam propagates through a positively dispersive material. This can also be seen from Figure 7. Thus the effect of SPM can also be compensated for using GVD compensation. In a dispersion-compensated OPO, the SPM produced by the nonlinear crystal can broaden the pulse spectrum sufficiently that shorter pulse durations can be generated than if SPM is not present. It can be seen from the time-bandwidth product of Equation 1.0 that this is clearly possible.

The intensity dependence of the refractive index or Kerr nonlinearity also causes another effect called self-focusing. When the laser beam is focused into the crystal, the maximum nonlinear phase delay is at its centre. The central part of the beam experiences a larger refractive index than the edges of the beam so the centre of the beam propagates more slowly than the edges of the beam. For a large enough light intensity (i.e. the peak of the pulse) the gain medium acts as a positive lens. The result of this effect can be seen in Figure 8.

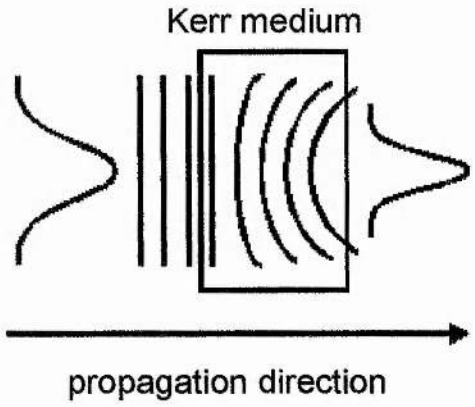

Figure 8: Self-focusing of an intense laser beam due to the optical Kerr effect.

Summary and Conclusions

This chapter has discussed nonlinear optics and the properties of nonlinear optical materials. Phasematching has been explained along with techniques for achieving this, including birefringent phasematching and quasi-phasematching. A review of techniques for periodically-poling nonlinear optical crystals is given. The chapter concludes with a section on the optical effects that influence the output from an ultrashort pulse laser or OPO and described methods for second and third-order dispersion compensation.

This chapter concludes the theory required to explain the experiments in the chapters to follow. The first of these experiments concerns the operation and characterisation of a femtosecond Ti:sapphire laser using the technique of frequency-resolved optical gating. This is followed by the operation and characterisation of a mirror-dispersion-compensated Ti:sapphire laser system providing transform-limited pulses of less than 20 fs duration. Consideration is given to the suitability of these lasers as pump sources for a femtosecond optical parametric oscillator.

The final three chapters describe the operation and characterisation of femtosecond optical parametric oscillators based on periodically-poled rubidium titanyl arsenate and periodically-poled lithium niobate.

Chapter 2

References

1. R.W Boyd, Nonlinear Optics (Academic Press, San Diego, 1992)
2. A Yariv, Quantum Electronics (third ed, Wiley New York, 1989)
3. A Yariv, Optical Electronics (fourth ed, Saunders College Publishing, USA, 1991)
4. R.L Byer, "Parametric oscillators and nonlinear materials", Ch2, *Nonlinear Optics: Proceedings of the Sixteenth Scottish Universities Summer School in Physics*, P.G Harper and B.S Wherrett, ed. (Academic Press, London, 1977)
5. R.W Munn, "Nonlinear optical phenomena", Ch2, and M Ebrahimzadeh and A.I Ferguson, "Novel nonlinear crystals", Ch6, *Principles and Applications of Nonlinear Optical Materials*, R.W Munn and C.N Ironside, ed. (Blackie Academic and Professional, 1993)
6. V.G Dmitriev, G.G Gurzadyan and D.N Nikogosyan, Handbook of Nonlinear Opticals (second ed, Springer-Verlag, Berlin, 1997)
7. R.W Boyd, Nonlinear Optics (Academic Press, San Diego, 1992) p44
8. A Yariv, Quantum Electronics (third ed, Wiley New York, 1989) p381
9. R.L Byer, "Parametric oscillators and nonlinear materials", Ch2, *Nonlinear Optics: Proceedings of the Sixteenth Scottish Universities Summer School in Physics*, P.G Harper and B.S Wherrett, ed. (Academic Press, London, 1977) p55
10. R.W Munn, "Nonlinear optical phenomena", Ch2, and M Ebrahimzadeh and A.I Ferguson, "Novel nonlinear crystals", Ch6, *Principles and Applications of Nonlinear Optical Materials*, R.W Munn and C.N Ironside, ed. (Blackie Academic and Professional, 1993) p115

11.V.G Dmitriev, G.G Gurzadyan and D.N Nikogosyan, Handbook of Nonlinear Opticals (second ed, Springer-Verlag, Berlin, 1997)

12.J.A Armstrong, N Bloembergen, J Ducuing and P.S Pershan, *Phys. Rev.* **127** 1918 (1962)

13.E.J Lim, M.M Fejer and R.L Byer, *Electron. Lett.* **25** 174 (1989)

14.M.L Bortz, M.A Arbore and M.M Fejer, *Opt. Lett.* **20** 49 (1995)

15.G.A Magel, M.M Fejer and R.L Byer, *Appl. Phys.* **56** 108 (1990)

16.Y Lu, L Mao and N Ming, *Opt. Lett.* **19** 1037 (1994)

17.H Ito, C Takyu and H Inaba, *Electron. Lett.* **27** 1221 (1991)

18.M Houé and P.D Townsend, *J. Phys. D* **28** 1747 (1995)

19.A.E Siegman, Lasers (University Science Books, California, 1986) Ch 9

20.G.P Agrawal, Nonlinear Fibre Optics (Academic Press, Inc., London 1989) Ch 3

21.R.L Fork, O.E Martinez and J.P Gordon, *Opt. Lett.* **9** 150 (1994)

22.T Brabec, C Spielmann and F Krausz, *Opt. Lett.* **17** 748 (1992)

23.C.P Huang, M.T Asaki, S Backus, H Nathel, M.M Murnane and H.C Kapteyn, *Opt. Lett.* **17** 1289 (1992)

24.F Krausz, C Spielmann, T Brabec, E Wintner and A.J Schmidt, *Opt. Lett.* **17** 279 (1992)

25.B.E Lemoff and C.P.J Barty, *Opt. Lett.* **17** 1367 (1992)

26.C.P Huang, M.T Asaki, S Backus, H Nathel, M.M Murnane and H.C Kapteyn, *Opt. Lett.* **17** 1289 (1992)

27.C.P Huang, H.C Kapteyn, J.W McIntosh and M.M Murnane, *Opt. Lett.* **17** 139 (1992)

28.J.M Jacobson, A.G Jacobson, K Naganuma, H.A Haus and J.G Fujimoto, *Digest of Conference on Lasers and Electro-Optics* (Optical Society of America, Washington D.C. 1992) paper CTuU2

29.B.E Lemoff and C.P.J Barty, *Opt. Lett.* **18** 57 (1993)

30.R Szipöcs, K Ferencz, C Spielmann and F Krausz, *Opt. Lett.* **19** 201 (1994)

31.M Nisoli, S de Silvestri, O Svelto, R Szipöcs, K Ferencz, Ch. Spielmann, S Sartania and F Krausz, *Opt. Lett.* **22** 522 (1997)

32.J Hebling, E.J Mayer, J Kuhl and R Szipöcs, *Opt. Lett.* **20** 919 (1995)

33.J Hebling. H Giessen, S Linden and J Kuhl, *Opt. Commun.* **141** 229 (1997)

34.A.E Siegman, Lasers (University Science Books, California, 1986) Ch 10

35.G.P Agrawal, Nonlinear Fibre Optics (Academic Press, Inc., London 1989) Ch 4

CHAPTER 3

Characterisation of Two Ti:sapphire Lasers Incorporating Different Methods of Dispersion Compensation

---

There are a number of areas of physics that rely on the generation of shorter, more intense and higher quality optical pulses to ensure their further exploration. The only available method for creating a coherent macroscopic polarisation is provided by optical excitation (and probing) on a timescale of 10 fs, and this is necessary for the investigation of important phenomena in semiconductors[1] as well as studying the dynamics of various chemical reactions and biological processes directly in the time domain. The intensity levels available in pulses of 10 fs duration exceed those previously attained and this opens up new possibilities for a range of experiments in nonlinear optical effects in particular[2,3].

In this chapter the operation of two different Ti:sapphire laser systems is described where the characterisation of the output pulses of each, using methods which have been described already in Chapter 1, is highlighted. The first is a prism-dispersion-compensated Ti:sapphire laser for which the results of SHG-FROG measurements and conventional interferometric autocorrelation and spectral methods, are made for varying amounts of net intracavity dispersion[4]. In the second experiment, the operation and characterisation of a mirror-dispersion-compensated Ti:sapphire laser, capable of producing sub- 20 fs duration pulses, is considered. The chapter concludes with some discussion of the suitability of each of these lasers as a pump source for an optical parametric oscillator.

Experimental Comparison of Conventional Pulse Characterisation Techniques and Second-Harmonic-Generation Frequency-Resolved Optical Gating

The technique of frequency-resolved optical gating (FROG)[5] is a powerful method for measuring the amplitude and phase of the electric field envelope of an ultrashort pulse. In one manifestation, second harmonic generation FROG (SHG-FROG)[6], the average field in a sequence of high-repetition-rate pulses from a moderate power laser oscillator can be measured. The application of SHG-FROG to the analysis of pulses from a self-modelocked Ti:sapphire laser, operating at a wavelength close to 800 nm and with varying amounts of net intracavity dispersion, is described here and the results of the SHG-FROG measurements are compared to those obtained using conventional interferometric autocorrelation and spectral measurement methods.

The Ti:sapphire Laser

The cavity configuration of the regeneratively-initiated self-modelocked Ti:sapphire laser used in this experiment is shown schematically in Figure 1. A Spectra-Physics Millennia laser (diode-pumped frequency-doubled Nd:YVO_4 laser) providing 5 W of power at 532 nm was used as the pump source for the Ti:sapphire laser. The vertically polarised output from the pump laser was rotated using a half-wave plate, which was antireflection coated for low loss at 532 nm, to allow it to enter the Ti:sapphire crystal as horizontally polarised light. The pump beam was focused into the Ti:sapphire crystal using a 100 mm focal length lens and this produced a beam waist radius of 34 μm.

The Ti:sapphire laser crystal had a length of 10 mm, with Brewster-angled faces and a pump absorption coefficient of 2.3 cm^{-1}. An electronically controlled Peltier-effect cooler was used to maintain the temperature of the Ti:sapphire crystal at 15°C. Low pressure water was also used to aid this cooling. The folding section consisted of spherical mirrors, each having a radius of curvature of -100 mm. These mirrors were highly reflecting at a wavelength of 800 nm and highly transmitting at the pump wavelength. A plane high reflector and a 15 % output coupler at 800 nm were also needed to form the cavity.

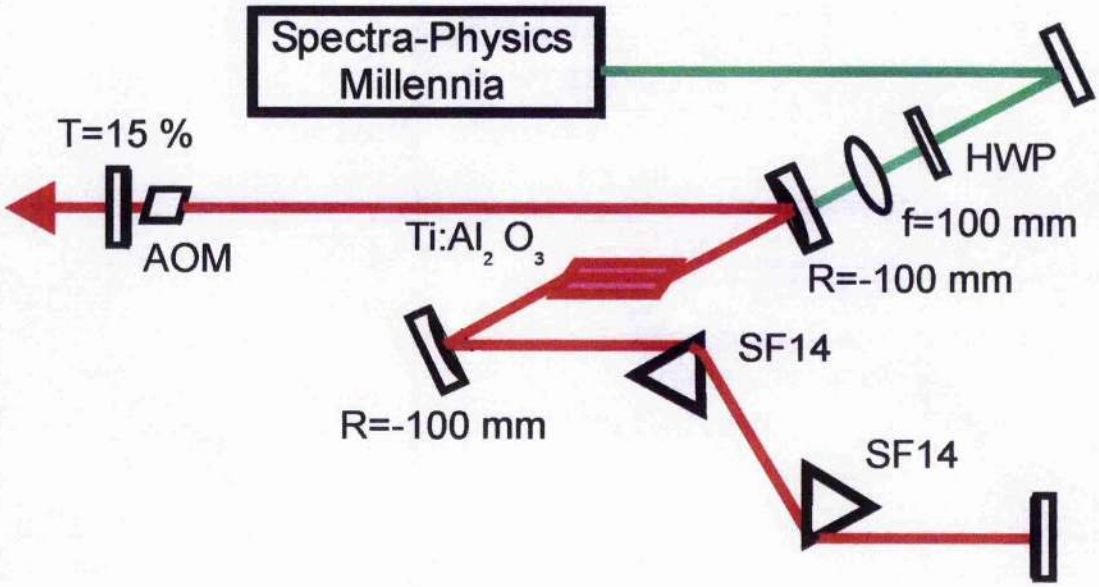

Figure 1: Cavity schematic of the self-modelocked Ti:sapphire laser studied in the FROG analysis. AOM - acousto-optic modulator; HWP - half-wave plate at 532 nm.

An acousto-optic modulator, consisting of a Brewster-angled quartz slab, was placed close to the output-coupling mirror and was used to initiate and stabilise the self-modelocked operation of the laser. Dispersion compensation was achieved by including two SF14 prisms in the cavity at a separation of 32 cm. Accurate

optimisation of the cavity alignment to obtain maximum cw output power caused the laser to self-modelock. In this case, pulses of less than 100 fs at 800 nm, at an output power close to 900 mW and with a repetition frequency of 76 MHz were produced. The net intracavity group velocity dispersion could be accurately adjusted by varying the amount of prism glass inserted into the intracavity beam.

The SHG-FROG System

The principle of SHG-FROG is to record the spectrum of the pulse SHG autocorrelation signal for a range of positive and negative delays. Our system was based on a Michelson interferometer type of delay line comprising, in one arm, a static corner-cube retroreflector and, in the other, a retroreflector mounted on an electromagnetic shaker. The outputs of the interferometer were adjusted for noncollinear second harmonic generation in a 500 μm thick crystal of BBO therefore allowing us to record the background-free intensity autocorrelation of the pulse. Our SHG-FROG system, illustrated schematically in Figure 2, was designed to allow continual video-rate acquisition of the FROG trace.

The background-free autocorrelation signal obtained from the interferometer was dispersed by an SF11 prism and then imaged to form a line spectrum on the surface of a CCD camera. The spectrum was swept across the surface of the camera by a spinning mirror, which was phase-locked to the shaker frequency of approximately 15 Hz. The camera image showed directly the SHG-FROG trace of the pulse sequence from the laser.

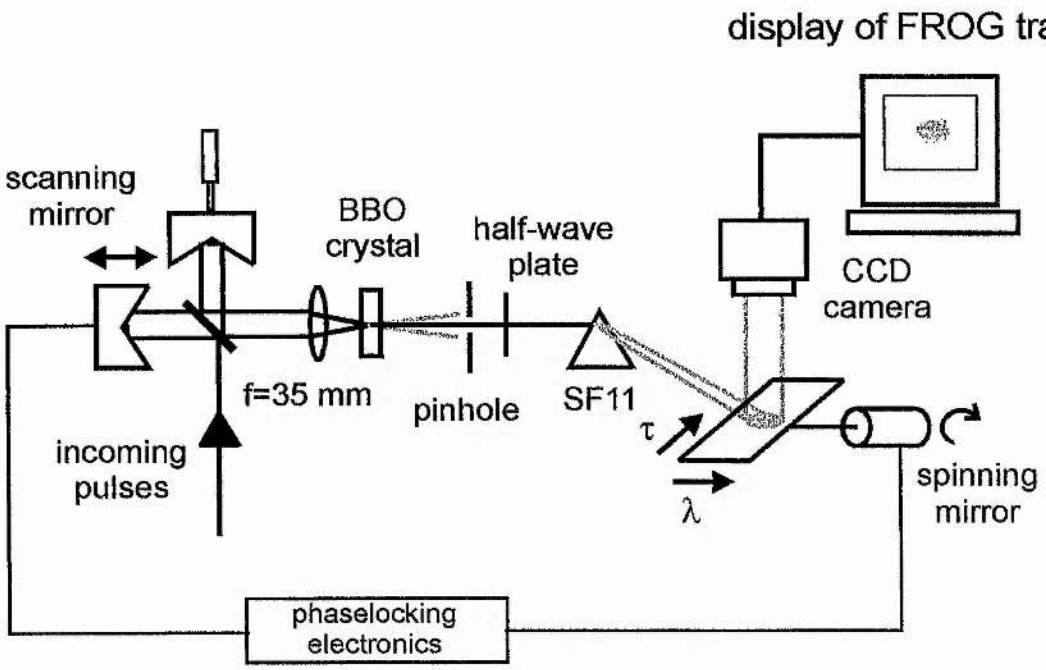

Figure 2: Schematic of real-time SHG-FROG system

A 90 MHz Pentium personal computer with a framestore interface was used to digitise the camera image, remove residual background noise and calibrate the trace in delay and wavelength. Using our proprietary Windows 95 software, which implemented both the basic and generalised projections FROG algorithms on a 128 × 128 dataset[7], we were able to retrieve the pulse shape and phase as a function of time and wavelength. Convergence of our algorithm typically required 100 iterations on a timescale of approximately 2 minutes.

The Experiment

The aim of the experiment was to directly compare the measurement techniques of SHG-FROG and interferometric autocorrelation and to assess the effect of intracavity laser dispersion on the output pulse shape and frequency-chirp. By varying the

amount of intracavity prism glass we operated the Ti:sapphire laser throughout a range of intracavity dispersions, which we estimate from Sellmeier data for SF14 glass, to correspond to -1110 to +170 fs^2. After initial calibration of the FROG system in delay and wavelength using an intensity autocorrelation of the laser output pulses and a spectrum of the laser second harmonic we made a series of measurements throughout the dispersion range described above. In order to be able to confirm the integrity of the FROG analysis we recorded, in addition to the SHG-FROG trace, the pulse spectrum and interferometric autocorrelation profile. Figure 3 shows the complete set of experimental measurements.

The first column depicts the calibrated FROG data used for the retrieval and uses a delay interval of 8 fs and a wavelength interval of approximately 0.5 nm. The second column shows the experimentally measured interferometric autocorrelation and the blue line overlaid on these plots represents the autocorrelation profile calculated from the pulse-shape retrieved by the FROG algorithm. In the third and fourth columns we plot the temporal and spectral intensity (circles) and phase (squares) retrieved from the FROG analysis. The pulse spectrum measured independently of the FROG system is shown overlaid in pink on the FROG results. The general agreement is good and shows that the integrity of the FROG calibration and retrieval is high.

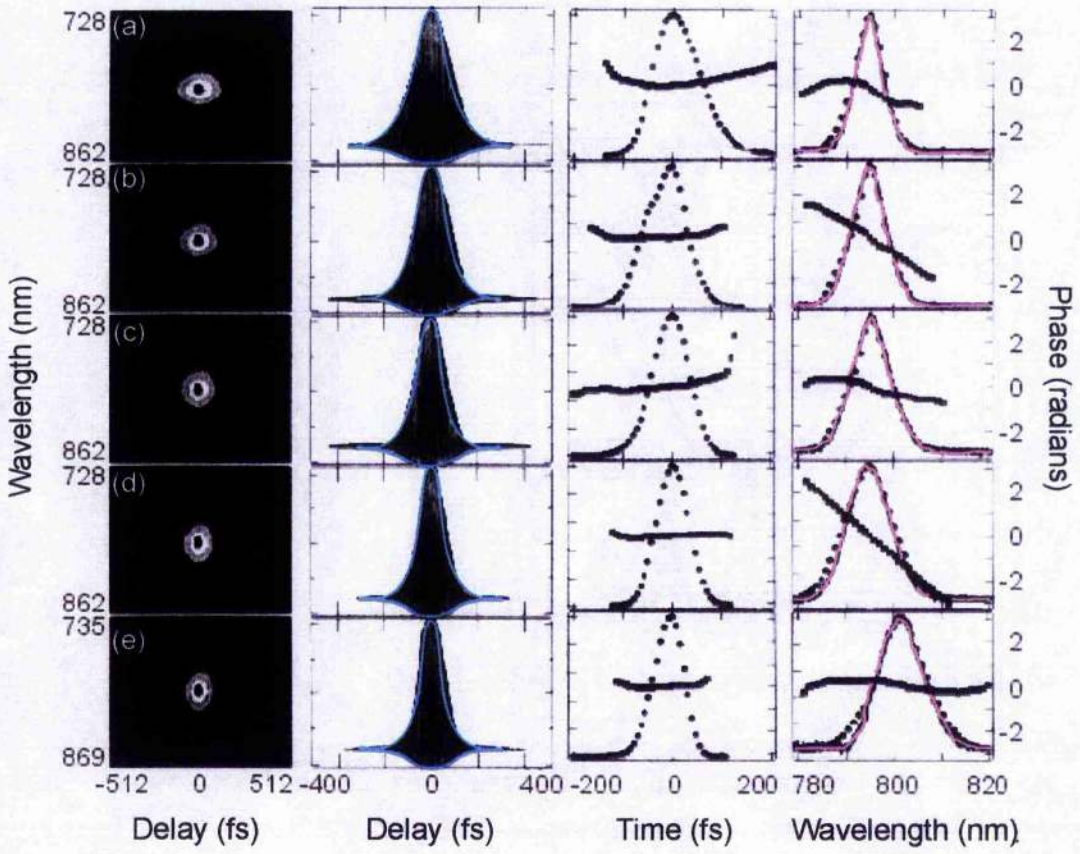

Figure 3: Measured SHG-FROG traces (column 1); experimental and calculated (blue line) interferometric autocorrelation profiles (column 2); pulse temporal intensity (circles) and phase (squares) determined by FROG (column 3); experimental spectrum (solid pink line) and pulse spectral intensity (circles) and phase (squares) determined by FROG (column 4).

The FROG retrieval-error, G, for each measurement is listed in Table 1, along with the estimated absolute roundtrip cavity dispersion and the temporal linear chirp parameter, b, for a pulse with a complex electric field amplitude defined by $E(t) = \exp[(-a + ib)t^2]$ [8]. The value of b was inferred by finding the best linear fit to the first derivative of the temporal phase of the pulse.

Measurement	Roundtrip Cavity Dispersion $\frac{d^2\beta}{d\omega^2}$ (fs^2)	Linear Chirp Parameter b (fs^{-2})	SHG-FROG G-error
a	-1110	0.000195	0.0038
b	-470	0.000165	0.0052
c	-260	0.000105	0.0050
d	-40	0.000055	0.0045
e	+170	-0.000205	0.0062

Table 1: Estimated net roundtrip cavity dispersion, SHG-FROG retrieval error and linear chirp parameter inferred from the FROG analysis for each measurement.

Results

The results of the analysis show that, in each case, the full-width half-maximum (FWHM) output pulse durations measured by FROG exceeded those inferred from the interferometric autocorrelation data ($sech^2(t)$ pulse intensity profile assumed) by an amount varying from 4 to 13 %. This discrepancy cannot be attributed to a systematic error in the FROG measurement because of the good agreement between the experimentally measured spectra and autocorrelations and those generated from the retrieved field. Instead the reason for the disagreement is the deviation of the pulse shape from the ideal $sech^2(t)$ profile because of the presence of uncompensated intracavity spectral cubic phase dispersion. The effect of spectral cubic-phase dispersion is seen in the interferometric autocorrelation as a broadening of the wings (see Figures 3(b) [13% discrepancy] and 3(c) [11% discrepancy]) and it is also

obvious in the spectral FROG data as a characteristic "S" shape in the phase. The agreement between the pulse duration inferred from the interferometric autocorrelation and that determined by FROG is best for the pulse measured with least intracavity glass (Figure 3(d) [4% discrepancy]) because uncompensated cubic-phase dispersion is minimised and a soliton-like $sech^2(t)$ solution for the pulse shape is therefore appropriate. In this case the contrast in the wings of the autocorrelation is high and the spectral phase varies exactly linearly with frequency as expected for an unchirped pulse.

A complete analysis of the output pulses from a prism-dispersion-compensated self-modelocked Ti:sapphire has been carried out using spectral, autocorrelation and FROG measurements. Close agreement is seen between the experimental autocorrelation profiles and those calculated using the pulse electric field amplitudes determined by FROG but pulse durations inferred from the autocorrelation data alone by assuming a $sech^2(t)$ amplitude profile appear to underestimate the actual duration by up to 13 % because of deviations from the ideal pulse shape due to the presence of spectral cubic phase dispersion.

Sub- 20 fs Mirror-Dispersion-Controlled Ti:sapphire Laser

This section describes the operation of a Ti:sapphire laser producing transform-limited pulses at sub– 20 fs pulse durations. Exploitation of the bandwidth available from Ti:sapphire has only been possible since the discovery of self-modelocking[9]. The presence of excessive self-phase modulation in such systems means that femtosecond pulse formation in a broad-bandwidth solid-state laser relies on the

introduction of a net negative intracavity group velocity dispersion (GVD). In the Ti:sapphire laser described here, net negative intracavity GVD is introduced using the same high-reflectivity dielectric mirrors that provide the feedback necessary for oscillation. These are specific chirped multilayer dielectric mirrors[10] that have been designed to produce an approximately constant negative intracavity GVD over a broader bandwidth than any other low-loss dispersive optical system to date.

In systems that rely on pairs of prisms for intracavity dispersion compensation, the prism material can be chosen to introduce a minimum amount of cubic-phase distortion. Ti:sapphire oscillators incorporating fused-silica prisms, which were shown to introduce a minimum amount of cubic-phase distortion at 800 nm, have been shown to be capable of producing optical pulses of 10 fs to 15 fs duration[11-13]. These pulse durations were limited by residual cavity third-order dispersion. More recent work, also involving a Ti:sapphire laser with fused-silica prisms in the cavity, revealed that the overall intracavity third-order dispersion reduces to zero at around 850 nm[14,15]. An increase in the modelocked pulse bandwidth beyond about 150 nm does not, however, correspond to a further reduction in the pulse duration and proved to be limited by the fourth-order dispersion of the prisms[16] and possible coherent ringing due to detuning of the laser[17]. Pulses of about 10 fs duration were achieved in this way[18].

In summary, prism-controlled, dispersion-compensated Ti:sapphire lasers are capable of generating high quality, nearly $sech^2$ pulses with durations close to 15 fs. Pulse durations near to 10 fs can be reached only at the expense of detuning the laser and pulses generated in this way are not close to the transform-limit. Chirped multilayer

dielectric mirrors, on the other hand, have made a major impact in the generation of light pulses in the sub- 20 fs regime in particular and have been successfully used in the production of ~6.5 fs duration laser pulses[19]. Careful design allowed higher-order contributions to the mirror phase dispersion to be kept to a minimum, or to be such that it cancels the higher-order phase distortion introduced by the other cavity elements such as the gain medium. The mirror dispersion compensated Ti:sapphire laser presented here uses mirrors that are not the latest design[20] and it delivered transform-limited pulses of 15 fs duration at an output power of ~480 mW.

Chirped Multilayer Dielectric Mirrors

The frequency dependence of the phase dispersion of a chirped multilayer dielectric mirror coating was first investigated in the 1960's[21,22]. The emergence of femtosecond lasers during the 1980's has led to a renewed interest in this field [23-29]. Standard quarterwave dielectric mirrors were shown to introduce negligible dispersion at the centre of their reflectivity range[30-32]. Assorted specific high-reflectivity coatings including Gires-Tournois interferometers[33] and double-stack mirrors[34], were devised for use in femtosecond dye lasers to precisely control the intracavity dispersion. However, the GVD introduced by the mirror coatings was accompanied by high cubic-phase and higher-order contributions to the dispersion. Consequently, a constant GVD could only be obtained over a restricted wavelength range of <10 THz. Broadband GVD control is difficult to achieve because of the physical source of the dispersion in such devices. Fabry-Perot type resonant structures in systems work by trapping different frequencies for different periods of time[35].

The wavelength dependence of the penetration depth of an incident optical field on a multilayer dielectric coating results in the production of a different type of GVD. The presence of resonant structures is not necessary, and it is possible to introduce a GVD which varies with wavelength over a wide bandwidth. For the GVD to be constant, the group delay must vary approximately linearly with wavelength. A light pulse centred at a particular wavelength is most effectively reflected by a corresponding quarterwave stack. Thus a monotonic variation of the multilayer period throughout the chirped coating process results in a penetration depth, and thus a group velocity that also varies monotonically with wavelength. However, it has previously been shown that using multilayer dielectric coatings with monotonic variation in thickness, causes strong Fabry-Perot-like resonance perturbations of the GVD[36]. More recent studies indicate that these undesirable resonances can be almost entirely eradicated by slightly adjusting the thickness of each layer within the multilayer coating.

Typical chirped multilayer dielecric coatings consist of a number of alternating layers of SiO_2 (n=1.45) and TiO_2 (n=2.3) with an optical thickness close to 200 μm (1/4 of the operating wavelength of 800 nm). The layers have increasing thickness towards the mirror substrate so that the group delay introduced would increase with wavelength, and thus would provide negative GVD as required. The mirrors are high reflectivity coated from 700 nm to 900 nm and can be designed to exhibit a slight linear variation so that the cubic-phase dispersion of the gain medium can also be compensated.

A standard electron beam evaporation technique is used to apply the chirped multilayer dispersive coatings to the mirrors. A theoretical refractive index profile[37] of an SiO_2-TiO_2 multilayer coating is shown in Figure 4.

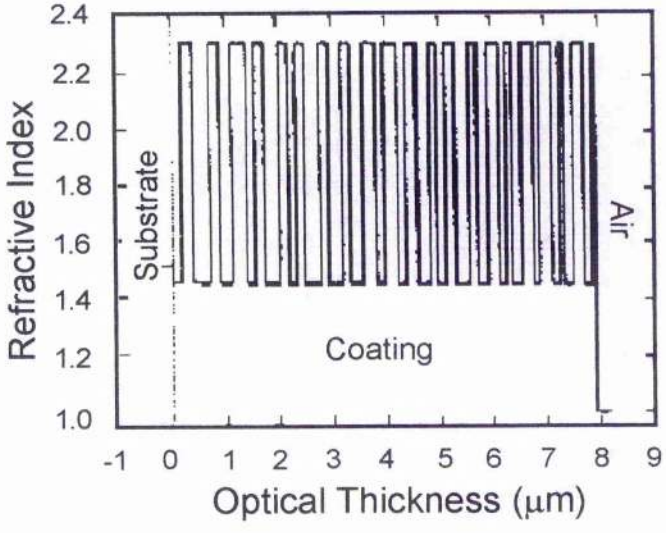

Figure 4: A theoretical refractive index profile of an SiO_2-TiO_2 multilayer coating[37].

Although the variation in optical thickness is not linear in this case, the layer thickness is largest close to the mirror substrate. Reflectivities as high as 99.9 % can be achieved at the centre of the wavelength range and the nominal GVD introduced by the mirrors at 800 nm is typically about -45 fs^2. The mirror also introduces some amount of cubic-phase dispersion typically around -33 fs^3, which allows for the simultaneous compensation of both second and third-order dispersion. The variation of group delay with wavelength[38] for a typical chirped multilayer dielectric coating is shown in Figure 5.

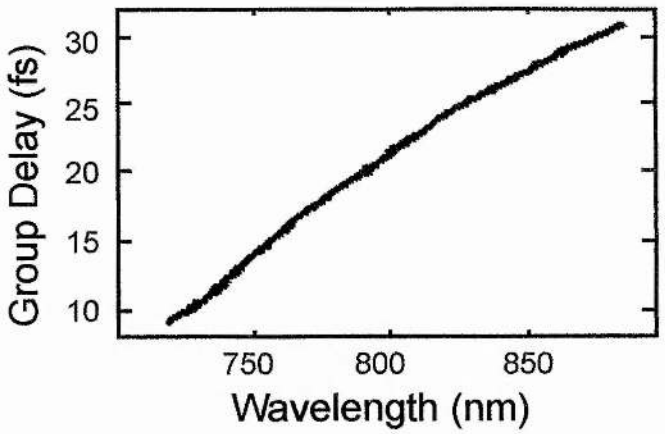

Figure 5: The variation of the group delay with wavelength for a typical chirped multilayer dielectric coating.

The Ti:sapphire Laser Configuration

The dispersion-controlled mirror set used in the Ti:sapphire laser described here comprised specifically designed chirped mirrors for intracavity (GVD) control[39]. Dispersion-engineered mirrors cannot currently be produced with high transmission at the pump wavelength. For this reason, low dispersion quarterwave dielectric mirrors for coupling the pump beam into and the modelocked pulse out of the resonator, were also included. The Ti:sapphire crystal was thin and highly doped, offering the potential to generate high quality, stable modelocked pulses with a high degree of reproducibility and duration of 15 fs or less.

The cavity configuration of the mirror-dispersion-compensated Ti:sapphire laser used in this experiment is shown schematically in Figure 6. A Spectra-Physics Millennia laser (diode-pumped frequency-doubled Nd:YVO_4 laser) providing 5 W of power at 532 nm was used as the pump source for the Ti:sapphire laser. The vertically polarised output from the pump laser was rotated using a periscope arrangement of

mirrors to allow it to enter the Ti:sapphire crystal as horizontally-polarised light. The periscope mirrors were high reflectivity coated from 480nm to 530 nm. The pump beam was focused into the Ti:sapphire crystal using a 35 mm focal length lens.

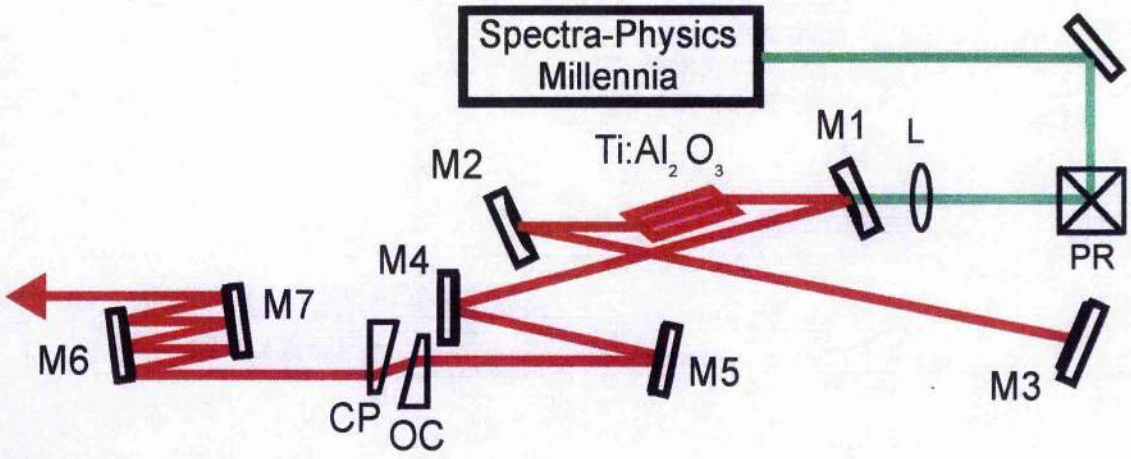

Figure 6: Cavity schematic of the mirror-dispersion-compensated Ti:sapphire laser.

The Ti:sapphire laser crystal had a length of 2.5 mm, with Brewster-angled faces and a pump absorption coefficient of 5.8 cm^{-1}. A Peltier-effect cooler was used to maintain the temperature of the Ti:sapphire crystal at 5°C. Low-pressure water was also used to aid this cooling. The folding section consisted of M1; a quarterwave dielectric mirror and M2; a highly-dispersive chirped mirror, each having a radius of curvature of -50 mm. These mirrors were broadband high reflectivity coated from 700 nm to 900 nm, and M1 was highly transmitting at the pump wavelength. M3, M4, M5, M6 and M7 were plane highly dispersive chirped mirrors, which were again high reflectivity coated for 700 nm to 900 nm. M6 and M7 were used for extracavity dispersion-control.

The cavity also comprised an output coupler (OC) with 16.5 % transmission at 790 nm on a wedged substrate along with a compensating plate (CP), which was AR-coated for 790 nm. The spatial chirp and associated pulse front tilt induced on transit through the wedged output coupler, was compensated for using the second wedged glass plate, which was identical to the output coupler substrate. This plate, which had a varying thickness, also aided the extracavity chirped dispersive mirrors in the continual tuning of the extracavity dispersion about zero GVD. The positive material dispersion introduced by the output coupler, the compensating plate and the beamsplitter included in the autocorrelator was also compensated for using the extracavity mirror pair. The number of reflections off each mirror could be adjusted accordingly. Steering and characterising the broadband optical pulses available from this system had to be achieved very carefully.

The output from the laser was characterised using a standard autocorrelator arrangement as described in Chapter 1, with modifications to reduce the amount of dispersion introduced to the pulse by the autocorrelator optics. Gold-coated mirrors were used to in place of the retroreflectors, as they have broadband high reflectivity at 800 nm. In place of the lens, a hyperbolic mirror was used to focus the light into the detector; this was also gold-coated. The detector was a gallium arsenide phosphide (GaAsP) photodiode, with E_g=680 nm[40]. A thin beamsplitter, which was AR-coated at 790 nm, was also included and this helped to minimise the dispersion introduced on the pulse.

Results

The interferometric autocorrelation and the pulse spectrum, describing the modelocked output from the laser are shown in Figure 7. Assuming a $sech^2$ pulse profile, near transform-limited pulses with $\Delta\nu\Delta\tau$=0.29, and of 15 fs duration were generated at a repetition rate of 78 MHz. Output powers of 480 mW were available from this system. The broad spectrum, of ~40 nm, is symmetric indicating the absence of significant higher-order dispersion in the cavity.

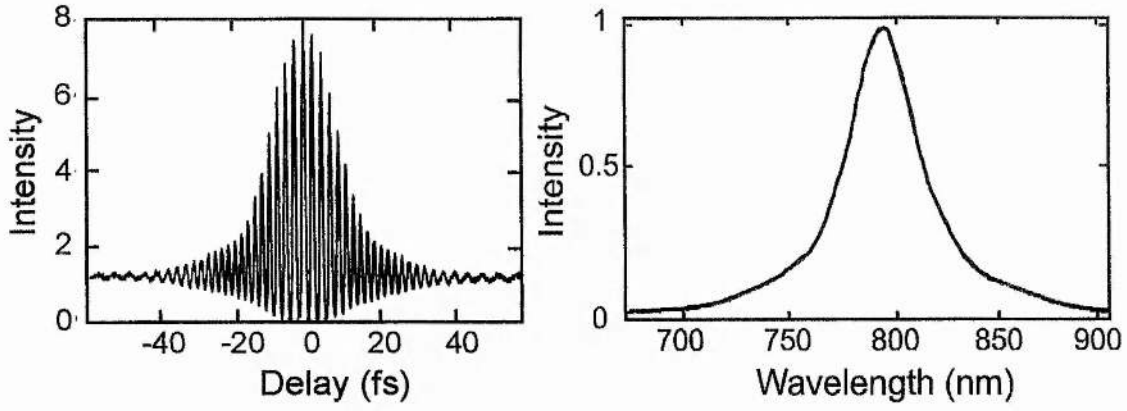

Figure 7: The interferometric autocorrelation and the pulse spectrum describing the modelocked output from the mirror-dispersion-compensated Ti:sapphire laser.

Conclusions

In this chapter the operation and characterisation of two different Ti:sapphire laser systems involving different methods of dispersion compensation has been described. The first laser produced 100 fs duration self-modelocked laser pulses and dispersion compensation was achieved by including a pair of prisms in the cavity. Output powers of the order of ~900 mW were available from this system. This laser system is

discussed further in Chapter 5, where it is operated in conjunction with a Spectra Physics Millennia pump laser in an all-solid-state OPO based on periodically-poled lithium niobate (PPLN). The output powers available from this system were sufficient to pump the OPO, and pulse durations of the order of 200 fs were obtained by including a pair of prisms in the OPO cavity to compensate for the dispersion.

The second laser produced self-modelocked pulses of ~15 fs duration and dispersion compensation was achieved using chirped multilayer dielectric mirrors in the cavity. Output powers of around 480 mW were available from this system. It was originally intended that this laser would also be used as the pump source for a PPLN-based OPO. Shorter pump pulses, as were available from this laser, opened up the possibility of producing shorted pulses from the OPO. Pulses of ~50 fs duration have been obtained from a noncritically-phasematched OPO based on KTP[41], which employed chirped multilayer dielectric mirrors in the OPO cavity. The OPO described in Chapter 5 was modified in a number of ways to reduce the intracavity dispersion introduced by the cavity optics, and a shorter pulse version of this system is described in Chapter 6. The Ti:sapphire laser which was actually used to pump this PPLN-based OPO was a ring laser cavity, which included four prisms to provide dispersion compensation, and which was capable of generating sub– 15 fs duration pulses at higher output powers than were available from the mirror-dispersion-compensated Ti:sapphire laser system. This Ti:sapphire laser is described in more detail at the beginning of Chapter 6.

Chapter 3

References

1. B.B Ju, E.A De Souza, W.H Knox, M.C Nuss and J.E Cunningham, Ultrafast Phenomena (optical Society of America, Washington D.C., 1994) Vol. 7 of 1994 OSA Technical Digest Series.
2. P.B Corkum, F Brunel and N.K Sherman, *Phys. Rev. Lett.* **61** 2886 (1988)
3. D Du, X Liu, G Korn, J Squier and G Mourou, *Appl. Phys. Lett.* **64** 3071 (1994)
4. Z.E Penman, T Schittkowski, W Sleat, D.T Reid and W Sibbett, *Opt. Commun.* (accepted)
5. D. J. Kane and R. Trebino, *IEEE J. Quantum. Electron.* **29**, 571 (1993)
6. K. W. Delong, R. Trebino, J. Hunter and W. E. White, *J. Opt. Soc. Am. B* **11**, 2206 (1994)
7. K. W Delong and R Trebino, *J. Opt. Soc. Am. A* **11**, 2429 (1994)
8. A. E Siegman, Lasers (University Science, Mill Valley, California, 1986) Ch 9
9. D.E Spence, P.N Kean and W Sibbett, *Opt. Lett.* **16** 42 (1991)
10. R Szipocs, K Ferencz, C.L Spielmann and F Krausz, *Opt. Lett.* **19** 207 (1994)
11. P.F Curley, C.L Spielmann, T Brabec, F Krausz, E Wintner and A.J Schmidt, *Opt. Lett.* **18** 54 (1993)
12. B Proctor and F Wise, *Appl. Phys. Lett.* **62** 490 (1993)
13. M Asaki, C Huang, D Garvey, J Zhon, H.C Kapteyn and M.M Murnane, *Opt. Lett.* **18** 977 (1993)
14. B.E Lemoff and C.P.J Barty, *Opt. Lett.* **18** 57 (1993)
15. C.L Spielmann, P.F Curley, T Brabec and F Krausz *IEEE J. Quantum. Electron.* **30** 1100 (1994)

16. I.P Christov, M.M Murnane, H.C Kapteyn, J Zhou and C Huang, *Opt. Lett.* **19** 1465 (1994)

17. J.D Harvey, J.M Dudley, P.F Curley, C.L Spielmann and F Krausz, *Opt. Lett.* **19** 972 (1994)

18. C.L Spielmann, P.F Curley, T Brabec and F Krausz *IEEE J. Quantum. Electron.* **30** 1100 (1994)

19. I.D Jung, F.X Kartner, N Matuschek, D.H Sutter, F Morier-Genoud, Z Shi, V Scheuer, M Tilsch, T Tschudi and U Keller, *Appl. Phys. B* **65** 137 (1997)

20. C.L Spielmann, R Szipocs, A Stingl and F Krausz, *Phys. Rev. Lett.* **73** 2308 (1994)

21. C.F Bruce and P.E Giddor, *J. Opt. Soc. Am.* **50** 295 (1960)

22. J.M Bennett, *J. Opt. Soc. Am.* **54** 612 (1964)

23. W Dietel, E Dopel, K Hehl, W Rudolph and E Schmidt, *Opt. Commun.* **50** 179 (1984)

24. S De Silvestri, P Laporta and O Svelto, *Opt. Lett.* **9** 335 (1984)

25. D.N Christodoulides, E Bourkoff, RI Joseph and T Simos, IEEE *J.Quantum. Electron.* QE-**22** 186 (1986)

26. A.M Weiner, J.G Fujimoto and E.P Ippen, *Opt. Lett.* **10** 71 (1986)

27. W.H Knox, N.M Pearson, K.D Li and Ch.A Hirlimann, *Opt. Lett.* **13** 574 (1988)

28. M Beck and I.A Walmsley, *Opt. Lett.* **15** 492 (1990)

29. K Ferencz and R Szipocs, *Opt. Eng.* **32** 2525 (1993)

30. W Dietel, E Dopel, K Hehl, W Rudolph and E Schmidt, *Opt. Commun.* **50** 179 (1984)

31. S De Silvestri, P Laporta and O Svelto, *Opt. Lett.* **9** 335 (1984)

32. W.H Knox, N.M Pearson, K.D Li and Ch.A Hirlimann, *Opt. Lett.* **13** 574 (1988)

33. J Heppner and J Kuhl, *Appl. Phys.Lett.* **47** 453 (1985)

34. M Yamashita, K Toriznka and T Sato, IEEE *J. Quantum Electron.* QE-23 2005 (1987)

35. P Laporta and V Magni, *Appl. Opt.* **24** 2014 (1985)

36. P Laporta and V Magni, *Appl. Opt.* **24** 2014 (1985)

37. R Szipocs, K Ferencz, C Spielmann and F Krausz, *Opt. Lett.* **19** 201 (1994)

38. R Szipocs, K Ferencz, C Spielmann and F Krausz, *Opt. Lett.* **19** 201 (1994)

39. Stingl OEG, Kleinengersdorferstr. 24, A-2100 Korneuburg, Austria

40. Photodiodes data sheet, Hamamatsu Photonics K.K., Solid State Division

41. J Hebling, H Giessen, S Linden and J Kuhl, *Opt. Commun.* **141** 229 (1997)

CHAPTER 4

Mid-infrared Optical Parametric Oscillator Based on Periodically-poled Rubidium Titanyl Arsenate

---

There are a number of important applications of femtosecond optical pulses in the mid-infrared including those in spectroscopy and atmospheric testing. In spectroscopy, there are many processes which occur in semiconductors, that can be monitored only with the use of femtosecond pulses at wavelengths between 3 μm and 5 μm[1-3]. High pulse powers are also required, and a broad tuning range is an advantage in examining the variety of kinetic processes within any single system[4,5]. Time-resolved mid-infrared spectroscopy is also used in the analysis of the dynamics of chemical processes and reactions[6-9] although pulse powers need not be as high as in semiconductor spectroscopy. In atmospheric testing, long-range atmospheric sensing and environmental pollution-monitoring[10-12] are possible because mid-infrared wavelengths can be used to measure the absorption spectra of atmospheric gases[13].

Results from the first demonstration of a periodically-poled lithium niobate (PPLN) based optical parametric oscillator[14] were sufficiently encouraging, that when periodically-poled rubidium titanyl arsenate (PPRTA) became available, we were curious to see if it exhibited the same extensive tuning range in the mid-infrared, as previously seen with PPLN. There were a number of reasons why these results were important. The first is that a pump wavelength of greater than 830 nm is required to operate the OPO, and this meant that longer idler wavelengths could be reached using

the available mirror sets. Secondly, the effects of photorefractive damage are not as apparent in PPRTA as in PPLN so the OPO could be operated with the crystal at a lower temperature. A picosecond OPO-based on PPRTA has been demonstrated[15], which operated with the PPRTA crystal at room temperature, thereby eliminating the inconvenience of having the oven in the cavity. PPRTA has a higher transmission than PPLN at wavelengths from 4 μm to 5 μm. RTA is also easier to pole than, for example, $KTiOPO_4$ (KTP), because of its particularly low ionic conductivity. Some of the optical properties of RTA and PPRTA are explained in the following sections by way of an introduction to the PPRTA-based OPO.

Optical Properties of RTA and PPRTA

RTA ($RbTiOAsO_4$) belongs to the group of crystals better known as the titanyl arsenates, and thus has a chemical structure of the form $MTiOXO_4$. M is one of K, Rb, Cs, Tl or NH_4 and X is either P or As. Every crystal in the group has an orthorhombic structure and is biaxial. RTA belongs to the crystallographic point group *mm*2 and has a space group $Pna2_1$. The structure of a titanyl arsenate is noncentrosymmetric and is characterised by chains of TiO_6 octahedra, linked at two corners and separated by XO_4 tetrahedra[16]. The crystal structure of RTA is shown in more detail in Figure 1, and it is this crystal structure that gives RTA its nonlinear optical properties.

In order that periodic-poling of a crystal is possible, the crystal must be ferroelectric. Ferroelectric materials must have a noncentrosymmetric structure. The structure of a ferroelectric crystal comprises permanent spontaneous electric field domains, which

can be reversed on application of an externally applied electric field. Flux grown RTA[17] can be periodically-poled using the procedure described already in Chapter 2. There are advantages of electric field poling of RTA over, for example $LiNbO_3$, which is discussed in Chapter 5, because significantly lower poling voltages are required to invert the ferroelectric domains.

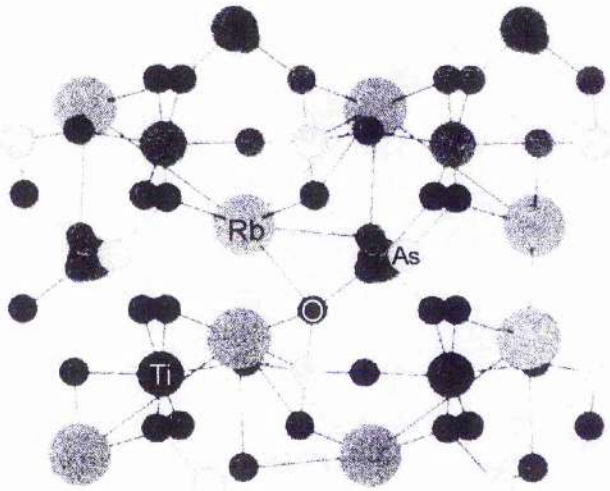

Figure 1: The crystal structure of RTA viewed along [010].

Also RTA[18] (or KTP) has a highly one-dimensional structure along its polar axis, which inhibits the leakage of the inverted polarisation into neighbouring domains within the crystal. This allows more accurate control of the duty cycle between poled and unpoled regions of the crystal. To achieve domain reversal, the coercive field voltage must be maintained over the sample. During this time the energy needed to convert the crystal lattice is reached and a small current flows through the crystal. This corresponds to the transfer of charge throughout the crystal structure. If this current becomes too large, it can have a random and detrimental effect on the poling process. This can be a problem when periodic-poling of flux grown KTP[19] is

carried out, but is not significant when RTA is poled because RTA is more than three orders of magnitude less conducting than KTP.

The Ti-O bonds are alternately long and short as they recur along the chains of TiO_6 octahedra. This causes some degree of distortion to the TiO_6 octahedra, which is responsible for the nonlinear and electro-optic effects observed in RTA. The optical properties of RTA were published originally in 1993 by Han et al[20]. Since then measurements of some of the main properties of the crystal, including refractive index, transparency and optical nonlinearity have been reported.

The variation of the ordinary and extraordinary refractive index with wavelength, over the range 0.403 μm to 3.6 μm is shown in Figure 2. This is based on the results of Fenimore et al.[21] and from this, Sellmeier coefficients for RTA were derived. These are given in Table 1, and in this case are related by:

$$n = \sqrt{A + \frac{B}{1 - \left(\frac{C}{\lambda}\right)^2} - D\lambda^2} \,. \qquad (4.1)$$

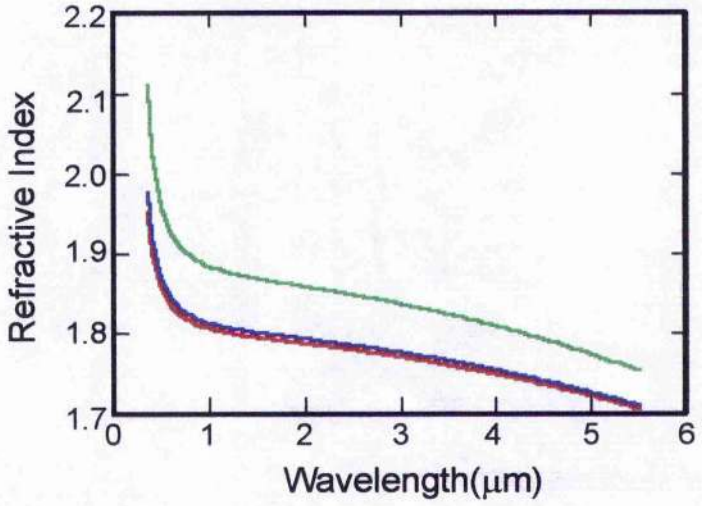

Figure 2: A graph of the variation of refractive index with wavelength in RTA: n_x is shown in red, n_y is shown in blue and $n_z(n_e)$ is shown in green.

Sellmeier Coefficient	n_x	n_y	$n_z(n_e)$
A	2.04207	2.14941	2.18962
B	1.17785	1.09267	1.30103
C	0.20157	0.21462	0.22809
D	0.01035	0.01067	0.01390

Table 1: Sellmeier coefficients of RTA[21], which can be substituted into Equation (4.1) to calculate n_e.

The transparency range of RTA extends to ~5.3 μm[22] and so RTA is suitable for the generation of mid-infrared wavelengths, but this cannot be achieved using conventional noncritical birefringent phasematching because of problems with walk-off compensation. The use of PPRTA, however, means that these problems can be

eliminated and wavelengths in the 4 μm to 5 μm region of the spectrum can readily be generated. The optical transmission of RTA is shown in Figure 3, for the wavelength range 2 μm to 6 μm.

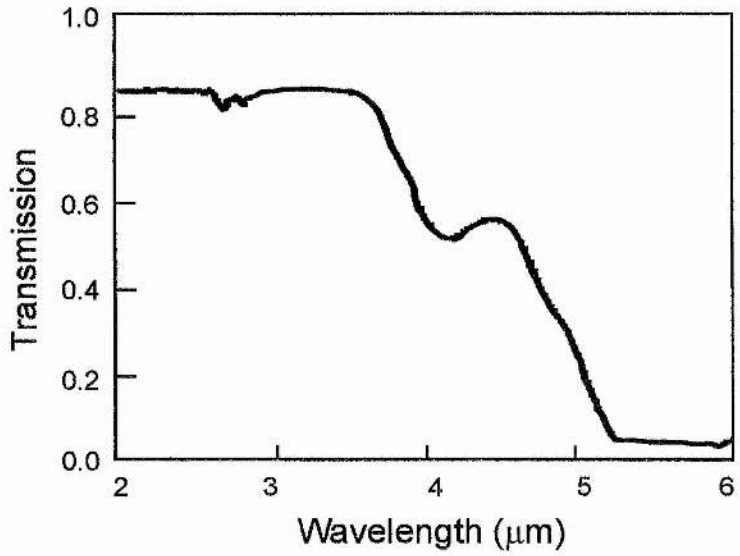

Figure 3: Transmission of RTA in the mid-infrared.

In RTA, there are only three non-zero nonlinear coefficients, namely d_{31}, d_{32}, and d_{33}. The most recently published values for these nonlinear coefficients are d_{31}=2.3 pm/V, d_{32}=3.8 pm/V and d_{33}=15.8 pm/V, from a paper by Cheng et al.[23]. In RTA, the d_{33} coefficient is significantly larger than the other nonlinear coefficients and can be accessed only by employing quasi-phasematching techniques in PPRTA. PPRTA has a relatively large effective nonlinear coefficient, with $d_{eff}\approx$10 pm/V and so conversion efficiencies in optical parametric oscillation in RTA are potentially higher than in some other materials.

Phasematching in PPRTA

The purpose of the experiment described in this chapter was to construct a femtosecond OPO based on the PPRTA crystal and to investigate its tuning range. In order to establish the most appropriate choice of pump wavelength, grating period and oscillation wavelength for the longest possible idler wavelengths to be generated, some theoretical modelling was used to generate the phasematching curve shown in Figure 4 below.

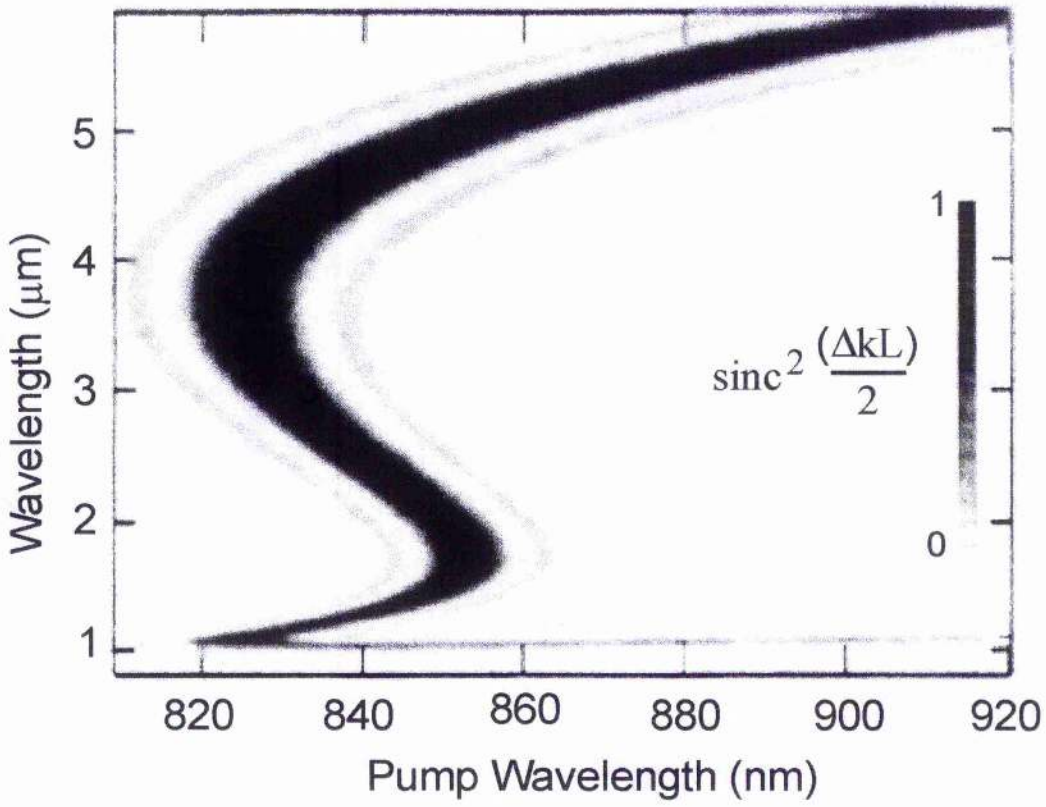

Figure 4: Phasematching curve for PPRTA over the range of wavelengths available from the pump laser. The sinc ^{2} variation of gain with the highest areas of gain shown in black.

The solution to the phasematching equation for PPRTA defines a range of wavelengths for which momentum and energy conservation are achieved and optical parametric generation is possible. The variation of gain across this wavelength range has a $sinc^2$ dependence, and because the gain bandwidth is so large in PPRTA optical parametric oscillation is still possible even for wavelengths where $\Delta k \neq 0$ but has a value close to zero.

Theoretical modelling was carried out to predict the wavelengths that would be phasematchable for the PPRTA-based OPO. For a range of pump wavelengths including those that are available from the Ti:sapphire laser, that is, 780 nm to 860 nm for the mirror-set used, the phasematching curve for PPRTA at 35 °C and a grating period of 30 μm, was calculated and is shown in Figure 4. This plot is generated form the Sellmeier equations already given and includes the $sinc^2$ variation of the gain bandwidth (from Equation (2.8)). The areas shown in black on the plot have the highest gain.

The phasematching curve and the variation of the gain bandwidth across the tuning range which it defines, were used to predict the behaviour of the output from the PPRTA-based OPO. It suggested that a pump wavelength of 830 nm to 840 nm combined with a signal wavelength of 1.1 μm would provide the best chance of generating idler wavelengths in the region of 5 μm. The crystal grating period was 30 μm.

Mid-infrared Femtosecond Optical Parametric Oscillator Based on PPRTA

The titanyl-arsenates and RTA in particular, have been used widely in bulk crystal form for Ti:sapphire-pumped femtosecond OPOs[24-27] because of their good crystal quality, relatively high nonlinear coefficients, and broad birefringent phasematching range. To operate at wavelengths beyond 3 μm using these crystals it is necessary to employ a critically-phasematched noncollinear geometry, which reduces the single-pass gain and requires sensitive detection equipment to align. Quasi-phasematching (QPM) makes it possible to combine the convenience of non-critical phasematching with the wavelength coverage of a critical geometry and in practice this is realised by the technique of periodic poling. To date, quasi-phasematched infrared OPOs have relied exclusively on PPLN[28] which can be used to produce idler wavelengths of longer than 5 μm and, in our own laboratory, we have generated idler wavelengths as long as 5.36 μm[29] from a femtosecond PPLN-based OPO. This is discussed further in Chapter 5. Some unresolved issues with PPLN (notably thermal effects, photorefraction and restricted aperture sizes) mean that for certain applications other materials may prove to be more practical, however PPLN has been successfully utilised in a synchronously-pumped picosecond OPO without any significant photorefractive or thermal damage[30]. The crystal isomorphs of KTP are characterised by a relatively low coercive field, which in combination with their highly anisotropic structure and low temperature dependence, allows them to be fabricated by periodic poling into large aperture QPM devices suitable for high power applications. Of these isomorphs, the particularly low ionic conductivity of RTA makes it easier to pole than KTP[31], and its greater transmission in the 4 μm to 5 μm

wavelength region allows it to be used in frequency down-conversion applications for which KTP is not suitable.

The Pump Laser

The pump source for the femtosecond OPO presented in this chapter was a commercial continuous wave (cw) Ti:sapphire laser which was modified for self-modelocking. The original system was a Spectra-Physics 3900S four-mirror resonator to which a number of elements were added to facilitate modelocking. A birefringent filter used for cw tuning was removed and the resulting cavity is shown schematically in Figure 5. The modifications increased the cavity length to approximately 1.75 m.

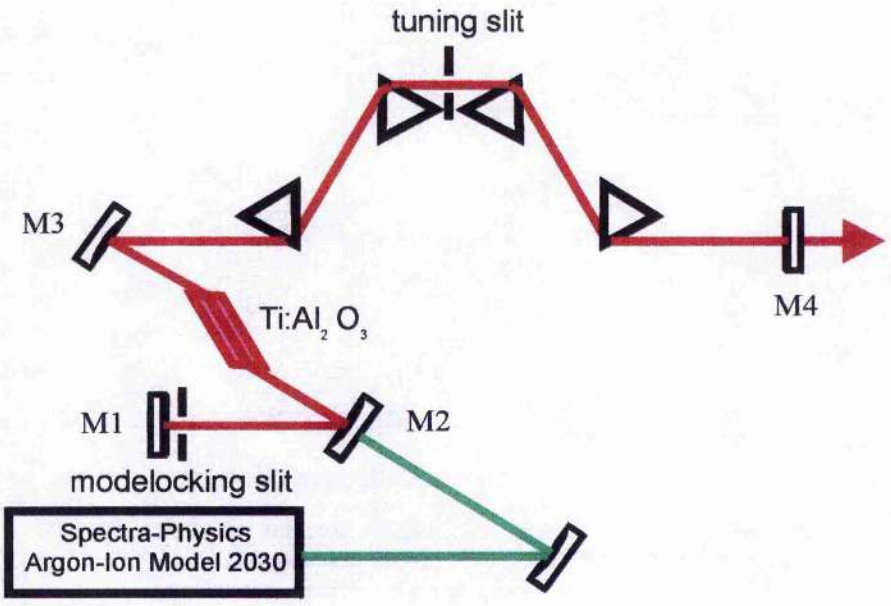

Figure 5: The configuration of the Ti:sapphire laser used as a pump source for the PPRTA-based OPO described in this chapter.

The Ti:sapphire laser was pumped using an argon-ion laser running on all-lines (488 to 514 nm), in a TEM_{00} mode and with an output power of 15 W. The pump beam was focussed into the Ti:sapphire cavity using a mirror with radius of curvature of –228 mm. The two curved Ti:sapphire cavity mirrors had radii of curvature of –100 mm; M1 was a plane mirror which was high reflectivity coated and M4 was a 20 % output coupler. Each mirror had a broadband high reflectivity coating in the 750 nm - 900 nm spectral range. The 20 mm long Ti:sapphire crystal was Brewster-cut and it was cooled using a low-pressure water supply.

The effects of group velocity dispersion and self-phase modulation on pulse propagation in OPOs have already been discussed. These effects also occur in ultrashort pulse lasers, leading to pulse broadening and spectral distortion and this must be accounted for. A sequence of four SF10 prisms was included in the laser cavity to achieve this; apex separations of 30 cm were sufficient to produce transform-limited pulses. Typical autocorrelation and spectral measurements from this laser are presented in Figure 6. Assuming a $sech^2$ pulse profile, near transform-limited pulses with $\Delta\nu\Delta\tau=0.34$, and of ~106 fs duration were produced from this laser.

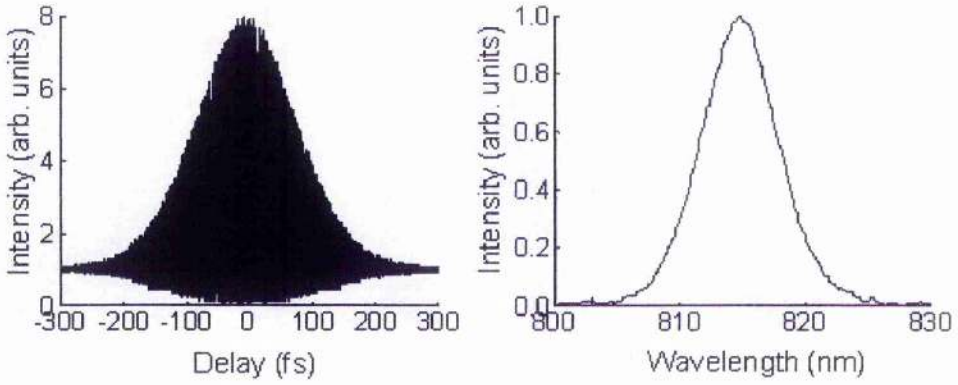

Figure 6: Typical autocorrelation and spectral measurements from the Ti:sapphire laser.

To facilitate modelocking a hard aperture was positioned close to mirror M1.It was adjustable in the vertical direction to discriminate against cw operation. The optimum cavity configuration for modelocking was found by translating mirror M3. An additional aperture was inserted between the second and third prisms to allow the laser wavelength to be tuned. At this point in the cavity the beam was spectrally dispersed, so by scanning a slit horizontally across the beam, the desired operating wavelength could be selected.

The laser produced average modelocked pulse durations of ~100 fs at output powers between 1 and 2 W, with the most stable operation at an output power of 1.4 W, and at a repetition rate of ~83 MHz. Under these conditions modelocked operation could be sustained for several hours in the absence of any external vibrations perturbing the system.

The PPRTA-Based OPO

The RTA crystal used in the work described here was prepared by the Institute of Optical Research[32] from an 8 mm long × 1 mm thick sample by patterning a photoresist grating with a period of 30 μm on to the c+-face. Electrical contact with the crystal was made by a KCl electrolyte and the sample was poled using 12 ms long voltage pulses of 2.0 kV. The quality of the QPM structure was evaluated by carrying out sixth-order second harmonic generation using a cw source with a fundamental wavelength of 914 nm. The width of the phasematching peak obtained implied an effective interaction length equivalent to about 80 % of the total grating length and an effective nonlinear coefficient of $d_{eff} \sim 10$ pm/V was also implied. The sample was cut to obtain a 2 mm long crystal whose end faces were polished and subsequently coated with an antireflection coating at a centre wavelength of 1.1 μm. The crystal length was selected to allow comparison of the results with those from a previous OPO which used a 2-mm long bulk RTA crystal[33]. Using the PPRTA sample we configured a singly-resonant femtosecond OPO in a three-mirror standing-wave V-cavity. This is shown in Figure 7.

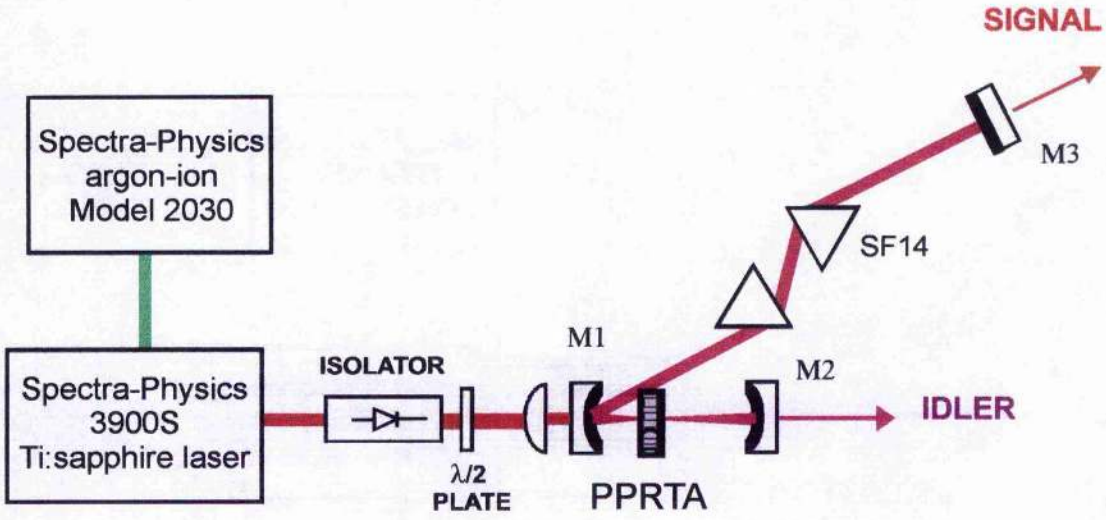

Figure 7: A schematic diagram of the PPRTA-OPO cavity configuration.

A temperature controller and oven were used to maintain the crystal at around 35 °C to avoid minor signs of photorefractive damage which were apparent at room temperature. The concave focusing mirrors, M1 and M2, had a radius of curvature of -100 mm and all mirrors were coated for high-transmission at 800 nm and high-reflectivity at a signal wavelength of 1.1 μm. The mirror substrate material was CaF_2, which is transparent to beyond 5 μm, and the transmission of this coating at the idler wavelength was approximately 75 %.

The focusing optics were chosen to give a minimum signal beam radius, which was 18 μm. The pump beam was focused using a 50 mm focal length lens to a radius of 15 μm. The polarisations of the pump, signal and idler waves were all horizontal in the cavity (all e-waves) and were parallel to the poling direction, which lies along the crystallographic c-axis. In RTA this direction is equivalent to the optical z-axis ($n_Z > n_Y > n_X$) and the piezoelectric Z-axis.

In the first instance, the resonator was configured without dispersion compensation. Interferometric autocorrelation measurements of the signal output indicated that the pulses were strongly frequency-chirped, as expected, and had durations of 750 fs. Using a 1 % signal output coupler(M3), 70 mW of average output power was extracted at a wavelength of 1.1 μm. By cavity-length tuning the OPO towards the long wavelength cut-off of the high-reflectivity mirrors, a total output power of 120 mW at 1.22 μm, was extracted, with an effective cavity output coupling of 12 %. The pump-power oscillation threshold for this configuration was 265 mW and a maximum pump depletion of 52 % was observed. Cavity-length tuning of the uncompensated OPO was rapid, and a length increase of 26 μm was sufficient to tune the signal centre wavelength across the entire mirror bandwidth from 1.072 μm to 1.225 μm. This cavity-length tuning range is significantly greater than that observed from a 2-mm long crystal of RTA which was not poled, and can be explained by the approximately sixfold increase in phasematching bandwidth available in the QPM geometry. This wide bandwidth is associated with the retracing behaviour of the OPO output wavelengths under pump tuning is illustrated in Figure 8 for a 2-mm long crystal with a 30 μm grating period. Wavevector mismatch ($\Delta k = k_p - k_s - k_i - k_g$) is shown varying from perfect phasematching (black) to a mismatch equal to or exceeding the phasematching bandwidth (white). The tuning rate, $\frac{d\lambda}{dL}$, derived from the experimental results is 0.0059 where L is the length of the standing-wave cavity. The single-pass dispersion can be obtained for the cavity using,

$$\frac{d^2\phi}{d\omega^2} = \frac{\lambda^2}{2\pi c^2}\left(\frac{d\lambda}{dL}\right)^{-1}, \tag{4.2}$$

and the tuning data imply a value of +400 fs^2. The single-pass dispersion contributed by the material dispersion of the crystal itself can be calculated from the Sellmeier equations for RTA[34] to be +320 fs^2 which implies a residual cavity dispersion of +80 fs^2 associated with the air and the resonator mirrors.

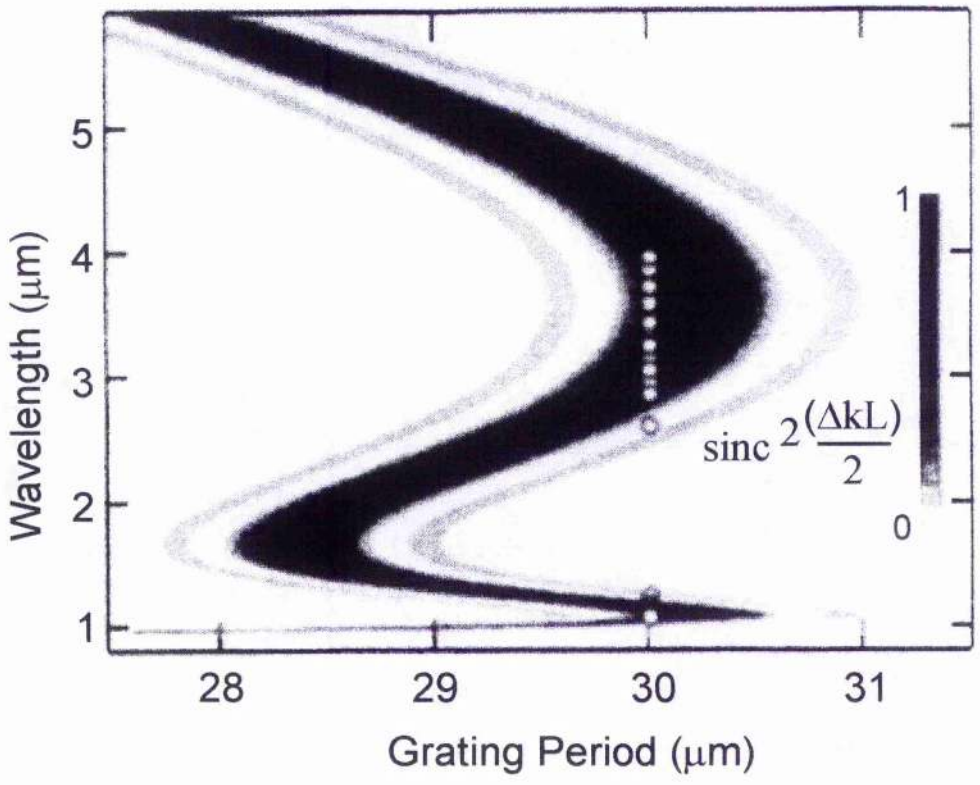

Figure 8: Pump wavelength tuning and phasematching bandwidth of a 2-mm long PPRTA crystal with a grating period of 30 μm.

Intracavity dispersion compensation was implemented using a pair of SF14 prisms with an apex separation of 300 mm and cavity-length tuning generated signal spectra from 1.068 μm to 1.225 μm (Figure 9(a)) and implied a single-pass cavity dispersion of -270 fs^2.

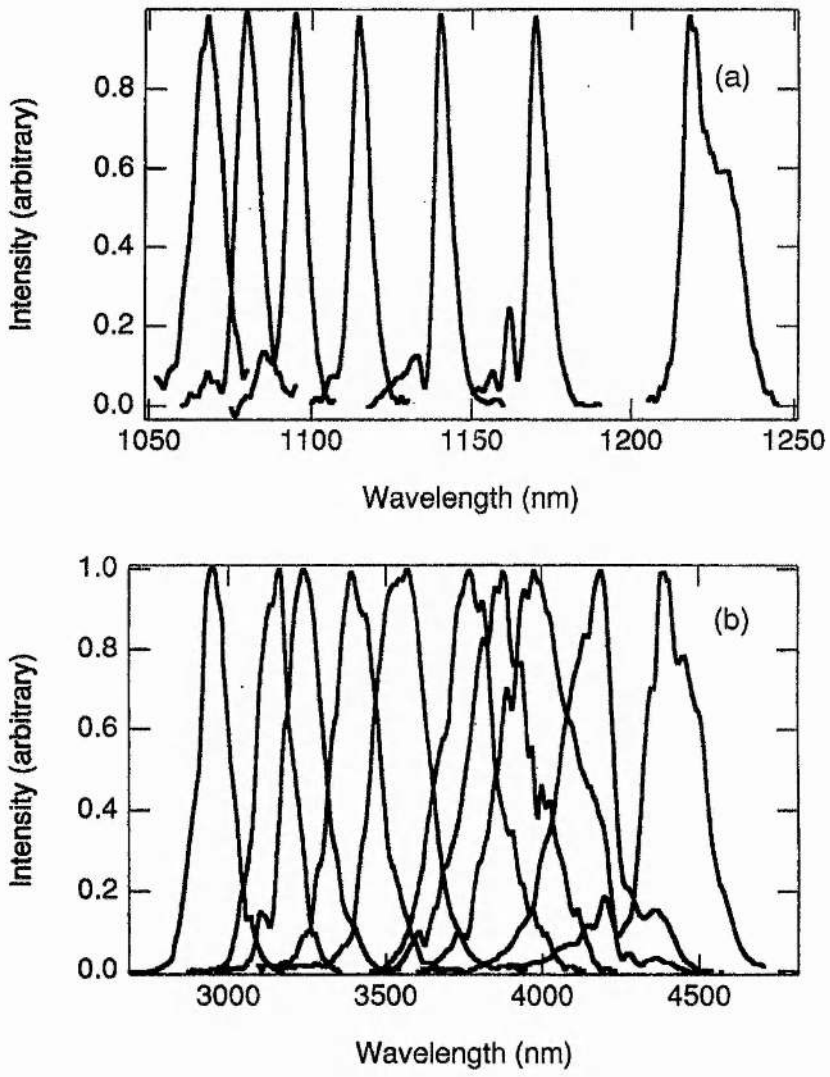

Figure 9: Signal (a) and idler (b) spectra illustrating the tuning range of the PPRTA-OPO. The complete wavelength ranges covered by the OPO were 1.060 μm – 1.225 μm for the signal wave and 2.67 μm - 4.5 μm for the idler.

The maximum signal power extracted was 120 mW at 1.2 μm. An interferometric autocorrelation and corresponding spectrum at a signal wavelength of 1.105 μm are shown in Figure 10 and imply that the pulses are quite close to the transform-limit with $\Delta\nu\Delta\tau = 0.36$.

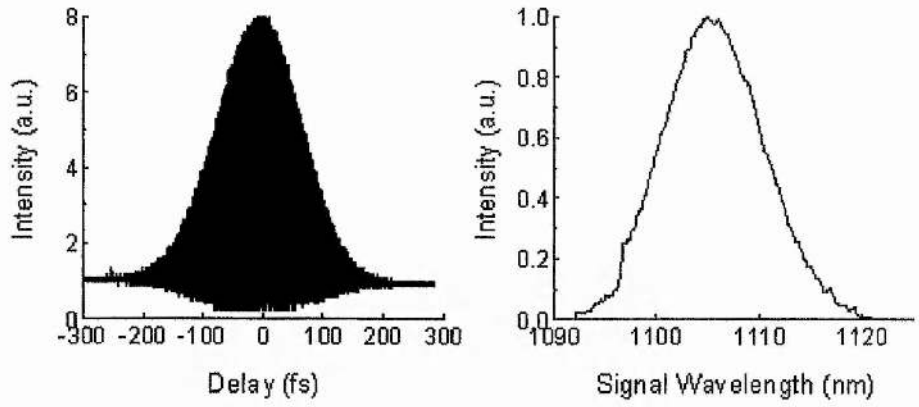

Figure 10: Interferometric autocorrelation and corresponding spectrum of the signal pulses from the intracavity dispersion-compensated PPRTA-OPO operating at a wavelength of 1105 nm.

The idler output wavelengths extended from 2.67 μm to 4.5 μm and representative spectra recorded from the dispersion-compensated OPO are shown as Figure 9(b). Power measurements across this range are plotted as Figure 11 for the OPO with (circles) and without (squares) signal dispersion compensation. All measurements were recorded for a pump wavelength of 830 nm except for those above an idler wavelength of 3.9 μm, which corresponded to a pump wavelength of 852 nm. Tuning to idler wavelengths beyond 4.5 μm requires longer pump wavelengths which could not be generated using the mirror-set of the Ti:sapphire laser used.

The maximum idler power recorded was 105 mW from the uncompensated cavity at a wavelength of 2.8 μm and was a few milliwatts at 4.5 μm.

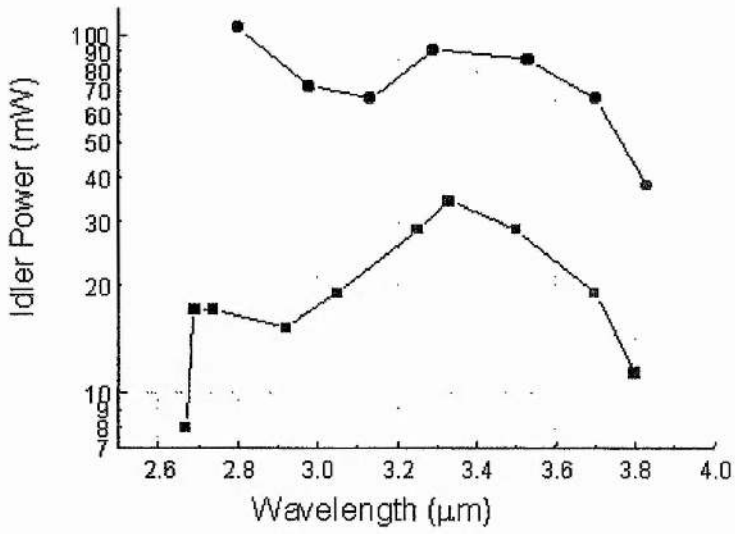

Figure 11: Average idler power recorded as a function of wavelength for the PPRTA-OPO operated with (circles) and without (squares) intracavity dispersion compensation. All measurements were made with a pump wavelength of 830 nm except for the two longest-wavelength data points, which correspond to a pump wavelength of 852 nm.

Figure 12 depicts an interferometric autocorrelation profile and a corresponding spectrum measured at a wavelength of 3.26 μm. The autocorrelation and detection were carried out simultaneously using the nonlinear response of an InGaAs photodiode[35]. Assuming a $\text{sech}^2(t)$ pulse intensity profile, the pulse duration was inferred from the autocorrelation to be 115 fs and, together with the spectral data, this implies a pulse time-bandwidth product of 0.46 which is close to transform-limited.

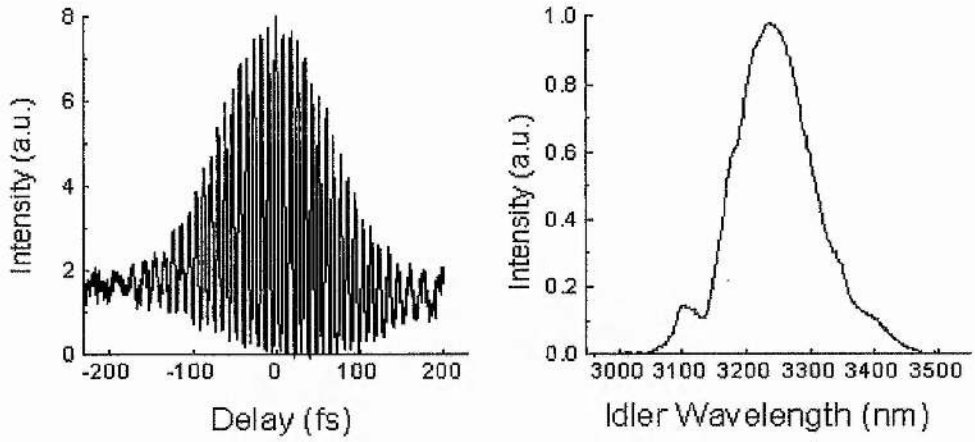

Figure 12: Interferometric autocorrelation and accompanying spectrum of the idler pulses from the PPRTA-OPO operating at a wavelength of 3.26 μm.

Conclusions

In this chapter the operation and characterisation of an OPO based on PPRTA has been described. Ti:sapphire pump tuning and OPO cavity-length tuning has produced wavelengths throughout the range 1.060 μm to 1.225 μm in the signal and 2.67 μm to 4.5 μm in the idler with average output powers as high as 120 mW in the signal and 105 mW in the idler output[36]. The effects of photorefractive damage were minimal and consequently this offered the possibility of operation of the PPRTA-based OPO with the crystal at 35 °C, close to room temperature. The extensive tuning range measured renders PPRTA a viable alternative to PPLN for frequency down-conversion applications in the near and mid-infrared.

Until recently, telecommunication systems have predominantly relied upon colour-centre lasers[37], self-modelocked Cr^{4+}:YAG lasers[38] and optical parametric

oscillators to generate wavelengths close to 1.5 μm. Colour-centre lasers are limited by their use of cryogenic-cooling methods and self-modelocking of Cr^{4+}:YAG lasers has met with practical difficulties in sustaining oscillation close to the water absorption at 1.4 μm. More recent work in this field[39] has shown that it is also possible to construct a femtosecond OPO based on PPRTA that is continuously tunable from 1.375 μm to 1.575 μm for the signal thus overcoming the limits of some other systems. Output powers as high as 110 mW were obtained from this system at a wavelength of 1.46 μm.

The following chapter concerns the generation of longer idler wavelengths, in the region of 5 μm, from an all-solid-state OPO based on periodically-poled lithium niobate. Having already generated 4.55 μm from a PPLN-based OPO[40], the choice of grating period and mirror sets combined with the longest available pump wavelength of 840 nm, we believed that PPLN was a more suitable choice of crystal for the OPO than PPRTA, in this case.

Chapter 4

References

1. M Cavallari, G.M Gale, F Hache, L.I Pavlov and E Rousseau, *Opt. Commun.* **114** 329 (1995)
2. S Adachi, S Takeyama and Y Takagi, *Opt. Commun.* **117** 71 (1995)
3. C Ludwig, W Frey, M Woerner and T Elsaesser, *Opt. Commun.* **102** 447 (1993)
4. R Laenen, K Wolfrum and A Laubereau, *Proc. SPIE* **2138** 41 (1994)
5. R Laenen, K Wolfrum, A Seilmeier and A Laubereau, *J. Opt. Soc. Am. B* **10** 2151 (1993)
6. M Cavallari, G.M Gale, F Hache, L.I Pavlov and E Rousseau, *Opt. Commun.* **114** 329 (1995)
7. G.R Holtom, R.A Crowell and X.S Xie, *J. Opt. Soc. Am. B* **12** 1723 (1995)
8. T.M Jedju, L Rothberg and A Labrie, *Opt. Lett.* **13** 961 (1988)
9. U Simon and F.K Tittel, *Infrared Phys. Tech.* **36** 427 (1995)
10. L Goldberg, W.K Burns and R.W McElhanon, *Opt. Lett.* **20** 1280 (1995)
11. A.H Kung, *Opt. Lett.* **20** 1107 (1995)
12. S.K Wong, R Oliver, K.L Schelper and D.L Fenimore, *Opt. Lett.* **19** 1433 (1994)
13. A.H Kung, *Appl. Phys. Lett.* **65** 1802 (1994)
14. C McGowan, D.T Reid, Z.E Penman, M Ebrahimzadeh, W. Sibbett and D.H Jundt, *J. Opt. Soc. Am. B* **15** 694 (1998)
15. D. T. Reid, M. Ebrahimzadeh and W. Sibbett, *Opt. Lett.* **20**, 55 (1995)
16. Z.W Hu, P.A Thomas, J Webjörn and G.M Loiacono, *J. Appl. Phys. D* **29** 1681 (1996)

17. H Karlsson, F Laurell, P Henriksson and G Arvidson, *Electron. Lett.* **32** 556 (1996)

18. H Karlsson, F Laurell, P Henriksson and G Arvidson, *Electron. Lett.* **32** 556 (1996)

19. Q Chen and W.P Risk, *Elecrton. Lett.* **30** 1516 (1994)

20. J Han, Y Liu, M Wang and D Nie, *J. of Crystal Growth* **128** 864 (1993)

21. D.L Fenimore, K.L Schelper, D Zelmon and S Kück, *J. Opt. Soc. Am. B* **9** 1935 (1996)

22. D.L Fenimore, K.L Schelper, D Zelmon and S Kück, *J. Opt. Soc. Am. B* **9** 1935 (1996)

23. L.K Cheng, L.T Cheng, J Galperin, P.A Morris Hotsenpiller and J.D Beirlein, *J. of Crystal Growth* **137** 107 (1994)

24. P. E. Powers, C. L. Tang and L. K. Cheng, *Opt. Lett.* **19**, 1439 (1994)

25. D. T. Reid, M. Ebrahimzadeh and W. Sibbett, *Opt. Lett.* **20**, 55 (1995)

26. D. T. Reid, C. McGowan, W. Sleat, M. Ebrahimzadeh and W. Sibbett, *Opt. Lett.* **22**, 525 (1997)

27. D. T. Reid, C. McGowan, M. Ebrahimzadeh and W. Sibbett, *IEEE J. Quantum. Electron.* **33**, 1, (1997)

28. C McGowan, D.T Reid, Z.E Penman, M Ebrahimzadeh, W. Sibbett and D.H Jundt, *J. Opt. Soc. Am. B* **15** 694 (1998)

29. Z.E Penman, P Loza-Alvarez, D.T Reid, M Ebrahimzadeh, W Sibbett and D.H Jundt, *Opt. Commun.* **146** 147 (1998)

30. S. D. Butterworth, P. G. R. Smith and D. C. Hanna, *Opt. Lett.* **22**, 618 (1997)

31. H. Karlsson, F. Laurell, P. Henriksson and G. Arvidsson, *Electron. Lett.* **32**, 556

(1996)

32. H Karlsson, Institute of Optical Research, Royal Institute of Technology, Lindstedtsv←gen 24, 100 44 Stockholm, Sweden.

33. D. T. Reid, M. Ebrahimzadeh and W. Sibbett, *Opt. Lett.* **20**, 55 (1995)

34. D.L Fenimore, K.L Schelper, D Zelmon and S Kück, *J. Opt. Soc. Am. B* **9** 1935 (1996)

35. D. T. Reid, C. McGowan, M. Ebrahimzadeh and W. Sibbett, *IEEE J. Quantum. Electron.* **33**, 1, (1997)

36. D.T Reid, Z.E Penman, M Ebrahimzadeh, W Sibbett, H Karlsson and F Laurell, *Opt. Lett.* **22** 1397 (1997)

37. G.T Kennedy, R.S Grant, W.E Sleat and W Sibbett, *Opt. Lett.* **14** 208 (1993)

38. G.J Valentine and W Sibbett, *Digest of Conference on Lasers and Electro-Optics* (Optical Society of America, Washington D.C. 1998) paper CTuM47

39. P Loza-Alvarez, D.T Reid, M Ebrahimzadeh, W Sibbett, H. Karlsson, P. Henriksson, G. Arvidsson and F. Laurell, *Appl. Phys. B.* (submitted)

40. C McGowan, D.T Reid, Z.E Penman, M Ebrahimzadeh, W. Sibbett and D.H Jundt, *J. Opt. Soc. Am. B* **15** 694 (1998)

CHAPTER 5

Mid-infrared Femtosecond Optical Parametric Oscillator Based on Periodically-poled Lithium Niobate

---

The amount of research into frequency-conversion techniques using periodically-poled lithium niobate (PPLN) as the nonlinear crystal has increased dramatically recently, and there are a number of reasons for this. The adaptability of quasi-phasematching (QPM) has meant that periodically-poled materials have been responsible for a huge improvement in the performance of OPOs in generating wavelengths in the mid-infrared region of the spectrum. The large nonlinearity and broad transparency range available from PPLN has allowed it to become the most popular crystal choice for an ever increasing range of applications. Poling techniques have improved sufficiently that high quality crystals are now commercially available and are currently being used extensively in all nonlinear frequency conversion processes. In this chapter the operation of an all-solid-state Ti:sapphire laser pumped femtosecond optical parametric oscillator based on periodically-poled lithium niobate is described. Some of the optical properties of $LiNbO_3$ and PPLN are explained in the following sections by way of an introduction to the PPLN-based OPO. The phasematching properties of PPLN in the OPO arrangement considered here are discussed and the pump laser and OPO configurations are described. The results presented characterise the output from the OPO and are discussed in relation to related work in this area.

Optical Properties of Lithium Niobate and Periodically-Poled Lithium Niobate

$LiNbO_3$ is a negative uniaxial crystal belonging to the crystallographic point group $3m$ and with space group $R3c$[1]. The crystal is composed of distorted oxygen octahedra that are slightly rotated, stacked one above the other, and with one face in common[2]. The oxygen ions are arranged in a hexagonally close-packed arrangement, in planes perpendicular to the crystal z-axis. The planes are separated by lithium and niobium ions in the sequence Nb, vacancy, Li, Nb, vacancy, Li, ... along the crystallographic c-axis. A simplification of the crystal structure of $LiNbO_3$ is shown in Figure 1.

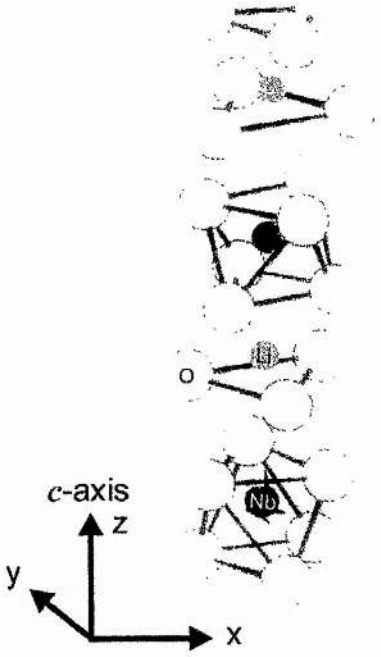

Figure 1: A simplified diagram of the crystal structure of lithium niobate.

$LiNbO_3$ is ferroelectric and this was first reported in 1949 by Matthais and Remeika[3]. This property occurs because of the particular crystallographic structure

of $LiNbO_3$ and is related to the electric field polarisation within the material. In order to be ferroelectric a crystal must have a noncentrosymmetric structure, and it is this structure that determines the nonlinear optical properties of the material. Ferroelectric crystal structures can have the highest degree of non-symmetry.

As was explained in Chapter 4 for RTA, a ferroelectric is a material that possesses a domain structure where the permanent spontaneous electric field of the domain can be reversed under the influence of an externally applied electric field. The internal potential electric field that is present within a crystalline structure means that each ion can take up more than one equilibrium position. The polarity of a ferroelectric domain in $LiNbO_3$, is determined by the displacement of the metal ions from the oxygen layers. Inversion of the poling direction in lithium niobate results if the lithium ions can be induced to move through the triangular plane of the oxygen ions[4]. Periodic-poling involves applying an electric field to a material to periodically alternate the polarity of neighbouring domains within the crystal. This is only possible in a ferroelectric medium. An illustration of the possible positions of the lithium and niobium ions relative to the planes of oxygen ions, for the different polarities, is given in Figure 2. The width of each domain is half the grating period, Λ, which was defined in Chapter 2.

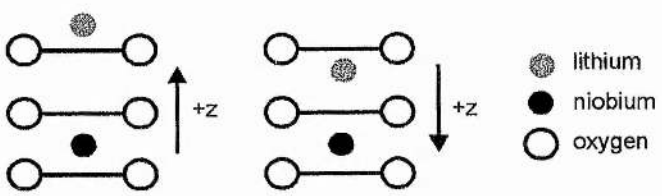

Figure 2: The position of the lithium and niobium ions relative to the planes of the oxygen ions, for the two different domain polarities in PPLN.

The main optical properties of $LiNbO_3$ that are relevant to the context of this work are refractive index, transparency and optical nonlinearity. The temperature of the PPLN crystal used in the OPO described later in this chapter was maintained at 100 °C. A graph of the variation of the extraordinary refractive index with wavelength for a $LiNbO_3$ crystal temperature of 100 °C is shown in Figure 3. This is based on the results of Jundt[5], which do not include results for the ordinary wave. The variation of the ordinary refractive index with wavelength for $LiNbO_3$ can be found in a paper by Edwards and Lawrence[6].

The Sellmeier coefficients, which are used to calculate the refractive index for $LiNbO_3$ are given in Table 1, and are related by:

$$n(\lambda) = \sqrt{a_1 + b_1 f + \frac{a_2 + b_2 f}{\lambda^2 - (a_3 + b_3 f)} + \frac{a_4 + b_4 f}{\lambda^2 - a_5} - a_6 \lambda^2} \quad . \tag{5.1}$$

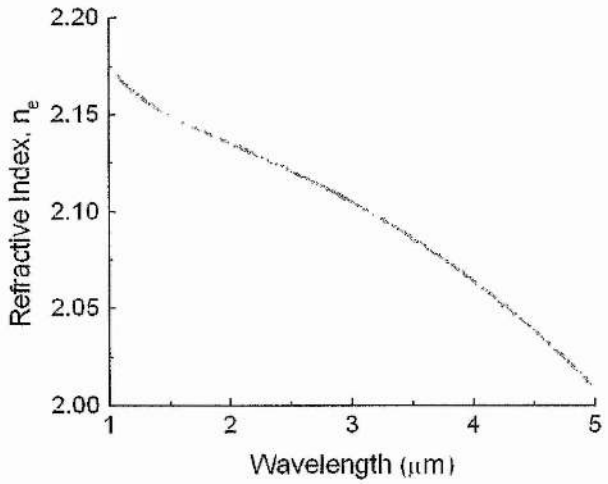

Figure 3: Variation of the extraordinary refractive index with wavelength in $LiNbO_3$, for a crystal temperature of 100 °C.

The temperature parameter, f, is the square of the absolute temperature in degrees Kelvin with an added offset to make f vanish at the reference temperature of 24.5 °C. For a crystal temperature T in degrees Celsius, f is given by:

$$f = (T - 24.5)(T + 570.82).$$

Sellmeier Coefficient	Value
a_1	5.35583
a_2	0.100473
a_3	0.20692
a_4	100
a_5	11.34927
a_6	1.5334×10^{-2}
b_1	4.629×10^{-7}
b_2	3.862×10^{-8}
b_3	-0.89×10^{-8}
b_4	2.657×10^{-5}

Table 1: Sellmeier coefficients for $LiNbO_3$, which can be substituted into Equation (5.1) to calculate n_e.

Refractive index also determines the degree of temporal walk-away[7] between the interacting pulses in an OPO. This can be significant in ultrashort-pulse OPOs because the shorter the pulses, the more detrimental is the effect of walk-away. If the pulses are very short, they only have to walk-away from one another for a very short time, before they are no longer overlapped. Once this happens the interaction ceases and no further gain is seen. The performance of the OPO is thus reduced.

In a $LiNbO_3$ crystal, the amount of walk-away between the pump, signal and idler waves, when all have extraordinary polarisations, can be calculated from Equation (2.11). The walk-away between the pump & signal, pump & idler and signal & idler is

measured in fs/mm, for a crystal temperature of 100 °C[8]. A graph of these results, for a varying signal wavelength, is shown in Figure 4. Varying the crystal temperature has little effect on the amount of walk-away between the interacting waves.

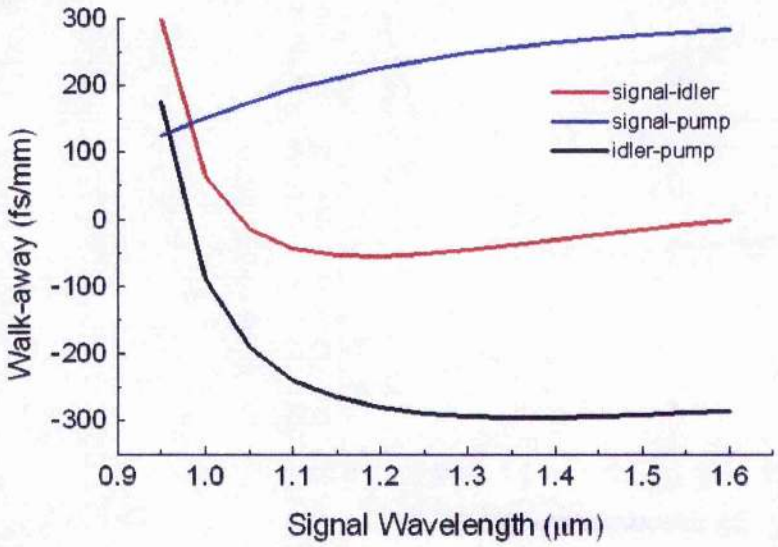

Figure 4. Walk-away in $LiNbO_3$ plotted against signal wavelength.

$LiNbO_3$ has a relatively large transparency range, extending from ~0.33 μm to ~5.5 μm, and is thus suitable for generating mid-infrared wavelengths. A graph of the transmission of $LiNbO_3$ is given in Figure 5. This is from the work of Myers et al[9]. An e-wave has a substantially higher transmission than an o-wave over the range of wavelengths of interest in optical parametric generation and does not suffer absorption at 2.9 μm. These are further advantages of using three e-waves in optical parametric oscillation using $LiNbO_3$.

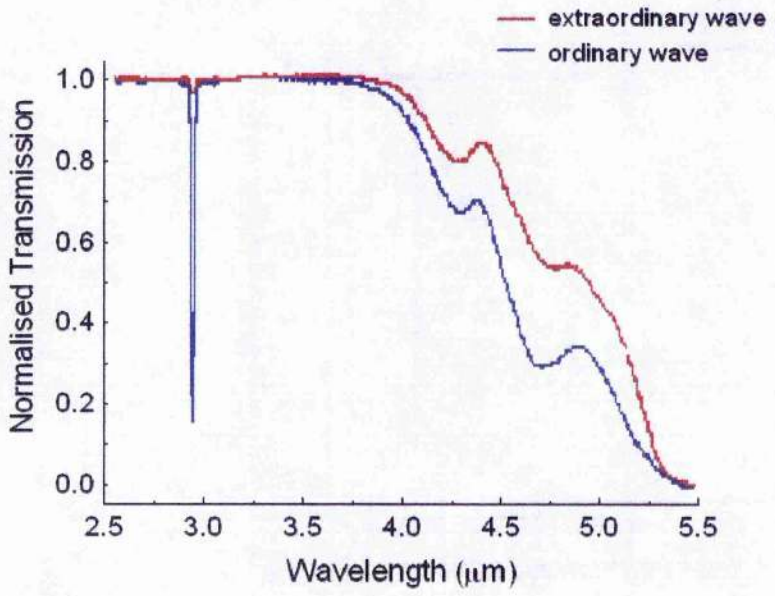

Figure 5: Transmission of $LiNbO_3$ in the mid-infrared, for an e-wave and an o-wave.

The optical nonlinearity for $LiNbO_3$[10] is found from the nonlinear optical tensor, d_{ij}, which is given by

$$d_{ij} = \begin{bmatrix} 0 & 0 & 0 & 0 & d_{31} & -d_{22} \\ -d_{22} & d_{22} & 0 & d_{31} & 0 & 0 \\ d_{31} & d_{31} & d_{33} & 0 & 0 & 0 \end{bmatrix}.$$

In $LiNbO_3$ there are only three non-zero nonlinear coefficients, namely d_{22}, d_{31} and d_{33}. The most up-to-date values for these coefficients are d_{22}=2.1 pm/V, d_{31}=4.3 pm/V and d_{33}=27 pm/V from a paper by Myers et al[11].

The efficiency of a nonlinear optical interaction is proportional to the square of the effective nonlinear coefficient, d_{eff}, hence d_{eff} should be as large as possible. d_{eff} is related to the d_{ij} coefficients by equations that depend on the type of interaction and the type of crystal used[12]. The d_{33} coefficient in $LiNbO_3$ is significantly larger than

d_{22} or d_{31}, but cannot be accessed using standard birefringent phasematching techniques.

When quasi-phasematching is employed, the interaction of any combination of polarisations along any direction in the crystal is permitted. In PPLN, the poling direction is chosen so that when all the interacting waves are e-waves, the largest nonlinear coefficient d_{33} is accessed. The effective nonlinearity of a material is found from

$$d_{eff} = \frac{2}{m\pi} d_{33}$$

and m=1,3,5, ... is the order of the phasematched process. First order processes, with m=1, are the most efficient. The effective optical nonlinearity in PPLN is about 17 pm/V and this is approximately four times larger than the maximum d_{eff} available from a birefringently phasematched $LiNbO_3$ crystal.

Photorefractive Damage

The photorefractive effect[13,14] is a change in the refractive index of a material caused by the incidence of light upon it. Materials that are particularly susceptible to this effect are called photorefractive materials. In a photorefractive material, the incidence of a visible wavelength beam of light (as shorter light wavelengths correspond to higher photon energies) can be sufficient to cause photoionisation, which results in the production of free charge carriers within the material. The rate of production of these free charge carriers is proportional to the intensity of the incident light beam. The free charge carriers scatter through the material towards areas of

lower light intensity causing a variation in the electric field across the material. It is this electric field disruption which causes localised changes in the material refractive index, which move throughout the material as the free charge carriers scatter. This effect is present to some extent in all ferroelectric materials, although it only becomes significant during the application and generation of visible light wavelengths.

It has been known for many years that $LiNbO_3$ is susceptible to photorefractive damage[15] and that the effect is most significant at wavelengths from 400 nm to 700 nm[16]. It was hoped that the problem would be less evident in PPLN. In fact, there have been reports of frequency-doubling experiments where photorefractive damage was not observed. However, in OPOs based on PPLN[17,18] photorefractive damage has been observed as a constantly-shifting break up of the oscillating beam. As far as this work is concerned, PPLN does suffer from the effects of photorefractive damage and the result of this is that transmission of high optical powers at visible wavelengths alters the refractive index of the material and seriously degrades the optical performance. This was overcome to a certain extent by heating the crystal to temperatures of around 100 °C[19,20].

Thermal Expansion

At high temperatures the crystal expands along the direction of propagation of the incident wave. The thermal expansion coefficients α and β describe the crystal length, l_T, at a temperature, T, normalised to the length of the crystal at 25 °C.

$$l_T = l_{25}\left[1+\alpha(T-25)+\beta(T-25)^2\right],$$

where α=1.54×10^{-5} K^{-1} and β=5.3×10^{-9} K^{-2}. PPLN is poled along the z-axis so, in a similar way, the grating period also increases such that

$$\Lambda_T = \Lambda_{25}\left[1+\alpha(T-25)+\beta(T-25)^2\right],$$

where Λ_{25} is the grating period for a crystal at 25 °C and Λ_T is the grating period for a crystal temperature T. This equation was derived by Kim and Smith[21] who also provided the values for α and β.

Phasematching in PPLN

The purpose of the experiment described in this chapter was to construct an all-solid-state femtosecond OPO based on PPLN and establish whether the tuning range already measured[22], could be further extended. In order to establish the most appropriate choice of pump wavelength, grating period and oscillation wavelength for this to be possible, some theoretical modelling was used to generate the phasematching curve shown in Figure 6.

The solution to the phasematching equation for PPLN defines a range of wavelengths for which momentum and energy conservation are achieved and optical parametric generation is possible. The variation of gain across this wavelength range has a sinc^2 dependence, and because the gain bandwidth is so large in PPLN, optical parametric oscillation is still possible even for wavelengths where $\Delta k \neq 0$ but has a value close to zero.

Theoretical modelling of the wavelengths that were phasematchable from the OPO was carried out. For the range of wavelengths available from the Ti:sapphire laser i.e. 780 nm to 860 nm, the phasematching curve for PPLN at 100 °C and a grating period of 21.14 μm, was calculated and is shown in Figure 6. This plot is generated from the Sellmeier equations already given and includes the $sinc^2$ variation of the gain bandwidth (from Equation (2.8)). The areas shown in black on the plot have the highest gain.

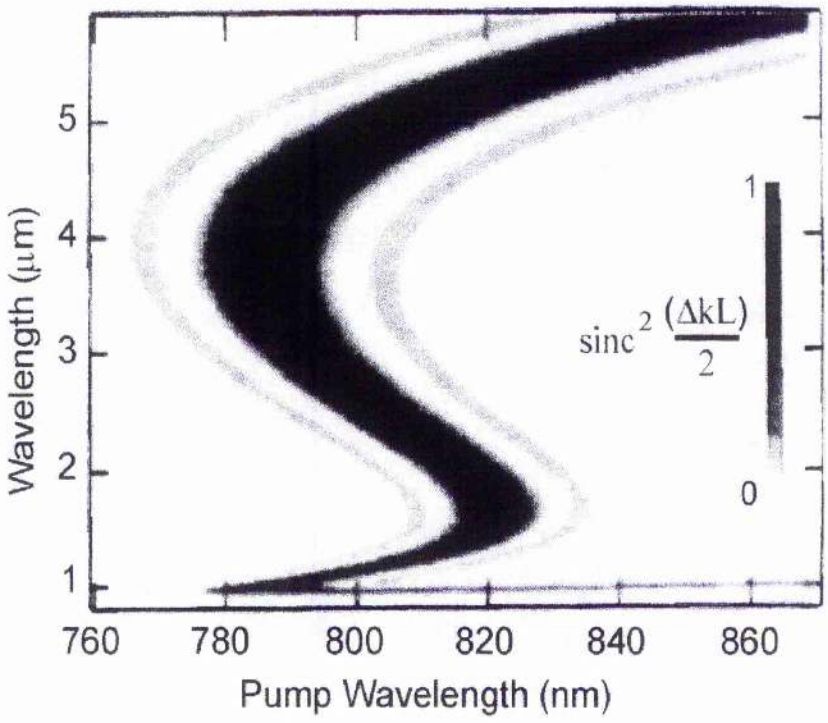

Figure 6: Phasematching curve for $LiNbO_3$ over the range of wavelengths available from the pump laser. The $sinc^2$ variation of gain with the highest areas of gain shown in black.

The phasematching curve and the variation of the gain bandwidth across the tuning range which it defines, were used to predict the behaviour of the output from the PPLN-based OPO. It suggested that a long pump wavelength, a short crystal grating

and a short signal wavelength would provide the best chance of generating idler wavelength in the 5 μm region.

The PPLN-Based Optical Parametric Oscillator

Until recently, Ti:sapphire laser pumped femtosecond optical parametric oscillators were based on birefringently phasematched nonlinear materials and an argon-ion laser as the input pump source. For access to mid-infrared wavelength regions beyond ~3 μm, $KTiOPO_4$ and its arsenate isomorphs or $KNbO_3$ have been the primary material candidates because of their broad infrared transparency ranges and relatively large nonlinearities [23-26]. However, a lack of noncritical geometry in these materials for mid-infrared phasematching has necessitated the use of noncollinear pumping schemes with disadvantages associated with spatial walk-off and a consequent reduction in gain. The use of quasi-phasematching in materials which can be periodically-poled permits collinear noncritical propagation of all waves along a crystal axis, thus overcoming the restrictions of critical noncollinear phasematching. The technique of periodic poling causes a periodic reversal of the polarity of the nonlinear coefficient in the material. The period of this domain inversion, or grating, can be chosen to provide phasematching for any $\chi^{(2)}$ frequency conversion process within the transparency range of the material. Through an appropriate choice of wave polarisations and propagation direction through the crystal, the quasi-phasematching technique also allows access to significantly larger nonlinear coefficients than those available under birefringent phasematching. In PPLN, the grating is arranged such that with all waves polarised parallel to the piezoelectric Z-axis (extraordinary

waves), the largest nonlinear coefficient, d_{33}, is accessed. These characteristics in PPLN have been exploited to develop a collinearly pumped all-solid-state femtosecond OPO capable of producing useful output powers and wide tunability in the mid-infrared.

The Pump Laser

The PPLN OPO was synchronously pumped by an all-solid-state-pumped self-modelocked Ti:sapphire laser, which is shown schematically in Figure 7. The Ti:sapphire laser was pumped using a Spectra-Physics Millennia laser (diode-pumped frequency-doubled Nd:YVO_4 laser). The Millennia is an all-solid-state, high power, visible cw laser that provides up to 5 W of green light at 532 nm. The vertically polarised light from the Millennia laser had to be rotated so as to enter the Ti:sapphire crystal as π-polarised light. This was achieved using a multiple-order half-wave plate designed for use at 532 nm.

The pump beam was focussed into the Ti:sapphire crystal using a broadband visible antireflection coated lens with a focal length of 100 mm. The two curved Ti:sapphire cavity mirrors had radii of curvature of –100 mm. M4 was a plane mirror and M3 was an output coupler. Each mirror was broadband high reflectivity coated from 700 to 850 nm. The Ti:sapphire crystal (Crystal Systems) was Brewster-cut and 10 mm in length with an absorption coefficient of 2.3 cm^{-1}. The rod was cooled using low-pressure water and a Peltier-effect cooler was used to maintain it at a constant temperature of 15 °C.

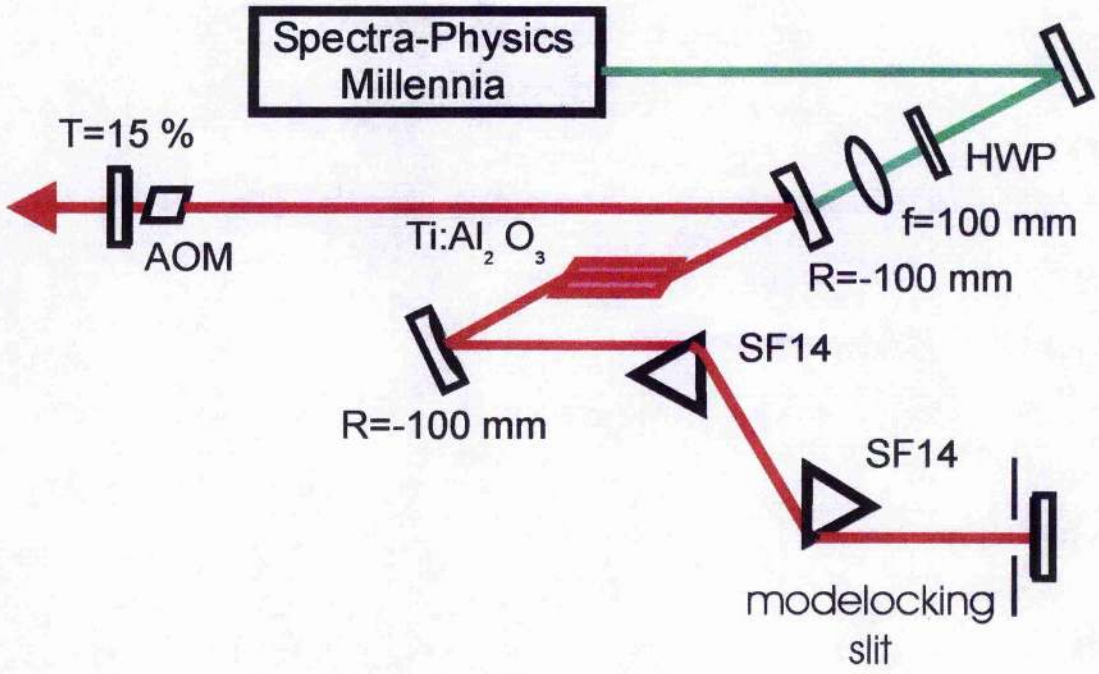

Figure 7: All-solid-state Ti:sapphire laser cavity configuration.

To facilitate modelocking an acousto-optic modulator (AOM) was positioned close to the output-coupling mirror M1. Once modelocked, any drifts in the cavity length led to a mismatch between the modulator drive frequency and the cavity repetition frequency. This produced instabilities in the output of the laser. To overcome the problem, the modulator drive signal was derived from a fast photodiode, which monitored the laser output. The acousto-optic modulator consisted of a Brewster-angled quartz slab (Brimrose Corporation) and was driven by focusing a weak reflection from one on the prisms on to a fast photodiode (type BPX65). The output of the photodiode was filtered using a 172 MHz band-pass filter with a bandwidth of approximately 10 MHz. This second harmonic component was amplified using a hybrid RF amplifier (Phillips OM335) and applied to the output of an integrated

"divide by four" circuit producing an output of 43 MHz. This signal was filtered and then amplified before being applied to the acousto-optic modulator. The typical power in the modulator drive signal was around 500 mW. When the laser oscillated, the mode-beating of the output was sufficient to drive the modelocker electronics.

An aperture was inserted close to the highly reflecting mirror. Narrowing this vertical slit favoured modelocked operation as the beam is more tightly focussed at this point in the cavity when the laser is modelocked.

Group velocity dispersion was significant in the cavity due to the Ti:sapphire rod and the acousto-optic modulator. To compensate for this negative dispersion was introduced into the cavity via two SF14 prisms. At an apex separation of 32 cm, the net cavity GVD was approximately zero. A prism separation of > 32 cm was required for a net negative GVD. With careful and accurate optimisation of the cavity alignment, the laser could be made to self-modelock, producing pulses with durations of the order of 100 fs, at output powers of 800 mW to 900 mW and at a repetition rate of ~86 MHz. The output wavelength of this laser was tuned to 840 nm, close to the long wavelength limit of the mirror set, because a long pump wavelength was required to generate the longest possible idler wavelengths from the PPLN-based OPO. Under these conditions modelocked operation could be sustained for several hours in the absence of any external vibrations perturbing the system. Typical interferometric autocorrelation and spectral measurements from this laser system are presented in Figure 8. The interferometric autocorrelation was recorded using a

standard SHG-autocorrelator system, which incorporated a BBO doubling crystal and the optical spectrum was recorded using a Rees Instruments laser spectrum analyser.

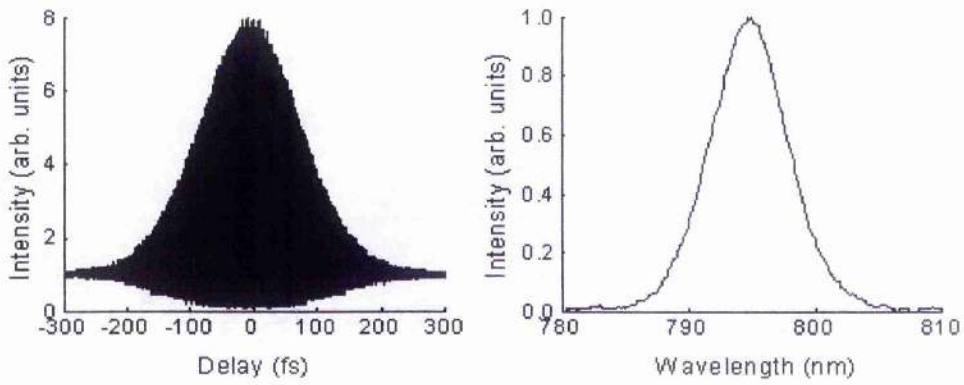

Figure 8: Typical autocorrelation and spectral measurements from the all-solid-state femtosecond Ti:sapphire laser.

The PPLN OPO Experiment and Results

The PPLN crystal used in the work described here was prepared by Crystal Technology[28], from a 15 mm long × 0.5 mm thick sample of congruent $LiNbO_3$, by patterning photoresist gratings, with periods of 20.5 μm to 22.0 μm, onto the +z face. These gratings were chosen to maximise the range of wavelengths available from the PPLN-OPO when pumped with a Ti:sapphire laser emitting wavelengths from 780 nm to 860 nm. Electrical contact with the crystal was made using LiCl electrolyte, and the crystal was poled using an applied voltage of ~25 kV for a duration of ~50 ms[29]. (When the poling voltage is abruptly turned off, the domains can return to their original polarity. This can be avoided if the electric field is applied at half the coercive field value for a further 50 ms after poling.). The resulting PPLN crystal was

cut to dimensions of 11 mm × 0.5 mm × 1 mm in length with the eight gratings evenly spaced along the longest side. A crystal length of 1 mm was sufficient for optical parametric oscillation to be possible in the limit of the temporal walk-away of the interacting pulses. A longer crystal would simply have contributed to the intracavity GDV experienced by the oscillating pulse. The only grating used in the experiment was 20.5 μm to allow generation of the longest possible idler wavelengths available from the OPO. The crystal was anti-reflection (AR) coated at 1.1 μm on both faces and the crystal temperature was maintained at 100 °C and this was sufficient to avoid the effects of photorefractive damage. This was achieved by mounting the PPLN crystal in an oven, which was mounted on an x, y, z -translation stage to provide an accurate means of aligning the crystal.

The heating element in the oven consisted of a 150 Ω resistor, which was enclosed in a copper block, providing a good thermal contact. The PPLN crystal was held in contact with the other side of the copper block using a spring-loaded arm, which accommodated thermal expansion of the crystal.

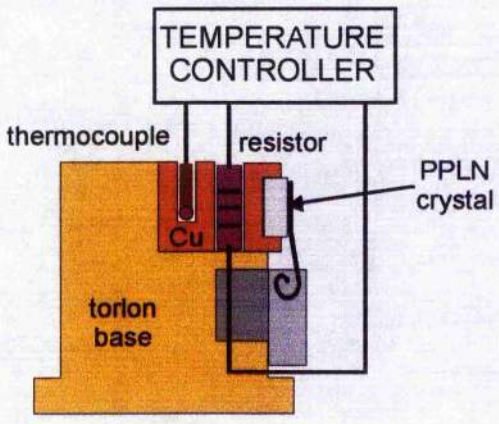

Figure 9: Diagram of the PPLN crystal mounted in an oven to maintain the crystal temperature at 100 °C.

The oven was enclosed in a block of torlon to provide enhanced thermal insulation. A Marlow Industries temperature controller[30] was used as a power supply for the heating element, and to monitor the crystal temperature via a thermocouple, which was also inserted into the copper block. A current of 0.16 A was sufficient to heat the resistor and thus the crystal to 100 °C. The slight temperature gradient across the crystal was not sufficient to impair the performance of the OPO.

It was necessary to include an optical isolator between the pump laser and the OPO to prevent feedback from the OPO disrupting the modelocking process in the Ti:sapphire laser. The loss of pump power on transit through the isolator was ~2 % and so was not significant. A half-wave plate was used to ensure the horizontal polarisation state of the pump required for the e→e+e interaction and the polarisations of the pump, signal and idler waves were horizontal in the cavity and were parallel to the poling direction.

As shown in Figure 10, the OPO was configured in a three mirror V-cavity. The pump beam was focussed into the PPLN crystal using a 50 mm focal length lens. The radius of curvature of each concave focusing mirror was -100 mm. The cavity mirrors included a high reflectivity mirror at 1.064 μm on a BK7 substrate (M1). The second mirror was high reflectivity coated at 1.1 μm on a CaF_2 substrate (M2), which is transparent to beyond 5 μm, thereby allowing extraction of the idler. M3 was either a high reflector or an output coupler with a coating centred at 1.064 μm. The OPO cavity was length matched to the Ti:sapphire laser cavity to achieve oscillation by synchronous pumping.

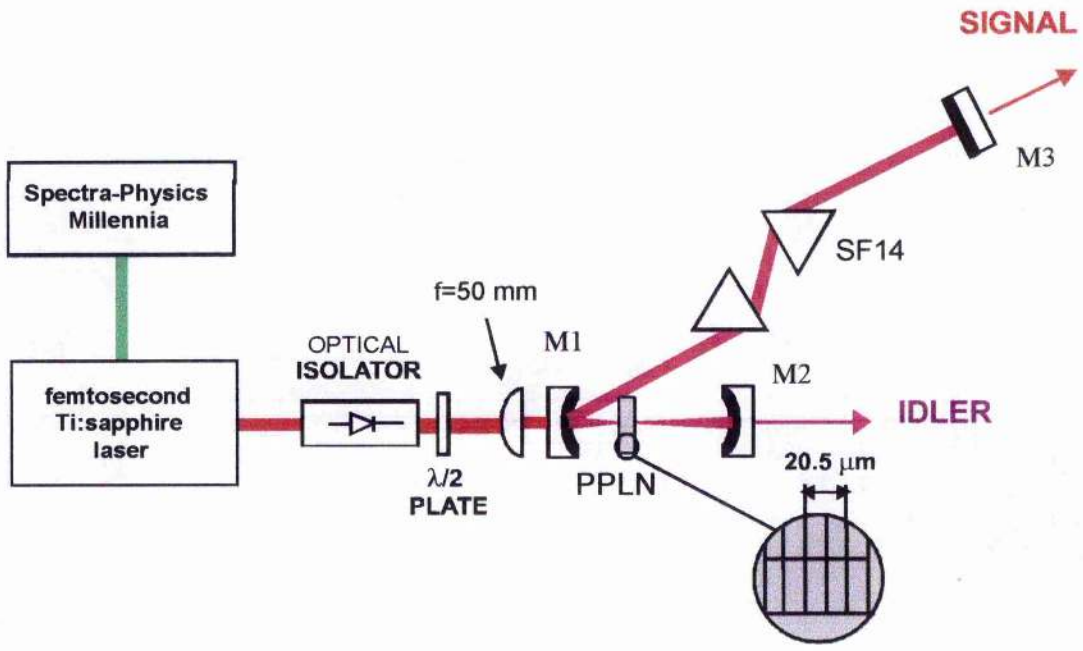

Figure 10: OPO cavity configuration showing collinear phasematching geometry. Inset illustrates the crystal grating and period.

The intracavity dispersion compensation was achieved by including a pair of SF14 prisms, with an apex separation of 45 cm, in the cavity. Temporal analysis of the signal pulses was carried out using a GaAs LED (E_g=980 nm)[31] as the detector, and an interferometric autocorrelation and spectrum of the signal pulses generated around 1.0 μm is shown in Figure 11. The pulse duration determined from the interferometric autocorrelation profile is 210 fs which, when combined with the spectral data, implies a duration-bandwidth product of $\Delta\tau\Delta\nu$=0.41, assuming a sech^2 pulse shape. The shortest signal wavelength attained was 996 nm but at this wavelength the OPO was unstable and measurements could not be taken. This signal wavelength, combined with the pump wavelength, which was known to be 840 nm, confirmed that idler wavelengths of 5.36 μm were generated from this PPLN-based OPO. The short

wavelength limit of the system was due to the lower bandwidth limit of the CaF_2 mirror coating, which extended from 996 nm to 1.22 μm.

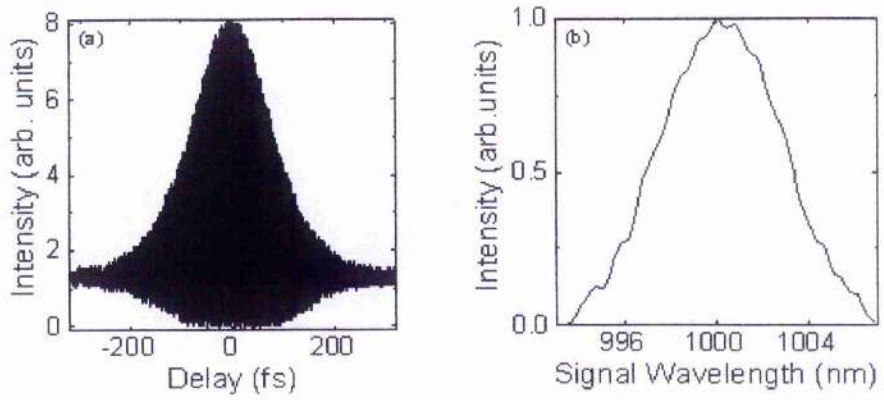

Figure 11: (a) Interferometric autocorrelation of the signal implying pulses of 210 fs duration.

(b) Corresponding signal spectrum centred at 1.0 μm.

For this particular choice of grating period and mirror set, varying the cavity length of the PPLN OPO provided a tuning range that extended from 996 nm to 1.22 μm for the signal and 2.6 μm to 4.98 μm for the idler. An extended-sensitivity InGaAs photodetector[32] was used to record interferometric autocorrelations of the idler at 4.45 μm and 4.88 μm. Autocorrelation profiles presented in Figure 12 imply pulse durations of 200 fs and 190 fs, respectively. Typical spectra were also recorded at wavelengths of 4.18 μm and 4.45 μm and are shown in Figure 13. At 4.45 μm the pulse duration and spectrum implied a duration-bandwidth product of $\Delta\tau\Delta\nu$=0.42, assuming a $sech^2$ pulse shape. The monochromator grating cut-off was 4.5 μm so spectra beyond this limit could not be measured.

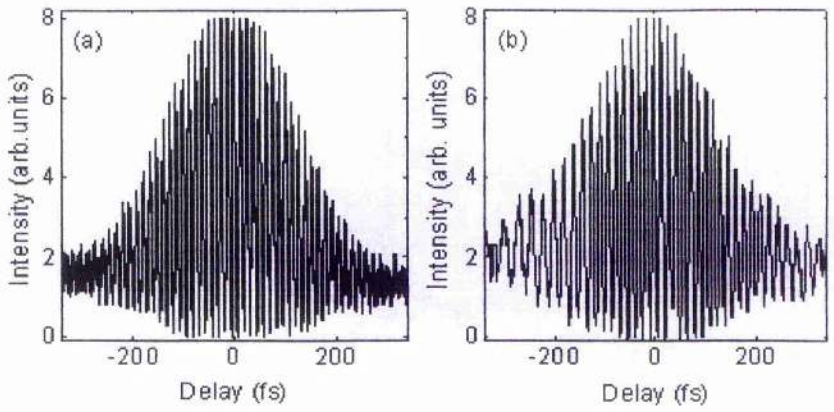

Figure 12: Typical interferometric autocorrelations of the idler at (a) 4.45 μm and (b) 4.88 μm. Pulse durations inferred from the autocorrelation profile are 200 fs and 190 fs respectively.

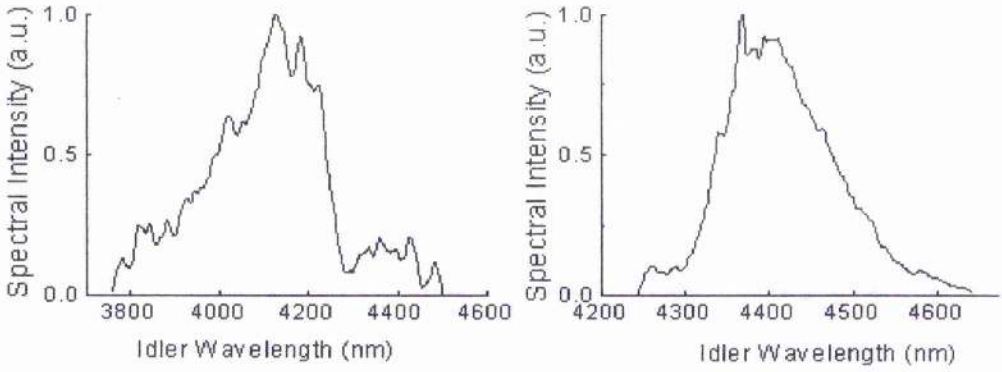

Figure 13: Typical idler spectra centred at (a) 4.18 μm and (b) 4.45 μm.

With intracavity dispersion compensation the maximum idler output power was 106 mW at 2.6 μm, measured after M2, when all the cavity mirrors were highly reflecting. At 4.88 μm, 25 mW of average power was measured. These values are not corrected for the loss incurred on transmission through the CaF_2 mirror M2 which we believe to be ~25 %. A maximum signal output power of 240 mW was measured at 1.16 μm using a 15 % output coupler. The pump threshold was measured as 480 mW for this amount of output coupling. Simultaneous measurements of signal and idler

powers of 203 mW and 106 mW, respectively, are as expected from the ratio of photon energies in an ideal low-loss system. These results indicate an overall conversion efficiency to useable signal and idler in excess of 35 %. The slope efficiency for the signal was measured to be 46 % for a pump wavelength of 830 nm and a signal wavelength of 1.04 μm and the slope efficiency for the signal was measured to be 70 % for a pump wavelength of 800 nm and a signal wavelength of 1.1 μm. These values were determined from measurements of signal output power made for a range of pump powers and these are shown in Figure 14.

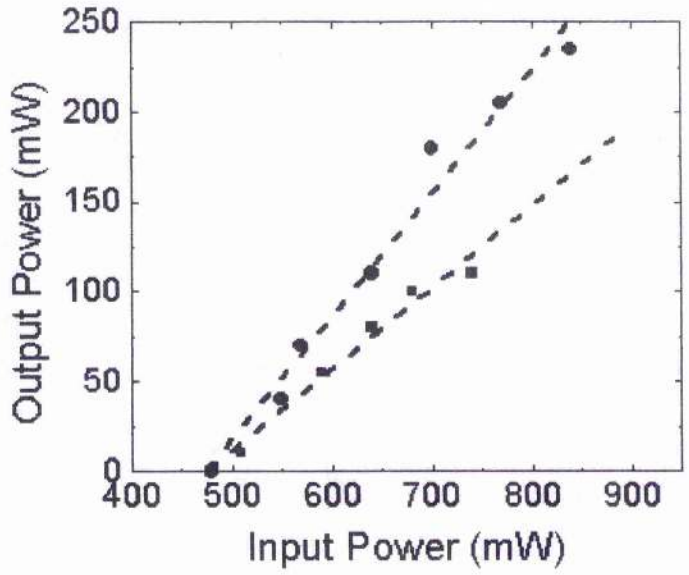

Figure 14: Variation in average signal output power with pump power for pump and signal wavelengths of 830 nm and 1.04 μm (circles) and pump and signal wavelengths of 800 nm and 1.1 μm (squares): (---), a linear fit of the experimental data which was used to determine the slope efficiencies of 46% and 70% respectively.

Conclusions

The operation of a picosecond OPO based on PPLN has been reported[33]. A femtosecond OPO based on a periodically-poled $RbTiOAsO_4$ (PPRTA)[34] was described in Chapter 4. By using PPRTA as the nonlinear crystal and an argon-ion pumped Ti:sapphire laser as the pump source for the OPO, a tuning range from 1.06 μm to 1.225 μm for the signal and 2.67 μm to 4.5 μm for the idler was obtained. This approach was extended to PPLN, and continuous wavelength coverage from 975 nm to 4.55 μm at moderate output powers[35] was achieved. In this chapter, results were presented which showed that the use of an all-solid-state Ti:sapphire pump source in combination with a PPLN-based OPO represented a robust source of high-repetition-rate femtosecond pulses in the mid-infrared at wavelengths out to ~5 μm. Significantly higher output powers in the signal and idler than previously reported[35] were also measured.

It was previously demonstrated that a continuous tuning range from 975 nm to 4.55 μm in the mid-infrared was available from a PPLN OPO using an argon-ion pumped Ti:sapphire laser[35] as the pump source. Here it has been shown that this tuning range can be readily extended to longer idler wavelengths, of ~5 μm, by employing a suitable mirror set in the OPO. In fact, idler wavelengths as long as 5.36 μm were reached with this system although this could not be measured directly. The use of a crystal which was AR-coated for shorter signal wavelengths combined with a shorter grating period and a longer pump wavelength could undoubtedly see this range extended yet further in accordance with the phasematching condition. It has

been shown that using a collinear geometry pulses of ~200 fs duration at powers of 240 mW for the signal, and 106 mW for the idler can be produced by an OPO based on PPLN. Powers of 25 mW at wavelengths as long as 4.88 μm are also readily available.

More recent work has shown that wavelengths close to 6.3 μm can be generated using a PPLN-based OPO. Hanna et al.[36] attained this wavelength using a picosecond PPLN-OPO, which was synchronously-pumped by a Nd:YLF laser operating at 1.047 μm.

In Chapter 6, a PPLN-based OPO pumped by an all-solid-state Ti:sapphire laser, producing transform-limited pulses of ~15 fs duration, is described. The purpose of this experiment was to reduce the duration of the pulses generated by the PPLN-OPO. A number of other improvements were made to the OPO cavity components to facilitate this.

Chapter 5

References

1. V.G Dmitriev, G.G Gurzadyan and D.N Nikogosyan, Handbook of Nonlinear Optical Crystals (second ed., Springer-Verlag, Belrin, 1997)
2. M Houé and P.D Townsend, *J. Appl. Phys.* **28** 1747 (1995)
3. B.T Matthais and J.P Remeika, *Phys. Rev.* **79** 1886 (1949)
4. M Houé and P.D Townsend, *J. Appl. Phys.* **28** 1747 (1995)
5. D.H Jundt, *Opt. Lett.* **20** 1553 (1997)
6. GJ Edwards and M Lawrence, *Opt. Quantum Electron.* **16** 373 (1984)
7. V.G Dmitriev, G.G Gurzadyan and D.N Nikogosyan, Handbook of Nonlinear Optical Crystals (second ed., Springer-Verlag, Belrin, 1997
8. V.G Dmitriev, G.G Gurzadyan and D.N Nikogosyan, Handbook of Nonlinear Optical Crystals (second ed., Springer-Verlag, Belrin, 1997
9. L.E Myers, R.C Eckardt, M.M Fejer and R.L Byer, W.R Bosenberg and J.W Pierce, J. Opt. Soc. Am. B, 12 2102 (1995)
10. V.G Dmitriev, G.G Gurzadyan and D.N Nikogosyan, Handbook of Nonlinear Optical Crystals (second ed., Springer-Verlag, Belrin, 1997)
11. L.E Myers, R.C Eckardt, M.M Fejer and R.L Byer, W.R Bosenberg and J.W Pierce, *J. Opt. Soc. Am. B*, **12** 2102 (1995)
12. R.W Boyd, Nonlinear Optics (Academic Press, San Diego, 1992) p45
13. E Harris, *Proc. IEEE* **57** 2096 (1969)
14. Ohanian, Physics, (second ed. W.W Norton and Company, New York, 1989)
15. A Ashkin, G.D Boyd, J.M Dziedzic, R.G Smith, A.A Ballman, J.J Levinstein and K Nassan, *Appl. Phys. Lett.* **9** 72 (1966)

16. R.W Boyd, Nonlinear Optics (Academic Press, San Diego, 1992) p411

17. L.E Myers, R.C Eckardt, M.M Fejer, R.L Byer, W.R Bosenberg and J.W Pierce, *J. Opt. Soc. Am. B* **12** 2102 (1995)

18. C McGowan, D.T Reid, Z.E Penman, M Ebrahimzadeh, W. Sibbett and D.H Jundt, *J. Opt. Soc. Am. B* **15** 694 (1998)

19. A Ashkin, G.D Boyd, J.M Dziedzic, R.G Smith, A.A Ballman, J.J Levinstein and K Nassan, *Appl. Phys. Lett.* **9** 72 (1966)

20. L.E Myers, R.C Eckardt, M.M Fejer, R.L Byer, W.R Bosenberg and J.W Pierce, *J. Opt. Soc. Am. B* **12** 2102 (1995)

21. Y.S Kin and R.T Smith, *J. Appl. Phys.* **40** 4637 (1969)

22. C McGowan, D.T Reid, Z.E Penman, M Ebrahimzadeh, W. Sibbett and D.H Jundt, *J. Opt. Soc. Am. B* **15** 694 (1998)

23. G.R Holtom, R.A Crowell and L.K Cheng, *Opt. Lett* **20** 1880 (1995)

24. S.W McCahon, S.A Anson, D.-J Jang and T.F Boggess, *Opt. Lett.* **20** 2309 (1995)

25. D.E Spence, S Weilandy, C.L Tang, C Bosshard and P Gunther, *Appl. Phys. Lett.* **68** 452 (1996)

26. D.T Reid, C McGowan, M Ebrahimzadeh and W Sibbett, *IEEE J. Quantum Electron.* **33** 1 (1997)

27. L.E Myers, R.C Eckardt, M.M Fejer and R.L Byer, *Opt. Lett.* **21** 591 (1996)

28. Crystal Technonlogy Inc., 1040E. Meadow Cir., Palo Alto, CA 94303, USA

29. L.E Myers, R.C Eckardt, M.M Fejer and R.L Byer, W.R Bosenberg and J.W Pierce, *J. Opt. Soc. Am. B*, **12** 2102 (1995)

30. Model SE5020, Marlow Industries, 7 Laura House, Jengers Mead, Billinghurst, West Sussex, RH14 9NZ

31. D.T Reid, M Padgett, C McGowan, W.E Sleat, and W Sibbett, *Opt. Lett.* **22** 233 (1997)

32. D.T Reid, C McGowan, M Ebrahimzadeh and W Sibbett, *IEEE J. Quantum Electron.* **33** 1 (1997)

33. S.D Butterworth, V Pruneri and D.C Hanna, *Opt. Lett.* **21** 1345 (1996)

34. D.T Reid, Z Penman, M Ebrahimzadeh, W Sibbett, H Karlsson and F Laurell, *Opt. Lett.* **22** 1397 (1997)

35. C McGowan, D.T Reid, Z.E Penman, M Ebrahimzadeh, W. Sibbett and D.H Jundt, *J. Opt. Soc. Am. B* **15** 694 (1998)

36. L Lefort, K Peuch, G.W Ross, Y.P Svirko and D.C Hanna, *Appl. Phys. Lett.* **73** 1610 (1998)

CHAPTER 6

Shorter Pulses from the Femtosecond Optical Parametric Oscillator Based On Periodically-poled Lithium Niobate

---

In Chapter 5 the operation and characterisation of an all-solid-state OPO based on PPLN was described. In this chapter a similar PPLN-based OPO, pumped by a sub-20 fs Ti:sapphire laser, is described. Modifications were made to the original OPO cavity components to reduce the intracavity dispersion. The aim of this work was to generate shorter pulses than had been demonstrated previously from our PPLN-based OPO[1,2]. This result was important because shorter pulses in the mid-infrared have a larger associated bandwidth and such a broad-bandwidth source in the mid-infrared is expected to satisfy an extensive range of applications.

Ti:sapphire lasers producing sub- 20 fs pulses have been available for a number of years. To date, these systems have been limited to producing average output powers of a few hundred milliwatts[3,4], because of cooling problems associated with the use of thin crystals (to minimise the intracavity group velocity dispersion) and stability problems resulting from the high intracavity peak powers. A system based on dispersion engineered cavity mirrors and which produces sub-10 fs pulses at peak power levels exceeding 1 MW, has recently been demonstrated[5]. The Ti:sapphire laser used to pump the PPLN-based OPO described in this chapter was capable of producing 13 fs pulses at peak powers in excess of 1 MW and with average output

powers in excess of 1.5 W[6]. This system incorporated a sequence of four prisms to provide dispersion compensation.

The Pump Laser

This sub- 20 fs Ti:sapphire laser was configured as a self-modelocked unidirectional ring cavity[7] providing a number of advantages over the pump sources used previously for the PPLN-based OPO. The symmetric cavity design meant that modelocking could be achieved at the centre of the cavity stability range and this maximised the output power available from the laser. Also, the intracavity dispersion introduced by the crystal was low because the pulse travelled through the crystal only once per round trip of the cavity. A further advantage was that the ring-laser was insensitive to optical feedback and so the loss of pump power incurred by including an optical isolator between the laser and the OPO-cavity was eliminated[8].

The pump source for the Ti:sappire laser was a Spectra-Physics Millennia X (diode-pumped frequency-doubled Nd:YVO_4) laser. The Millennia X provides up to 10 W of power at 532 nm. The vertically polarised light from the Millennia X had to be rotated so as to enter the Ti:sapphire crystal as π-polarised light. This was achieved using a multiple-order half-wave plate designed for use at 532 nm. The cavity layout for the megawatt Ti:sapphire laser is shown schematically in Figure 1.

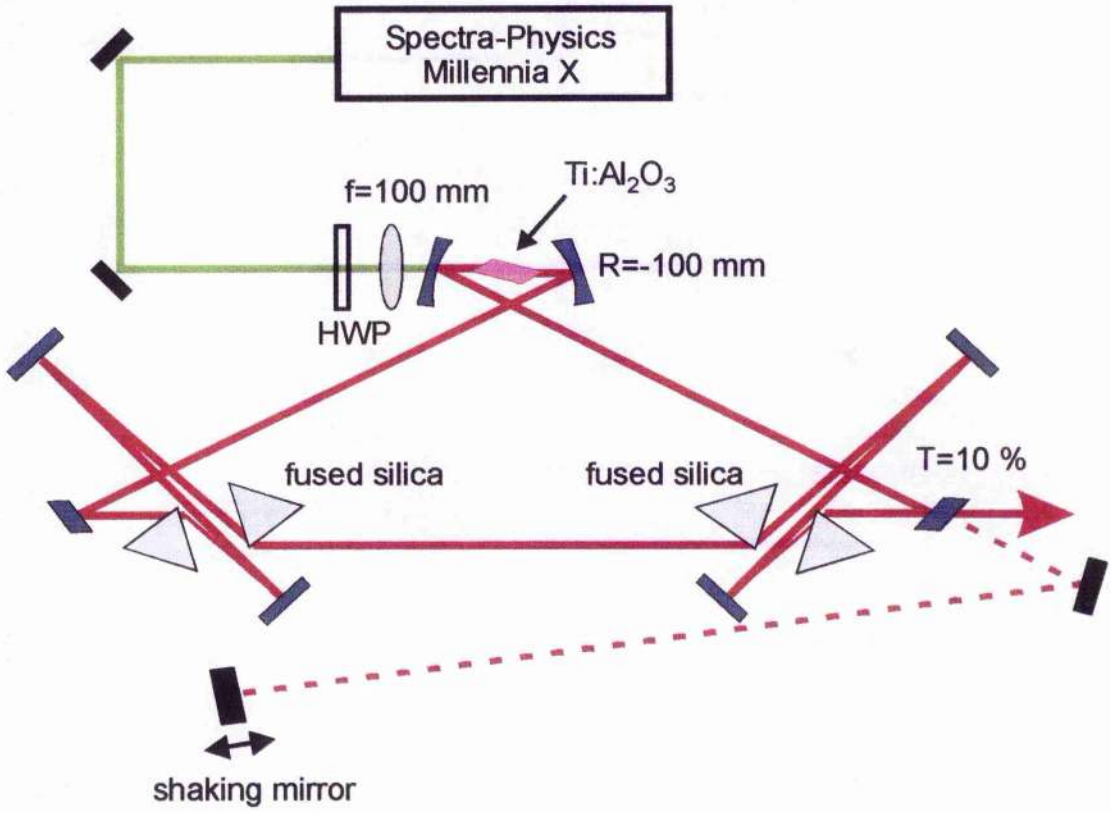

Figure 1: Megawatt Ti:sapphire laser cavity configuration.

The pump beam was focussed into the Ti:sapphire crystal using a broadband visible anti-reflection coated lens with a focal length of 63 mm. The two curved Ti:sapphire cavity mirrors had radii of curvature of –100 mm. With the exception of the output coupler, which was 10% transmitting at 850 nm (LaserOptik, GmbH, Germany), the plane cavity mirrors were all broadband high reflectivity coated from 710 nm to 890 nm (Newport UF.20). The Ti:sapphire crystal was Brewster-cut and 10 mm in length with an absorption coefficient of 2.3 cm^{-1}. The crystal was cooled using low-pressure water and a Peltier-effect cooler was used to maintain it at a constant temperature of 15 °C.

Second and third-order dispersion compensation was provided by two pairs of fused silica prisms (apex angle 69°), each with a separation distance of 590 mm. Extracavity dispersion compensation was also achieved using two pairs of fused silica prisms, each with a separation distance of 350 mm. This was necessary to remove the frequency-chirp acquired by the pulse on transit through the BK7 substrate of the output coupler. The amount of pulse chirp was considerable at this point, as the thickness of the output coupler substrate was effectively 7 mm, due to the angle of the mirror relative to the beam path. Additionally, it was not possible to pump the PPLN-based OPO with the spectrally-dispersed beam from the laser and so the extracavity prism sequence was necessary for this particular application.

To facilitate self-modelocking, an extracavity self-starting mechanism was included[9] in the form of an aluminium mirror, mounted on a small audio loudspeaker running at ~10 Hz. This provided sufficient amplitude modulation to initiate self-modelocked operation of the laser and also maximised the self-modelocked output power by allowing the light to travel in a single direction around the ring cavity. It was found that feedback from this moving mirror could disrupt the self-modelocking process of the laser. Once self-modelocking was achieved the moving mirror was blocked to prevent this from occurring.

With careful and accurate optimisation of the cavity alignment, the laser could be made to self-modelock, producing pulses with durations close to 13 fs, at average output powers of ~1.5 W and at a repetition rate of ~109 MHz. Under these conditions self-modelocked operation could be sustained for several hours in the

absence of any external vibrations perturbing the system. Temporal characterisation of the output from this laser was carried out using an ultra-bright AlGaAs LED (E_g=660 nm)[10,11] as the detector in the autocorrelator. Typical autocorrelation and spectral measurements from this laser system are presented in Figure 2. Assuming a $sech^2(t)$ intensity profile the time-bandwidth product of the generated pulses was 0.36 indicating that the pulses were transform-limited

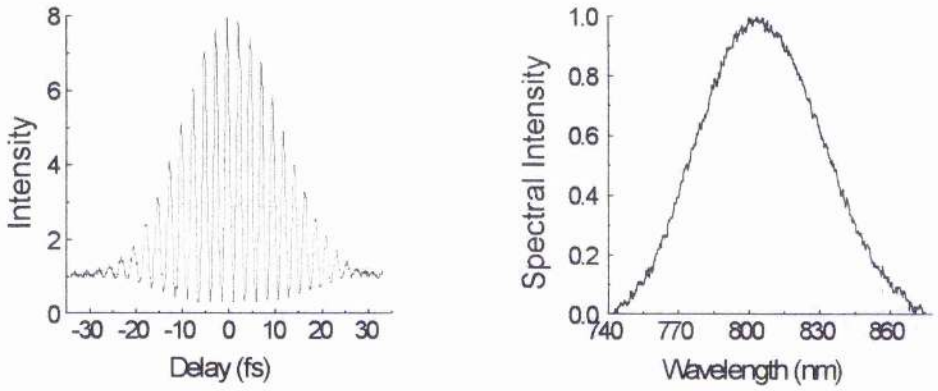

Figure 2: Typical autocorrelation and spectral measurements from the megawatt Ti:sapphire laser.

The average output power at the time this measurement was taken exceeded 1.4 W, which corresponds to a pulse peak power of ~1 MW and a pulse energy of 13 nJ.

The PPLN-based OPO

It was found that oscillation of the OPO could not be sustained when the pump pulse duration was as short as 13 fs. Hence, for the purposes of this experiment, a small amount of prism glass was inserted into the laser cavity to lengthen the pump pulse duration to ~17 fs. Under these conditions peak output powers close to 12 nJ were available from the laser. This proved to be the shortest duration of pump pulse that

could be used to operate the OPO and the reasons for this are discussed later in this chapter. Also, the wavelength was tuned to 840 nm, close to the long wavelength limit of the mirror coatings because this provided the most stable operation of the pump laser.

A schematic diagram of the experimental set-up for the PPLN-based OPO is shown in Figure 3. The OPO was configured, as previously, in a three-mirror V-cavity with a number of modifications to the cavity components to reduce the output pulse durations available from the system. A PPLN crystal identical to that which was used in the work described in Chapter 5, was used in this experiment, but only the 21.79 μm grating was used. This was the most appropriate choice of grating period for operation in the highest gain region of the phasematching curve shown in Figure 6. The crystal temperature was again maintained at 100 °C for the reasons described already. The pump beam was focused into the crystal using a 150 mm radius of curvature mirror to optimally match the radius of the intracavity signal beam. (Using a focusing mirror instead of a lens served to reduce the intracavity material dispersion experienced by the pump pulse on transit through M1.) This mirror was gold-coated to provide broadband high reflectivity at 800 nm. The radius of curvature of the concave focusing mirrors (M1 and M2) was 100 mm. The cavity mirrors comprised a high reflectivity mirror at 1.115 μm on a 0.5 mm thick CaF_2 substrate (M1), which was also highly transmitting at the pump wavelength. The second mirror, M2, was also coated for high reflectivity at 1.115 μm on a 0.5 mm thick CaF_2 substrate. M3 was either a 1 % output coupler at 1.115 μm on a 0.5 mm thick fused silica substrate or a plane highly reflecting mirror at 1.115 μm on a fused silica substrate. The

thinnest possible mirror substrates were chosen to reduce the pump pulse broadening experienced on transit through M1, the idler pulse broadening experienced on transit through M2 and the signal pulse broadening experienced on transit through M3. CaF_2 was chosen as the substrate for the mirror through which the idler was to be extracted as CaF_2 is highly transmitting at the idler wavelength. Fused silica was chosen as the substrate for M3 because fused silica introduced a minimum amount of third-order dispersion at the signal wavelength.

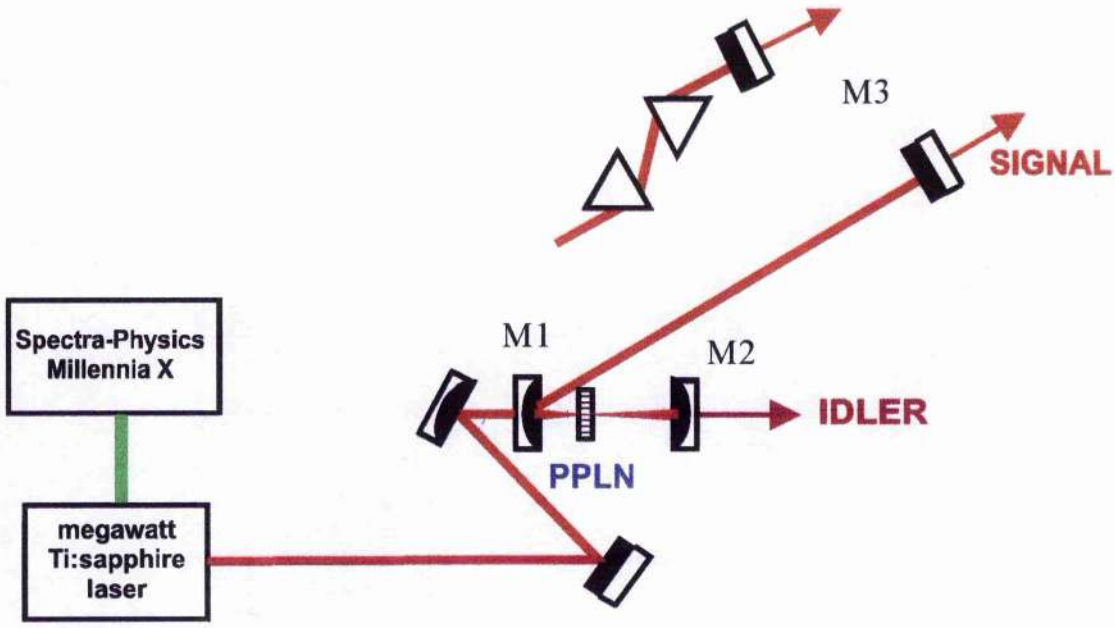

Figure 3: The PPLN-based OPO cavity configuration

For this particular choice of grating period and mirror set, varying the cavity length of the PPLN-OPO provided a tuning range that extended continuously from 1.045 μm to 1.190 μm for the signal and 2.57 μm to 3.67 μm for the idler. Typical spectra recorded over these tuning ranges for the signal and the idler are shown in Figure 4. The signal spectra were measured using a Rees Instruments Laser Spectrum

Analyser[12] and the idler spectra were measured using a Monolight Spectrum Analyser[13].

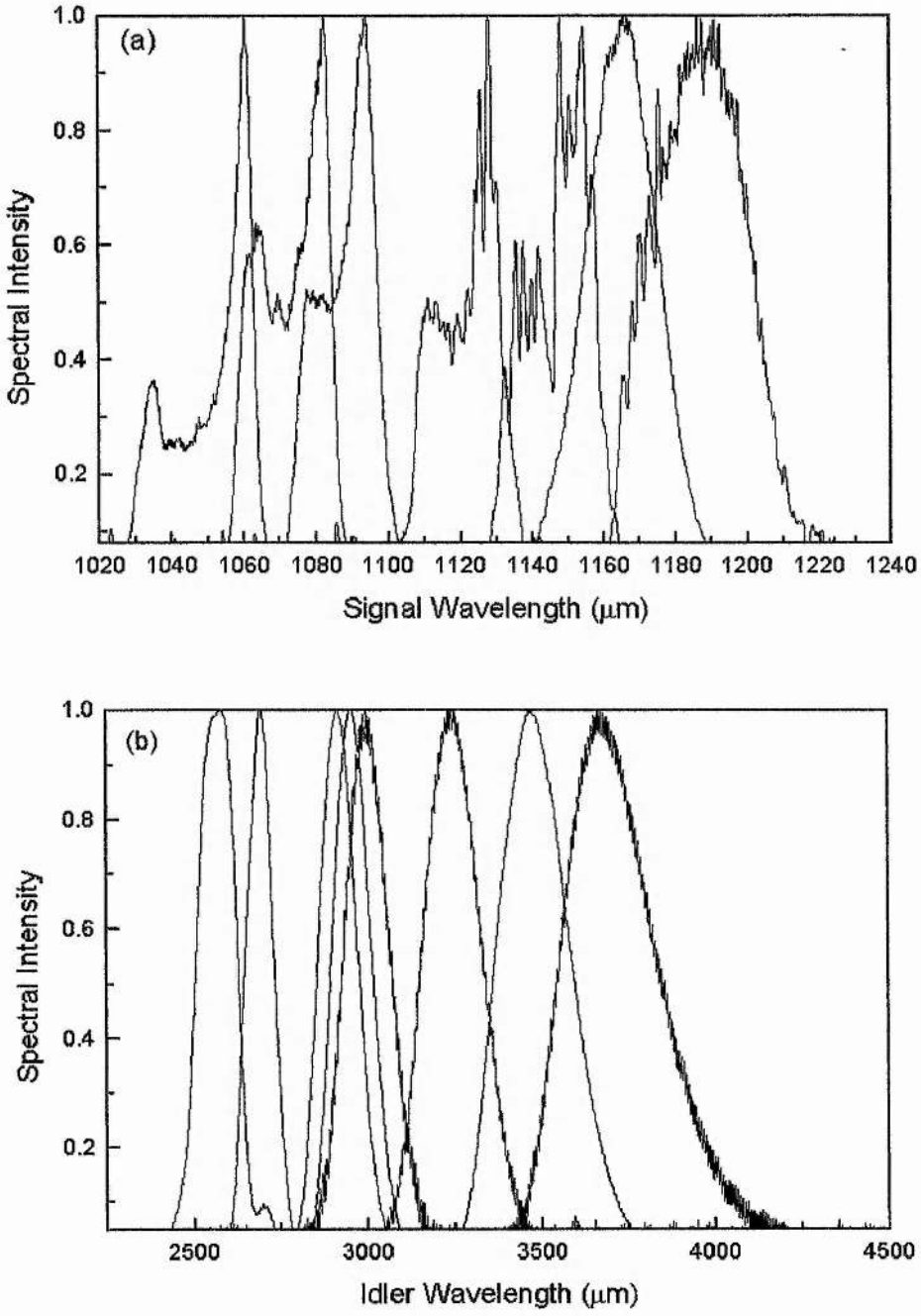

Figure 4: The tuning ranges of (a) the signal extending from 1.045 μm – 1.190 μm and (b) the idler extending from 2.57 μm – 3.67 μm.

A phasematching curve was generated for PPLN for a pump wavelength of 840 nm and a crystal temperature of 100 °C, and this is shown in Figure 5. The Sellmeier equation and coefficients given in Chapter 5 were used[14].

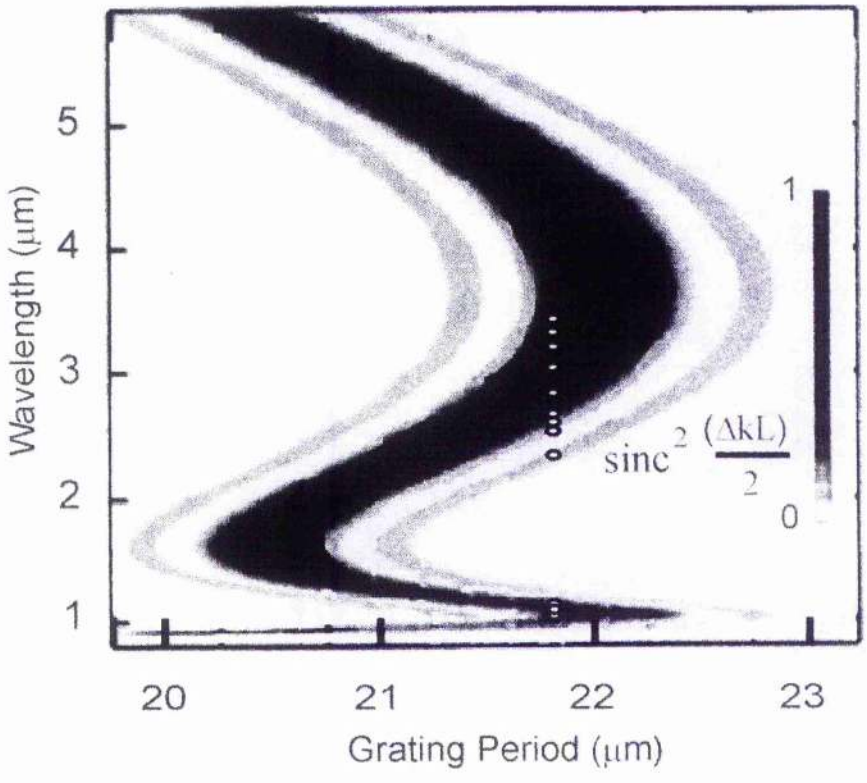

Figure 6: A phasematching curve generated for PPLN for a pump wavelength of 840 nm and a crystal temperature of 100 °C, including the $sinc^2$ variation of the gain bandwidth.

The experimental data points corresponding to the signal and idler wavelengths generated from the OPO are also shown on this graph. The phasematching curve includes the $sinc^2$ variation of the gain bandwidth, with the areas of highest gain shown in black ($\Delta k=0$) and the areas of lowest gain shown in white (Δk equals an

integral multiple of 2π). It can clearly be seen that, for a grating period of 21.79 μm, the OPO operated across the highest gain region of the phasematching curve.

Intracavity dispersion compensation was achieved by including a pair of F2 prisms in the OPO cavity, with an apex separation of 44.9 cm. The prism material F2 was chosen because it was suitable for second-order dispersion compensation, but more importantly also introduced minimal third-order dispersion at the operating wavelength of 1.115 μm[15].

The separation of the F2 prisms was chosen so that the amount of intracavity prism glass could be adjusted through the point of minimum intracavity dispersion, that is zero second-order and minimal third-order intracavity dispersion. The single-pass dispersion of the OPO cavity can be calculated using:

$$\frac{d^2\phi}{d\omega^2} = \frac{\lambda^2}{2\pi c^2}\left(\frac{d\lambda}{dL}\right)^{-1}.$$

The tuning rate, $\frac{d\lambda}{dL}$, for a standing wave cavity of length L, was derived experimentally and had a value of 0.0073 in this case. This implied a single-pass dispersion of +270 fs^2. The Sellmeier equation for PPLN, given in Equation (5.1), was used to calculate the material dispersion contributed by the PPLN crystal itself. It was found to be +250 fs^2, implying a residual dispersion associated with the cavity mirrors and the air, of +20 fs^2. In Chapter 4, the residual cavity dispersion associated with the cavity mirrors and the air in the PPRTA-based OPO was +80 fs. Thus, the modifications to the cavity components had successfully served to reduce the intracavity material dispersion. The intracavity dispersion contribution from the air

was also less in the case of the PPLN-based OPO, because the cavity length was shorter.

It was expected that the intracavity dispersion was minimal when the output from the OPO could be tuned across the bandwidth of the mirror set via a minimal adjustment of the cavity length. Moving mirror M3 by ~20 μm was sufficient to achieve this degree of tuning. This could be readily observed because the cavity length tuning of the signal wave generated a corresponding variation in visible light wavelengths produced by the sum-frequency mixing of the pump and signal waves. Whilst configured in this way, the OPO was particularly susceptible to cavity length variations resulting from changes in the air density. This was sufficient, at times, to cause the OPO to flicker on and off.

The maximum idler output power was measured to be 6.8 mW at 2.7 μm, measured after the second curved mirror, when all the cavity mirrors were highly reflecting. This values is not corrected for the loss incurred on transmission through the second curved mirror, M2. The maximum signal output power was measured after M3 to be 28 mW at 1.07 μm, when M3 was a 1 % output coupler. The amount of output power generated for both the signal and the idler waves was disappointing. It had been expected that the gain of the OPO would have been higher. The operation of the OPO was fundamentally limited by the extent of the temporal walk-away between the pump, signal and idler pulses[16]. Calculations revealed that the signal and idler pulses walked away from the pump pulse by as much as +160 fs/mm (for the signal)

and −140 fs/mm (for the idler), thereby explaining the low gain available from the PPLN-based OPO.

The variation of the temporal walk-away between the pump, signal and idler waves is shown in Figure 6.

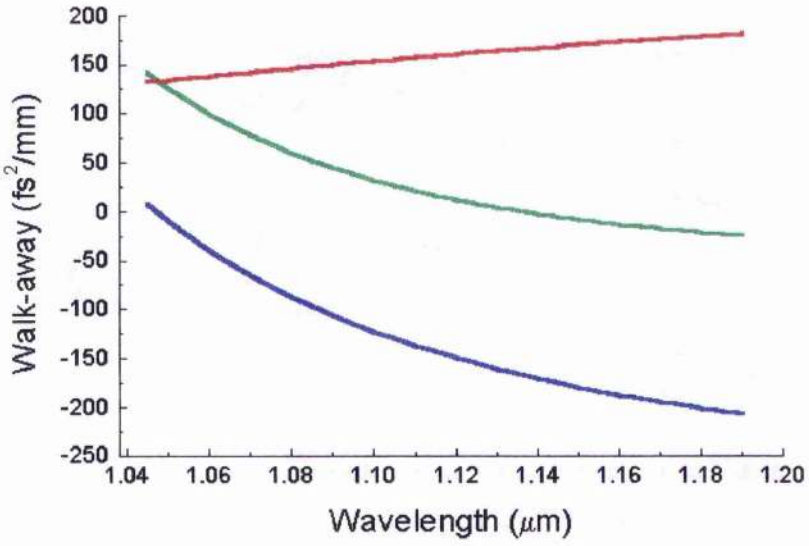

Figure 6: The variation of the temporal walk-away between the pump & signal (red), pump & idler (blue) and signal & idler (green) waves over the tuning range measured for the PPLN-based OPO.

The amount of temporal walk-away between the interacting pulses is considerable and is greater at the longer wavelength end of the tuning range. This explains why the highest output powers from the system were measured for shorter wavelengths, where the interaction between the pulses is stronger. Had a pump wavelength of 800 nm been used, the amount of temporal walk-away between the interacting pulses would have been higher. For a pump wavelength of 800 nm, the signal and idler pulses

would have walked away from the pump pulse at a rate of +200 fs/mm and –250 fs/mm respectively, at the operating wavelength of 1.115 μm.

It was also for this reason, that pump pulses of as short as 13 fs duration could not be used to pump the PPLN-based OPO. The extent of the temporal walk-away problem was such that a pump pulse duration of less than ~17 fs did not provide enough interaction for gain to be achieved in the OPO. Further more, the OPO operated well when pumped with a chirped laser pulse. On an occasion when the laser cavity had been slightly misaligned, resulting in the production of chirped pulses, the OPO produced a stable and broadly tunable output. It was thought that the large bandwidth associated with the frequency-chirped pulses was sufficient to enable the OPO to be widely tunable even though the pump pulse duration was not optimally short.

It was also found that, if the pump power fell below ~1 W, the OPO would no longer oscillate. The pump threshold was measured as 900 mW for this amount of output coupling. This was a further consequence of the amount of temporal walk-away between the interacting pulses in the OPO.

Pulse characterisation of the OPO was only possible with intracavity dispersion compensation as this offered more stable operation. The 1 % output coupler was used as M3 to maximise the output power. Temporal analysis of the signal pulses was carried out using an ultra-bright AlGaAs LED (E_g=660 nm)[17,18] as the detector in the autocorrelator. An intensity autocorrelation and spectrum of the signal pulses generated at 1.09 μm is shown in Figure 7.

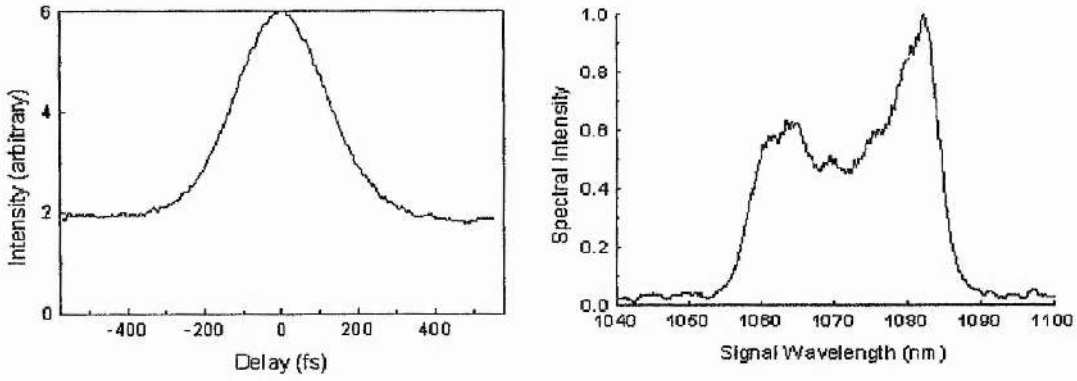

Figure 7: Typical autocorrelation and spectral measurements from the PPLN-based OPO, implying a pulse duration of 175 fs.

The pulse duration determined from the intensity autocorrelation profile is 175 fs which, when combined with the spectral data, implies a duration-bandwidth product of $\Delta\tau\Delta\nu=0.95$, assuming a $\text{sech}^2(t)$ pulse shape. Thus the pulses were not close to transform-limited as had been initially thought. The double-peaked nature of the spectrum recorded at 1.09 μm revealed that the dispersion compensation had not been sufficient to eliminate the effects of self-phase modulation on the output pulse. The SPM associated with the pulses would have been considerable because of the high peak powers introduced by the pump pulse. At the long wavelength limit of the tuning range, the spectrum recorded for the signal was a more characteristic "bell-shape" with a broader bandwidth, suggesting that shorter or less chirped pulses might have been available had there been sufficient output power to characterise the OPO at such long wavelengths. The OPO produced insufficient output power for it to be possible to carry out successful temporal characterisation of the idler pulses.

Conclusions

In Chapter 5 the operation and characterisation of an all-solid-state femtosecond OPO based on PPLN was described. The results presented and the results of previous work [19] show that a tuning range extending from 975 nm to 5.36 μm is available from such an OPO. It was also shown that pulse durations of the order of 200 fs are readily available from this OPO, across the tuning range described[20]. In this chapter a similar PPLN-based OPO has been described, with modifications made to the cavity elements, in an effort to reduce the output pulse duration of the OPO. This system was pumped by a sub- 20 fs Ti:sapphire laser. It was believed that if this extremely short pulse duration could be made maintained during frequency-conversion to wavelengths of the order of 5 μm (the idler in this case), then the number of optical cycles within the pulse envelope would be reduced. This meant that the PPLN-based OPO might prove to be an exceptionally broad-bandwidth, or "white-light" source in the mid-infrared. Although this was not achieved in this experiment, it was shown that a large number of improvements could be made to the cavity components to minimise the intracavity round-trip dispersion and that an appropriate choice of prism material can provide a means of compensating for this dispersion to some extent.

The high peak powers associated with the pump pulse increased the effects of self-phase modulation on the output pulses from the OPO and the extent of the temporal walk-away severely limited the gain of the OPO. All the same, a pulse duration of 175 fs was recorded for the signal at a wavelength of 1.07 μm. Output powers of 28 mW for the signal at 1.07 μm and 6.8 mW for the idler at 2.7 μm were also

measured. The tuning range for the signal extended from 1.045 μm to 1.190 μm, and for the idler, extended from 2.57 μm to 3.67 μm.

The results of this work have shown that, provided a sub- 20 fs Ti:sapphire laser produces sufficient output power, then it can be successfully used to pump a PPLN-based OPO. Improvements to the cavity design, in terms of dispersion compensation, caused the OPO to generate shorter pulses than had been previously measured from a similar system. The tuning range of a PPLN-based OPO can be readily extended to ~5.36 μm by an appropriate choice of pump wavelength, grating period and mirror-set. Thus the available pump pulse durations and wavelength coverage of OPOs based on periodically-poled materials are sufficient to pose the question of the generation of single-cycle optical pulses in the mid-infrared, provided that the intracavity dispersion can be precisely controlled. The potential undoubtedly exists for exciting new developments in the area and the results presented here are encouraging in a preliminary context.

Chapter 6

References

1. C McGowan, D.T Reid, Z.E Penman, M Ebrahimzadeh, W. Sibbett and D.H Jundt, *J. Opt. Soc. Am. B* **15** 694 (1998)
2. Z Penman, P Loza-Alvarez, D.T Reid, M Ebrahimzadeh, W. Sibbett D.H Jundt, *Opt. Commun.* **146** 147 (1998)
3. C.L Spielmann, R Szipocs, A Stingl and F Krausz, *Phys. Rev. Lett.* **73** 2308 (1994)
4. M Asaki, C Huang, D Garvey, J Zhon, H.C Kapteyn and M.M Murnane, *Opt. Lett.* **18** 977 (1993)
5. L Xu, G Tempea, Ch Spielmann, F Krausz, A Stingl, K Ferencz and S Takano, *Opt. Lett.* **23** 789 (1998)
6. T Beddard, W Sibbett and D.T Reid, *Opt. Lett.* (accepted)
7. K Tamura, J Jacobson, E.P Ippen, H.A Haus and J.G Fujimoto, *Opt. Lett.* **18** 220 (1993)
8. C McGowan, D.T Reid, Z.E Penman, M Ebrahimzadeh, W. Sibbett and D.H Jundt, *J. Opt. Soc. Am. B* **15** 694 (1998)
9. D.T Reid, M Padgett, C McGowan, W.E Sleat, and W Sibbett, *Opt. Lett.* **22** 233 (1997)
10. Photodiodes data sheet, Hamamatsu Photonics K.K., Solid State Division
11. Rees Instruments Ltd, Thornbrook, Weyside Park, Cattleshall Lane, Godalming, Surrey, GU7 1XE
12. Monolight mid-infrared optical spectrum analyser, Macam Photometrics Ltd, 10 Kelvin Square, Livingston, EH54 5PF
13. D.H Jundt, *Opt. Lett.* **20** 1553 (1997)

14. B.E Lemoff and C.P.J Barty, *Opt. Lett.* **18** 57 (1993)

15. V.G Dmitriev, G.G Gurzadyan and D.N Nikogosyan, Handbook of Nonlinear Optical Crystals (second ed., Springer-Verlag, Belrin, 1997)

16. D. T. Reid, C. McGowan, M. Ebrahimzadeh and W. Sibbett, *IEEE J. Quantum. Electron.* **33**, 1, (1997)

17. Photodiodes data sheet, Hamamatsu Photonics K.K., Solid State Division

CHAPTER 7

General Conclusions

The research which has been presented in this thesis is concerned with the recent development of self-modelocked Ti:sapphire lasers and femtosecond optical parametric oscillators based on periodically-poled rubidium titanyl arsenate and lithium niobate and operating in the near and mid-infrared.

The purpose of Chapter 1 was to explain the theory of ultrashort pulse generation with regard to the Ti:sapphire laser. The optical properties of Ti:sapphire were discussed along with the principles of laser oscillation and pulse generation. The techniques used to modelock the lasers used in the experimental work, which followed, were also considered. The second part of the chapter dealt with typical measurement techniques for characterising femtosecond optical pulses from a laser or an OPO, including a detailed explanation of second harmonic generation autocorrelation. Chapter 1 concluded with a thorough description of frequency-resolved optical gating, the newest of these pulse characterisation techniques.

In Chapter 2 the subject of nonlinear optics and the properties of nonlinear optical materials were discussed. Phasematching in nonlinear optical materials was explained along with the principle techniques for achieving this, including birefringent phasematching and quasi-phasematching. A review of techniques for periodically-poling nonlinear optical crystals was also given. The chapter concluded with a section on the optical effects of group velocity dispersion and self-phase modulation, that

influence the output from an ultrashort pulse laser or OPO and described methods for second and third-order dispersion compensation. Chapter 2 concluded the theory required to understand the experiments described in Chapters 3, 4, 5 and 6.

Chapter 3 described the operation and characterisation of two different Ti:sapphire laser systems involving different methods of dispersion compensation. The first laser produced 100 fs duration self-modelocked laser pulses and dispersion compensation was achieved by including a pair of prisms in the cavity. Output powers of the order of ~900 mW were available from this system. This laser system was discussed further in Chapter 5, where it was operated in conjunction with a Spectra Physics Millennia, as the pump source for an all-solid-state femtosecond OPO based on periodically-poled lithium niobate (PPLN). The output powers available from this system were sufficient to pump the OPO, and pulse durations of the order of 200 fs were obtained by including a pair of prisms in the OPO cavity to compensate for the intracavity dispersion.

The second laser system described in Chapter 3 produced self-modelocked pulses of ~15 fs duration and dispersion compensation was achieved by including chirped multilayer dielectric mirrors in the cavity. Output powers of around 480 mW were available from this system and it was originally intended that this laser would also be used as the pump source for a PPLN-based OPO. Shorter pump pulses, as were available from this laser, opened up the possibility of producing shorted pulses from the OPO. The OPO described in Chapter 5 was modified in a number of ways to reduce the intracavity dispersion introduced by the cavity optics, and a shorter pulse version of this system was described in Chapter 6. The Ti:sapphire laser which was

actually used to pump this PPLN-based OPO was a unidirectional ring laser cavity, which included four prisms to provide dispersion compensation, and was capable of generating sub– 15 fs duration pulses at higher output powers than were available from the mirror-dispersion-compensated Ti:sapphire laser system. This Ti:sapphire laser was described in more detail at the beginning of Chapter 6.

The subject matter that Chapter 4 was concerned with included the operation and characterisation of a femtosecond OPO based on PPRTA. Ti:sapphire pump wavelength tuning and cavity-length tuning of the OPO were shown to produce wavelengths throughout the range 1.060 μm to 1.225 μm in the signal and 2.67 μm to 4.5 μm in the idler, with average output powers as high as 120 mW in the signal and 105 mW in the idler output. The effects of photorefractive damage were minimal and consequently this offered the possibility of room-temperature operation of the PPRTA-based OPO.

Until recently, telecommunication systems had predominantly relied upon colour-centre lasers, self-modelocked Cr^{4+}:YAG lasers and optical parametric oscillators to generate wavelengths close to 1.5 μm. Colour-centre lasers were limited by their use of cryogenic-cooling methods and self-modelocking of Cr^{4+}:YAG lasers met with practical difficulties in sustaining oscillation close to the water absorption at 1.4 μm. Since then it has been shown that it is also possible to construct a femtosecond OPO based on PPRTA that is continuously tunable from 1.375 μm to 1.575 μm for the signal thus overcoming the limits of some other systems. Output powers as high as 110 mW were obtained from this system at a wavelength of 1.46 μm.

Chapter 5 was concerned with the generation of longer idler wavelengths, in the region of 5 μm, from an all-solid-state OPO based on periodically-poled lithium niobate. Having already generated 4.55 μm from a PPLN-based OPO, the choice of grating period and mirror sets combined with the longest available pump wavelength of 840 nm, we believed that PPLN was a more suitable choice of crystal for the OPO than PPRTA, in this case.

The approach used with the PPRTA-based OPO was extended to PPLN and in Chapter 5, results were presented which showed that the use of an all-solid-state Ti:sapphire pump source in combination with a PPLN-based OPO represented a robust source of high-repetition-rate femtosecond pulses in the mid-infrared at wavelengths out to ~5 μm. Significantly higher output powers in the signal and idler than previously reported were also measured.

It was shown that the tuning range of the PPLN-based OPO could be readily extended to longer idler wavelengths, of ~5 μm and, in fact, idler wavelengths as long as 5.36 μm were reached with this system. The use of a crystal which was AR-coated for shorter signal wavelengths combined with a shorter grating period and a longer pump wavelength could undoubtedly see this range extended yet further in accordance with the phasematching condition. It was shown that using a collinear geometry pulses of ~200 fs duration at powers of 240 mW for the signal, and 106 mW for the idler can be produced by an OPO based on PPLN. Powers of 25mW at wavelengths as long as 4.88 μm were also readily available.

More recent work has shown that wavelengths close to 6.3 μm can be generated using a PPLN-based OPO. Hanna et al. attained this wavelength using a picosecond PPLN-based OPO, which was synchronously-pumped by a Nd:YLF laser operating at 1.047 μm.

In Chapter 6 a similar PPLN-based OPO was described, with modifications made to the cavity elements, in an effort to reduce the output pulse duration of the OPO. This system was pumped by a sub- 20 fs Ti:sapphire laser. It was believed that if this extremely short pulse duration could be made maintained during frequency-conversion to wavelengths of the order of 5 μm, then the number of optical cycles within the pulse envelope would be reduced. This meant that the PPLN-based OPO might prove to be an exceptionally broad-bandwidth, or "white-light" source in the mid-infrared. Although this was not achieved in this experiment, it was shown that a large number of improvements could be made to the cavity components to minimise the intracavity round-trip dispersion and that an appropriate choice of prism material could provide a means of compensating for this dispersion to some extent.

The high peak powers associated with the pump pulse increased the effects of self-phase modulation on the output pulses from this OPO and the extent of the temporal walk-away severely limited the gain of the OPO. All the same, a pulse duration of 175 fs was recorded for the signal at a wavelength of 1.07 μm. Output powers of 28 mW for the signal at 1.07 μm and 6.8 mW for the idler at 2.7 μm were also measured. The tuning range for the signal extended from 1.045 μm to 1.190 μm, and for the idler, extended from 2.57 μm to 3.67 μm.

Work is ongoing in this area of research, to extend the wavelength coverage of the OPOs yet further into the mid-infrared. Also the quest for single-cycle optical pulses and an ultimate "white-light" source in the mid-infrared continues. The development of improved methods for dispersion compensation and novel new sources based on periodically-poled materials, which have proved to be extensively tunable, means that the chances of reaching this goal are ever increasing.

Publications

C McGowan, D.T Reid, Z.E Penman, M Ebrahimzadeh, W. Sibbett and D.H Jundt "Femtosecond optical parametric oscillator based on periodically poled lithium niobate" *J. Opt. Soc. Am. B* **15** 694 (1998)

D.T Reid, Z.E Penman, M Ebrahimzadeh, W Sibbett, H Karlsson and F Laurell "Broadly tunable femtosecond optical parametric oscillator based on periodically poled RbTiOAsO4" *Opt. Lett.* **22** 1397 (1997)

Z.E Penman, T Schittkowski, W Sleat, D.T Reid and W Sibbett "Experimental analysis of a self-modelocked Ti:Sapphire laser using second harmonic generation autocorrelation frequency-resolved optical gating" *Opt. Commun.* (accepted)

Z.E Penman, P Loza-Alvarez, D.T Reid, M Ebrahimzadeh, W. Sibbett D.H Jundt "All-solid-state mid-infrared optical parametric oscillator based on periodically-poled lithium niobate" *Opt. Commun.* **146** 147 (1998)

Z.E Penman, C McGowan, P Loza-Alvarez, D.T Reid, M Ebrahimzadeh, W. Sibbett and D.H Jundt "Femtosecond optical parametric oscillators based on periodically poled lithium niobate" *J. of Modern Optics* **45** 1285 (1998)

Acknowledgements

I am indebted to my supervisor, Professor Wilson Sibbett, for his support and guidance throughout my time in research. I would like to thank Karen Oppo for her help with the Ti:sapphire laser and for being a good friend in the early days and Bill Sleat for his help with everything electronic. I am grateful to Cate for her help with the first PPLN OPO, Derryck for his help with the PPRTA OPO, Pablo for his help with the all-solid-state PPLN OPO and Tom for his help with the unidirectional ring Ti:sapphire laser. I would also like to thank John-Mark, David and Gareth for their friendship and understanding and the rest of the W-squad for their generous use of the computers.

I would like to thank my family for all their help and support throughout my time at St. Andrews.

This work was funded by the Engineering and Physical Sciences Research Council to whom I am very grateful.